Spring 2009

Investigation of the interactions between selected nanoparticles and human lung carcinoma cells at the single cell and single particle level

Isaac Stayton

Department: Chemistry

INVESTIGATION OF THE INTERACTIONS BETWEEN SELECTED NANOPARTICLES AND HUMAN LUNG CARCINOMA CELLS AT THE SINGLE CELL AND SINGLE PARTICLE LEVEL

by

ISAAC ALEXANDER STAYTON

A DISSERTATION

Presented to the Faculty of the Graduate School of

MISSOURI UNIVERSITY OF SCIENCE AND TECHNOLOGY

In Partial Fulfillment of the Requirements for the Degree

DOCTOR OF PHILOSOPHY

in

CHEMISTRY

2009

Approved by:

Dr. Yinfa Ma, Advisor

Dr. Nuran Ercal

Dr. Shubhender Kapila

Dr. Jeffrey Winiarz

Dr. Yue-wern Huang

PUBLICATION DISSERTATION OPTION

This dissertation consists of the following three articles that have been published, submitted for publication, or will be submitted for publication as follows:

Pages 12 – 48 are intended for submission to ANALYTICAL AND BIOANALYTICAL CHEMISTRY.

Pages 49 – 67 were published in TOXICOLOGICAL AND ENVIRONMENTAL CHEMISTRY.

Pages 68 – 108 were submitted for publication in ANALYTICAL AND BIOANALYTICAL CHEMISTRY.

ABSTRACT

The recent advances in nanomaterials development and applications have sparked concerns regarding the safety of these materials in living organisms. This body of work investigates specific interactions between chosen nanoparticles and living human lung carcinoma (A549) cells. First presented is imaging platform development with applications in single molecule detection and live cell fluorescence imaging. Microcapillary, right angle prism, flat prism and modified microscope slide geometries are shown. Real-time disruption in cell membrane potential was investigated following exposure of A549 cells to Al_2O_3 and CeO_2 nanoparticles. It was found that, while all nanoparticles caused membrane depolarization relative to the control, Al_2O_3 particles exhibited the greater effect within the timeframe of our experiment. This effect was particle size-dependent, where the smaller particles caused the greater disruption. Fluorescence microscopy was used to investigate parameters influencing the internalization of amorphous SiO_2 nanoparticles in A549 cells. Nanoparticle-protein interactions were characterized as a function of time, as proteins are abundant in *in vitro* and biological environments. The effect of a particle's adsorbed protein charge on the rate of cell uptake showed that a greater negative charge slightly slowed particle uptake. However, in the absence of any adsorbed proteins on the nanoparticle surface, uptake nearly tripled, indicating alternative mechanisms governing the internalization process. We present evidence which suggests there is indiscriminate adsorption of bare SiO_2 nanoparticles on membrane surface proteins and subsequent internalization via endocytosis. In addition, we have shown that the agglomeration of silica nanoparticles in suspension has limited effect upon cell uptake. The nanoparticle loss from living A549 cells was characterized over time, which showed that although particle loss is rapid during the first eight hours after the removal of environmental nanoparticles, there remained particles inside the cells and it did not appear they would lose all internalized nanoparticles. In conclusion, these studies shed light upon some of the mechanisms which govern nanoparticle interactions with living A549 cells, and show the need for continued research in the areas of nanoparticle toxicology and environmental persistence.

ACKNOWLEDGEMENTS

The work presented in this doctoral dissertation would never have been possible without the continual support and guidance of my advisor, mentor and friend, Dr. Yinfa Ma. His direction in all aspects of my graduate work was invaluable and will be forever appreciated.

I would also like to thank my doctoral committee members, for the various ways in which they assisted me in my work. I would like to thank Dr. Jeffrey Winiarz for his enthusiastic patience in synthesizing nanoparticles, without which I could not have performed the experiments. I would like to thank Drs. Nuran Ercal and Yue-wern Huang for the use of their cell culture facilities and for advice in their respective fields of expertise in biochemistry and toxicology. I would like to thank Dr. Shubhender Kapila for his continual support.

This work was supported by Yinfa Ma's startup fund from Missouri S&T, the Missouri research Board, Frontage Laboratory, Inc., the Missouri S&T Department of Chemistry, the Environmental Research Center and the Center for Environmental Science and Technology. I am thankful for their financial support.

A great debt of thanks is owed to Dr. Katie Shannon, for the use of the fluorescent microscope in her lab and for discussing my questions with me. I would like to thank Honglan Shi and Dr. Demin Wang for their time and assistance in operating instrumentation untried by me. I would like to thank Dr. David Hoiness for his continual help and interest. I would also like to thank Joseph Council, David Satterfield, Mike Myers and Dean Lenz for their help in instrument care and design, and in the manufacturing of the numerous bizarre things I wanted to try. I would like to thank the Department secretaries, Carol Rodman, Donna Riggs and Kathy Eudaly, who were constantly eager to help, and provided a wealth of timely information.

I would like to thank my family and especially my parents for their untiring support and encouragement, which took shape in so many ways. Their confidence and exhortation in all areas of life were always a strength to me. Finally, I would like to thank my Lord, for giving me strength and for ever holding up the highest standard, without which success would have been impossible.

TABLE OF CONTENTS

Page

PUBLICATION DISSERTATION OPTION.....iii

ABSTRACT.....iv

ACKNOWLEDGMENTS.....v

LIST OF ILLUSTRATIONS.....x

LIST OF TABLES.....xiii

INTRODUCTION.....1

Nanomaterials.....1

Cell Imaging.....4

Optics.....6

References.....8

PAPER

1. Single Molecule Spectroscopy and Single Cell Analysis: Applications in Nanoparticle Bioanalysis.....12

Abstract.....12

Keywords.....13

Introduction.....13

Experimental.....15

Chemicals.....15

Optics.....15

Cell Culture.....16

Labeling of DNA.....17

Labeling of Antibodies.....18

Purification of Labeled Antibodies.....18

Optical Measurements in a Square Capillary.....19

Optical Measurements on a Flat Surface.....22

Results and Discussion.....28

Interpretation of Data.....39

Conclusions.....45

Acknowledgements.....46

References.....46

2. Effect of nanoparticles on membrane potential of living A549 cells.....49

Abstract.....49

Keywords.....50

Introduction.....50

Experimental.....52

Nanoparticles.....52

Chemicals.....52

Cell Culture.....53

Single Cell Imaging Assembly.....53

Cell Labeling for Single Cell Imaging.....54

Equipment Setup.....55

Statistical Analysis.....57

Results.....58

Single Cell Imaging to Study the Interaction of Nanoparticles with Cells.....58

Discussion.....61

Conclusion.....64

Acknowledgements.....65

References.....65

3. Study of Uptake and Loss of Silica Nanoparticles in Living Human Lung Epithelial Cells at the Single Cell Level.....68

Abstract.....68

Keywords.....69

Introduction.....69

Experimental.....72

Chemicals.....72

Nanoparticle Synthesis and Characterization.....72

Spectral Analysis of Fluorescent Nanoparticles.....74

Cell Culture and Treatment with NPs.....74

Cell Imaging.....76

Cadmium Determination by ICP-MS.....77

Protein Content Assays.....78

Determination of Protein Adsorption onto SiO_2 NPs over Time.....78

Determination of Zeta Potential.....79

Results and Discussion.....80

Surface Characteristics of Fluorescent Nanoparticles.....80

Spectral Analysis of Fluorescent Nanoparticles.....81

Protein Adsorption onto SiO_2 NPs over Time.....81

Dose-dependent Uptake of NPs in Cells.....84

Time-dependent Uptake of NPs in Cells.....85

Internalization of NPs under Different Protein-coating Environments.....87

Loss of Internalized NPs over Time.....92

Cadmium Determination by Mass Spectrometry.....93

Interpretation of Data.....94

Conclusions.....103

Acknowledgements.....104

References.....105

CONCLUSIONS.....109

VITA.....111

LIST OF ILLUSTRATIONS

Figure Page

PAPER 1

1. Components of the single molecule imaging capillary mount.....20

2. Right angle prism mount in use for cell imaging.....24

3. Dimensions of quartz ATR plate.....25

4. Cell imaging using an ATR plate geometry.....26

5. Modified microscope slide with small right angle prism used for cell imaging.....27

6. Yoyo-I labeled lambda-DNA molecules imaged one by one by fluorescence microscopy using a square capillary.....28

7. Single molecule spectroscopy of dye-labeled immunoglobulins.....29

8. Difference in mobilities of dye-labeled antibodies versus their immunocomplexes.....30

9. Mobility of unbound human IgG molecules compared to the mobility of those bound by a complementary anti-human IgG antibody.....31

10. Importance of solvent photobleaching in single fluorescent nanoparticle imaging in a square capillary.....32

11. Labeled lambda-DNA imaged using a large right angle prism.....33

12. Cell fluorescence from living cells placed on a large right angle prism.....34

13. Labeled lambda-DNA imaged on the flat prism.....35

14. Cells labeled with membrane dye, imaged using the flat prism.....36

15. Fluorescent images of cells labeled with membrane dye, imaged using the modified prism-microscope slide.....36

16. Phase contrast images collected using the prism-slide sample mount.....37

17. Fluorescent nanoparticles imaged on the combination prism-slide.....37

18. Images of materials imperfections observed in different types of cover glasses.....39

19. Micro-scratches on the surface of a right angle prism.....42

PAPER 2

1. Sample introduction system for single cell imaging.....55

2. Optical setup for single cell imaging.....58

3. Averaged percent change in cellular fluorescence intensity for control, and after treatment with Al_2O_3 and CeO_2 nanoparticles.....60

4. Examples of fluorescence intensity changes after cells were exposed to 13 nm and 22 nm Al_2O_3 nanoparticles.....61

PAPER 3

1. Absorbance curve and fluorescence emission peaks following excitation at noted wavelengths for fluorescent nanoparticles.....82

2. Protein adsorption onto silica nanoparticles over time in complete cell growth medium.....83

3. Uptake of fluorescent silica-coated nanoparticles following different doses.....85

4. Uptake of fluorescent NPs under different protein environments.....86

5. A549 cells in complete medium with internalized fluorescent nanoparticles after specified durations of exposure.....88

6. Nanoparticle uptake of pre-agglomerated particles compared to regularly-dispersed particles.....91

7. Uptake of nanoparticles in medium lacking serum (protein-free), and in complete medium.....92

8. Loss of nanoparticles from cells over time, following the removal of the environmental presence of particles.....93

9. Cell uptake of NPs in complete medium, showing NP agglomerates loosely associated with cell membrane surfaces prior to rinsing, and the disappearance of NPs after rinsing.....101

10. Serum-free uptake showing nanoparticle aggregates adsorbed onto glass plate surface.....103

LIST OF TABLES

Table Page

PAPER 1

1. Background noise associated with different sample optic materials.....38

PAPER 3

1. Zeta potentials of bare and specific protein-coated silica NPs suspended in purified water.....90

2. Analysis of Cd in cells and growth medium using ICP-MS.....95

INTRODUCTION

Nanomaterials

The scientific community has begun in recent years to evaluate nanomaterials with respect to their toxicity. Attention has been given in areas as widespread as drug delivery development, consumer products and the environment (Nohynek et al., 2007; De Jong and Borm, 2008; Handy et al., 2008; Krug and Klug, 2008; Nohynek et al., 2008).

Though relatively new in their current wide-spread popularity in scientific research, nanomaterials have existed in the environment naturally. From fullerene occurrences reported in outer space (Radicati di Brozolo et al., 1994) to possible fullerene occurrences in mineral deposits (Gu et al., 1995; Parthasarathy et al., 1998), natural sources of materials in the nanometer size range will likely continue to be discovered as time progresses. Already “natural product” nanoparticles (NPs) have been produced as catalysts in cleaning products (Nero and Tran, 2007). Before the recent popularity of nano-based science, there existed at least some nanomaterials in scientific use. A prime example is Percoll, a polyvinylpyrrolidone-coated silica particle medium used in separating centrifuged lab samples by their density gradient (Kurnick et al., 1979).

Percoll was originally thought to be nontoxic (Brysk et al., 1981; Tengvar et al., 1983). However, there soon arose studies challenging its nontoxic status (Viscardi et al., 1992). Less than five years later, the product Percoll was removed from the market over toxicity and contamination concerns (Ren et al., 2004).

It must be noted that Percoll was accepted in numerous laboratory methods, and enjoyed reasonably wide use. If this product – once thought to be safe – was discovered to be hazardous after years of routine use, what other products or substances should also be evaluated for their potential to cause harm in living organisms? While some nanoparticles, such as those synthesized from CdTe, would obviously seem toxic (Lovric et al., 2005), what becomes their toxicity status after they have been coated with a polymer designed for biological use (Wang et al., 2007)? Which nanomaterials that appear to be harmless in the micron size range may induce toxicity in the nano size range (Lin et al., 2006)?

Nanomaterials present numerous unknowns to researchers. This is the very reason they have become ubiquitous in research labs around the world today, where scientists hope to learn and develop uses for their unique properties. While a given material's bulk properties may be well described, and that same material's molecular properties soundly understood, its behavior while comprising shapes within the 1 – 100 nm size range may be radically different. A perfect example of this phenomenon is CdSe. In its bulk substrate form, CdSe is a semiconductor that exhibits properties expected from that class of materials (Bertolotti et al., 1967; Tyagai and Kolbasov, 1971; Kulshrestha et al., 1986). In its molecular form, it is also well understood as a toxic heavy metal substance (Shabalina, 1966; Mount and Stephan, 1967; Abraham and McEuen, 1986). But when CdSe crystals were synthesized with diameters in the 5 nm range, they showed characteristics unlike either their bulk or molecular counterparts (Schlegel et al., 2002; Shimizu et al., 2002; Brokmann et al., 2004). A "new-to-science" observation was made of these and similar types of semiconductor nanocrystals: broad absorbtion bands

extending down into the ultraviolet, and strong, blinking fluorescence observed in the visible light range. It was discovered that as the semiconductor material's size changed from the micro- to the nano-range, the behavior of an excited electron changed. Confined by the size of the nanocrystal, the electron produced a fluorescence effect. Furthermore, the size of the nanocrystal dictated the wavelength at which fluorescence emission was observed (Nirmal et al., 1993; Norris et al., 1993). Today, these, and other similar fluorescing nanocrystals have revolutionized the way in which fluorescence microscopy is performed. They provide a fluorescent marker which is significantly more resistant to photobleaching than most traditional organic dyes, and one that can have its absorbance and emission spectra changed simply by altering particle size.

Some general nanoparticle properties have already been alluded to, and others merit further explicit description. By nature of their size, NPs have a very large surface area relative to their mass. This property translates directly into there being a high surface energy for NPs. Resulting from their high surface energy was the tendency of NPs to form aggregates when in suspension (Foucaud et al., 2007; Schulz et al., 2008; Jiang et al., 2009). Such agglomerates were observed during this work, and became especially important for the experiments presented in Paper 3. A characteristic common to numerous NP types is that of surface charge. Once again, because of their high surface area, charged surface moieties may effectively direct NP behavior. In Paper 3, experimental particle surface charge was explored relative to its effects upon nanoparticle-cell interactions.

The goal of this work was not to declare all nanomaterials imminent health threats, but was instead to increase knowledge of the mechanisms through which some

commonly-produced NPs interact with living human lung carcinoma-derived cells. It is hoped that a better understanding of these interactions will lead to a halt of harmful applications of nanomaterials in the present, and help prevent them from existing in the future.

Cell Imaging

In vitro studies often take one of two approaches to solve a given problem. Commonly used are “bulk cell” methods, which measure the averaged response of many cells simultaneously. The number of cells analyzed for a single measurement may vary from hundreds to even millions. The obvious benefit from such an approach arises from the fact that biological systems – even at the single cell level – do not respond to an environmental stimulus with a stoichiometric response. When a large number of cells are measured together, the response may be understood as representative for the given stimulus. However, therein lies the weakness of a bulk cell approach: the response is an average, and mechanistic data can be lost since thousands of cells at different stages of growth, etc. respond simultaneously.

To overcome this poor experimental resolution, microscopy is used to bring the analysis down to the single cell level. The first advantage is evident in the ability to observe one cell next to another and distinguish their individual responses. While not necessarily advantageous to claiming a representative response, a study at this level has the ability to observe *when* and *how* a given response is exhibited relative to the stimulus. Details of cell morphology become suddenly evident. Conditions such as “blebbing” in

apoptotic cells are visible. In experiments such as were performed in this study, sub-cellular and extracellular locations of nanoparticles were able to be observed.

As this study was designed to model circumstances that occur in the "real world," it may at first appear less than ideal that the authors chose to use the A549 (derived from human lung carcinoma cells) cell line. Human cells were chosen to make the information learned most directly applicable to human safety measures. Lung cells were chosen since, in the human body, a cell might be exposed to nanoparticles through inhalation, digestion or absorption through the skin. In the human body, should NPs be absorbed through the gastrointestinal tract, they would be spread through the body via the circulatory system and thereby to the lungs. Inhalation would lead to direct exposure to lung cells. A carcinoma-derived cell line was chosen because, at the time the study was begun, no normal human lung cell line was available which was capable of enough passages to be used in our study.

Adherent mammalian cells are nearly transparent using standard brightfield microscopy. The lack of most color in cellular components coupled with the finite thickness of the cell itself require phase contrast microscopy to be used if fluorescent emission signals are to be accurately compared to individual cell membrane boundaries. The primary disadvantage with phase contrast microscopy that will be noted when performing simultaneous fluorescence microscopy is the slight loss in a microscope objective's necessary decrease in numerical aperture. Fortunately, though the phase ring engineered within a phase contrast microscope objective partially blocks the fluorescent signal, it will not prevent a successful experiment if the objective is of high quality and other measures were taken to ensure an optimum signal to noise ratio.

One advantage to performing single cell fluorescence microscopy is the vast numbers of fluorescent markers available. Typically organic dyes, they are available to mark organelles, cell structures such as actin, and may reveal cellular conditions such as membrane potential. When chosen carefully, multiple cell marker dyes may be used at once, and multiple cell analysis parameters may be monitored at once. However, besides interference from other dyes (or fluorescent NPs), cell autofluorescence must not be allowed to give false positive signals. In analysis at the single cell level, autofluorescence may be identified using both wavelength and sub-cellular shape and location.

Optics

The importance of maximizing the signal to noise ratio in fluorescence microscopy cannot be overstated. An analyte's fluorescence signal is often characteristically weak as a result of poor quantum efficiency, low abundance or photobleaching. Only a percentage of it can be collected by the optics leading to the detector, since fluorescence is emitted radially – in every direction. Every optic involved in that light path reduces the fluorescent signal further through reflection, scatter and possibly absorption. Noise contributions are numerous and may originate in the excitation light source, undesired fluorophores in the sample or outside light sources.

Beyond the elimination of outside light sources, the careful choice of the excitation source and of system optics may make significant improvements upon the signal to noise ratio. Lasers typically provide the most monochromatic light used in fluorescence microscopy, and therefore yield lower noise levels since non-targeted

fluorophore excitation is minimized. They are also typically capable of higher excitation power, which can be used to achieve stronger analyte signal unless photobleaching prevents it. Ultraviolet lamps are popular because their cost is much lower than laser systems, and they are capable of exciting a much more broad range of fluorophores. To use a UV lamp for fluorophore excitation, a bandpass filter must be carefully chosen to select the desired wavelength range.

Regardless of the excitation source employed, in all but a very few cases a properly chosen bandpass filter must be used to block undesired emission wavelengths and allow the desired ones. While the emission bandpass filter will indeed block some of the desired fluorescence photons, it will make marked improvements in the signal to noise ratio by blocking the majority of noise.

Sample presentation is very important in achieving a higher purity sample signal. It is an easy way to introduce scatter, etc., as other optical components in the light path are primarily in pre-engineered positions. Polymer-based platforms are typically not used in single cell fluorescence microscopy since the polymer of the dish or flask may absorb excitation light and emit background signal. In addition, because a substrate material's noise contribution is a function of its thickness, polymer dishes cause problems because they are thicker than their glass-type counterparts. Finally, polymer dishes tend to have far more irregularities as an optic than do glass-type versions. A few different optical glass types were evaluated for their performance in a fluorescence microscopy system in Paper 1, but generally in most situations a high quality fused silica optic offers the greatest advantages in materials purity and lowest noise generated. Where cost and / or availability prohibit the use of fused silica, there are several quality optics glass types

available, as long as the work is being performed in the visible portion of the electromagnetic spectrum.

To date, some of the most sensitive fluorescence microscopy experiments performed with wide-field detectors in real time have been single molecule detection experiments (Gai et al., 2007; Roeffaers et al., 2007; Xu et al., 2007; Herten, 2008; Blum and Subramaniam, 2009). This manner of single molecule detection involves the association of multiple fluorescent dye molecules with a single large biomolecule. When diluted to approximately 50 pM or less, these single molecules may be observed in solution and distinguished one by one in real time. As nanoparticle fluorescence imaging was the goal of part of the work presented in Paper 3, single molecule imaging was used for the design and testing of sample presentation geometries, as presented in Paper 1. Though two different microscopes and two different cameras were used throughout the body of this work, single molecule and single fluorescent nanoparticle imaging was performed on both to confirm each system's capabilities.

It was the goal of the body of work presented here to use the higher resolution of single cell and single fluorescent nanoparticle imaging to gain a greater understanding of the interactions between some commonly-produced nanoparticles that are in use today and living human carcinoma cells.

References

Abraham, J. L., and McEuen, D. D., 1986. Inorganic particulates associated with pulmonary alveolar proteinosis: SEM and X-ray microanalysis results. Appl Pathol 4, 138-146.

Bertolotti, M., De Pasquale, F., Marietti, P., Sette, D., and Vitali, G., 1967. Laser damage on semiconductor surfaces. J. Appl. Phys. 38, 4088-4090.

Blum, C., and Subramaniam, V., 2009. Single-molecule spectroscopy of fluorescent proteins. Anal. Bioanal. Chem. 393, 527-541.

Brokmann, X., Coolen, L., Dahan, M., and Hermier, J. P., 2004. Measurement of the radiative and nonradiative decay rates of single CdSe nanocrystals through a controlled modification of their spontaneous emission. Phys Rev Lett 93, 107403.

Brysk, M. M., Snider, J. M., and Smith, E. B., 1981. Separation of newborn rat epidermal cells on discontinuous isokinetic gradients of PERCOLL. J Invest Dermatol 77, 205-209.

De Jong, W. H., and Borm, P. J. A., 2008. Drug delivery and nanoparticles: applications and hazards. Int. J. Nanomed. 3, 133-149.

Foucaud, L., Wilson, M. R., Brown, D. M., and Stone, V., 2007. Measurement of reactive species production by nanoparticles prepared in biologically relevant media. Toxicol. Lett. 174, 1-9.

Gai, H., Stayton, I., Ma, Y., Liu, X., and Lin, B., 2007. Visualizing chemical interactions in life sciences with wide-field fluorescence microscopy towards the single-molecule level. TrAC, Trends Anal. Chem. 26, 980-992.

Gu, Y., Wilson, M. A., Fisher, K. J., Dance, I. G., Willett, G. D., Ren, D., and Volkova, I. B., 1995. Fullerenes and shungite. Carbon 33, 862-863.

Handy, R. D., Owen, R., and Valsami-Jones, E., 2008. The ecotoxicology of nanoparticles and nanomaterials: current status, knowledge gaps, challenges, and future needs. Ecotoxicology 17, 315-325.

Herten, D.-P., 2008. Insights into the nanocosmos. Optical single molecule spectroscopy. Chem. Unserer Zeit 42, 192-199.

Jiang, J., Oberdoerster, G., and Biswas, P., 2009. Characterization of size, surface charge, and agglomeration state of nanoparticle dispersions for toxicological studies. J. Nanopart. Res. 11, 77-89.

Krug, H. F., and Klug, P., 2008. Impact of nanotechnological developments on the environment. Nanotechnology 2, 291-306.

Kulshrestha, K. K., Pandya, A., Goyal, P. K., and Mathur, P. C., 1986. The d.c. galvanomagnetic properties in a single crystal of n-type cadmium selenide optimally annealed in molten cadmium. Phys. Status Solidi A 97, 557-563.

Kurnick, J. T., Ostberg, L., Stegagno, M., Kimura, A. K., Orn, A., and Sjoberg, O., 1979. A rapid method for the separation of functional lymphoid cell populations of human and animal origin on PVP-silica (Percoll) density gradients. Scand J Immunol 10, 563-573.

Lin, W., Huang, Y.-w., Zhou, X.-D., and Ma, Y., 2006. In vitro toxicity of silica nanoparticles in human lung cancer cells. Toxicol. Appl. Pharmacol. 217, 252-259.

Lovric, J., Bazzi Hassan, S., Cuie, Y., Fortin Genevieve, R. A., Winnik Francoise, M., and Maysinger, D., 2005. Differences in subcellular distribution and toxicity of green and red emitting CdTe quantum dots. J Mol Med 83, 377-385.

Mount, D. I., and Stephan, C. E., 1967. A method for detecting cadmium poisoning in fish. J. Wildl. Manage. 31, 168-172.

Nero, M., and Tran, B., 2007. An investigation of natural nano-particles for cleaning. NSTI Nanotech 2007, Nanotechnol. Conf. Trade Show 2, 624-627.

Nirmal, M., Murray, C. B., Norris, D. J., and Bawendi, M. G., 1993. Size-dependent spectroscopy and photodynamics of some II-VI semiconductor nanocrystallites (quantunm dots). Proc. SPIE-Int. Soc. Opt. Eng. 1861, 280-284.

Nohynek, G. J., Dufour, E. K., and Roberts, M. S., 2008. Nanotechnology, Cosmetics and the Skin: Is There a Health Risk? Skin Pharmacol. Physiol. 21, 136-149.

Nohynek, G. J., Lademann, J., Ribaud, C., and Roberts, M. S., 2007. Grey goo on the skin? Nanotechnology, cosmetic and sunscreen safety. Crit. Rev. Toxicol. 37, 251-277.

Norris, D. J., Nirmal, M., Murray, C. B., Sacra, A., and Bawendi, M. G., 1993. Size dependent optical spectroscopy of II-VI semiconductor nanocrystallites (quantum dots). Z. Phys. D: At., Mol. Clusters 26, 355-357.

Parthasarathy, G., Srinivasan, R., Vairamani, M., Ravikumar, K., and Kunwar, A. C., 1998. Occurrence of natural fullerenes in low grade metamorphosed Proterozoic shungite from Karelia, Russia. Geochim. Cosmochim. Acta 62, 3541-3544.

Radicati di Brozolo, F., Bunch, T. E., Fleming, R. H., and Macklin, J., 1994. Fullerenes in an impact crater on the LDEF spacecraft. Nature (London) 369, 37-46.

Ren, S. S., Sun, G. H., Ku, C. H., Chen, D. C., and Wu, G. J., 2004. Comparison of four methods for sperm preparation for IUI. Arch Androl 50, 139-143.

Roeffaers, M. B. J., De Cremer, G., Uji-i, H., Muls, B., Sels, B. F., Jacobs, P. A., De Schryver, F. C., De Vos, D. E., and Hofkens, J., 2007. Single-molecule fluorescence spectroscopy in (bio)catalysis. Proc. Natl. Acad. Sci. U. S. A. 104, 12603-12609.

Schlegel, G., Bohnenberger, J., Potapova, I., and Mews, A., 2002. Fluorescence decay time of single semiconductor nanocrystals. Phys Rev Lett 88, 137401.

Schulz, H., Schimmoeller, B., Pratsinis, S. E., Salz, U., and Bock, T., 2008. Radiopaque dental adhesives: Dispersion of flame-made Ta2O5/SiO2 nanoparticles in methacrylic matrices. J. Dent. (Oxford, U. K.) 36, 579-587.

Shabalina, L. P., 1966. Comparative toxicity of certain cadmium compounds. 115-116.

Shimizu, K. T., Woo, W. K., Fisher, B. R., Eisler, H. J., and Bawendi, M. G., 2002. Surface-enhanced emission from single semiconductor nanocrystals. Phys Rev Lett 89, 117401.

Tengvar, C., Hultstrom, D., and Olsson, Y., 1983. An improved Percoll density gradient for measurements of experimental brain edema. Addition of sucrose to an isotonic gradient in an attempt to balance osmotic conditions during density determinations. Acta Neuropathol 61, 201-206.

Tyagai, V. A., and Kolbasov, G. Y., 1971. Mechanism of cathodic iodine reduction and noise on cadmium sulfide and cadmium selenide semiconductor electrodes. Elektrokhimiya 7, 1722-1725.

Viscardi, R. M., Ullsperger, S., and Resau, J. H., 1992. Reproducible isolation of type II pneumocytes from fetal and adult rat lung using nycodenz density gradients. Exp Lung Res 18, 225-245.

Wang, X., Ma, Q., Li, B., Li, Y., and Su, X., 2007. The preparation of CdTe nanoparticles and CdTe nanoparticle-labelled microspheres for biological applications. Luminescence 22, 1-8.

Xu, X.-H. N., Song, Y., and Nallathamby, P., 2007. Probing membrane transport of single live cells using single-molecule detection and single-nanoparticle assay. Chem. Anal. (Hoboken, NJ, U. S.) 172, 41-70.

PAPER

1. Single Molecule Spectroscopy and Single Cell Analysis: Applications in Nanoparticle Bioanalysis

Abstract

Fluorescence microscopy has long been an invaluable tool used for probing chemical and biological systems. In this work, we evaluate different modes of sample presentation in laser-excitation fluorescence microscopy with wide-field intensified charge-coupled device camera detection for single molecule and single cell imaging. The ultimate goal of the work was to use these sample presentation models for the analysis of single fluorescent semiconductor nanoparticles, single living cell samples, and for their simultaneous imaging. We present the use of microfluidics as imaging performed in square capillaries. Laser total internal reflection was utilized in all live cell imaging configurations, which consisted of the three following geometries: Single right angle prism, flat prism and a combination right angle prism – microscope slide. Microscope slide materials were evaluated for their intrinsic noise levels in the technique. Fused silica produced the least noise of the materials tested. All sample presentation geometries shown here were successful in imaging the samples and the combination right angle prism – microscope slide provided the greatest advantages in our instrument setup.

Keywords

Single molecule imaging; single cell imaging; fluorescence microscopy

Introduction

Single molecule spectroscopy has been in use for over two decades [1-5]. The principles by which single molecule detection is achieved, using wide-field detectors such as intensified charge-coupled device (ICCD) cameras, are largely identical to those used in single cell fluorescence microscopy. Foundational in these techniques is the maximization of analyte signal while simultaneously minimalizing noise signals. The work presented in this section laid the foundation for nanoparticle analysis in living cells at the single cell level.

The single molecule detection work performed here consisted of the approach that employs multiple fluorophores attached to single biological molecules to facilitate their direct imaging by way of fluorescence microscopy. Large biomolecules such as DNA can accept hundreds of dye molecules, while others like immunoglobulins are typically labeled with ten fluorophores or less each. Though the quantum event is somewhat dissimilar, the detection of single fluorescent nanocrystals falls within this range of required sensitivity.

Single molecules, like single nanocrystals, are too small to be viewed by conventional optical microscopy alone. Therefore, the detection of fluorescent quantum events is used to view them indirectly. For example, organic dye molecules typically

contain a system of conjugated bonds, and where a pi electron absorbs light and enters an excited state. The subsequent loss of some energy in the form of heat, rotations or vibrations, and the electron's relaxation and emission of a longer wavelength light constitutes typical fluorescence [6]. In the case of semiconductor nanocrystals, a photon of light is absorbed and an electron is excited into the conduction band of the semiconductor crystal. Its subsequent relaxation and the emission of a longer wavelength of light constitute typical nanocrystal fluorescence [7-9]. While both systems can be susceptible to photobleaching, the fluorescent nanoparticles show much more resistance to it especially after a thin stabilizing shell has been added around the semiconductor core [10, 11].

In all cases, the fluorescence intensity is limited by its quantum yield. This is the population of excited electrons which yield fluorescence following excitation compared to the total number of excited electrons. Because of quantum efficiency limitations, fluorescence signals are typically of relatively low intensity. For this reason, it was necessary to develop sample presentation geometries with sufficient sensitivity thresholds to capture the fluorescent quantum events. Among the aspects studied were inherent noise levels in sample presentation optic materials and solution background noise contributions. As the final goal was to perform fluorescence analysis in living cells at the single cell level, most of the sample presentation design was focused there.

Experimental

Chemicals

Lambda-DNA was purchased from Fermentas Inc. (Glen Burnie, MD, USA).The fluorescent dyes bis-(1,3-dibutylbarbituric acid)trimethine oxonol ($DiBAC_4(3)$), Yoyo-I and Alexa Fluor-488 carboxylic acid, succinimidyl ester were purchased from Molecular Probes, Invitrogen (Carlsbad, CA, USA). Fetal bovine serum (FBS) and Ham's F-12 medium with L-glutamine but without phenol red were purchased from MidSci (St. Louis, MO, USA). Bovine serum albumin (BSA), human IgG, Mouse anti-human IgG, rabbit anti-bovine serum albumin IgG, penicillin-streptomycin, gly-gly, $FeSO_4$, $MgSO_4$, and $ZnSO_4$ were purchased from Sigma (St. Louis, MO, USA). Polyvinyl pirrolidone (PVP) (average molecular weight = 1.3×10^6 g/mol), polyethylene oxide (PEO) (average MW = 6.0×10^5), $CaCl_2$, NaCl, and D-glucose were bought from Aldrich (Milwaukee, WI, USA). Potassium chloride, dimethylsulfoxide (DMSO), Na_2HPO_4, $NaHCO_3$ and 22 mm square cover glasses were purchased from Fisher Scientific (Pittsburg, PA, USA). Sephadex G-50 gel column material (dry) was purchased from Pharmacia LKB Biotechnology, Inc. (Piscataway, NJ, USA). All solutions were made using ultrapure DI-water prepared using a Simplicity 185 system (Millipore, Bedford, MA, USA).

Optics

Fluorescent silica-coated nanoparticles were synthesized by Dr. Jeffrey Winiarz (Missouri S&T) based on a method from the literature [12]. Their composition was as follows: a CdSe core was coated with a shell of CdS, which was finally coated with amorphous SiO_2. Particle diameter was characterized by TEM to be 13 nm. Square fused

silica capillaries were purchased from Polymicro Technologies (Phoenix, AZ, USA). The square capillaries used were of two sizes: the length of one side (inner capillary wall) was either 50 or 75 μm. Large right angle prisms (A=B=C= 1 inch) and mirrors were purchased from Melles Griot (Rochester, NY, USA). Fused silica microscope slides were purchased from Technical Glass, Inc. (Painesville Twp., OH, USA). Small right angle prisms (A=B=C= 1cm) and cylindrical lenses were purchased from Surplus Shed (Fleetwood, PA, USA). The attenuated total reflectance (ATR) plate was manufactured by Harrick Scientific Corporation (Ossining, NY, USA). Ultraviolet-curable optics glue was purchased from Edmund Optics (Barrington, NJ, USA). A Foturan glass sample was provided by Dr. Hailong Tsai (Missouri S&T), and Borofloat 33 glass, Flat Panel 1737 glass and fused silica samples were donated by Dr. Lance Koutny (independent consultant) for materials background noise testing. An Olympus BX-51 upright microscope was used (Tokyo, Japan). The ICCD camera was an I-Pentamax with a generation III intensifier, manufactured by Princeton Instruments (Trenton, NJ, USA). A 40 x objective was used to collect all images using the square capillary. A 100 x objective was used to collect all images using flat sample presentation geometries unless otherwise noted.

Cell Culture

The human lung cancer cell line A549 was purchased from American Type Culture Collection (ATCC) (Manassas, VA, USA). Cells were maintained in Ham's F-12 medium supplemented with 10% FBS and 100 units/ml penicillin, 100 μg/ml streptomycin, and grown at 37 ºC in a 5% CO_2 environment with 100% humidity. In

order to facilitate imaging, cells were cultured on sterile No. 1.5, 22 mm square cover glass.

The buffer used in these cell imaging experiments contained $CaCl_2$, NaCl, D-glucose, $FeSO_4$, $MgSO_4$, $ZnSO_4$, KCl, Na_2HPO_4, and $NaHCO_3$ at the same concentrations found in Ham's F-12 culture medium. The buffer was adjusted to pH 7.2 and filtered using a sterile 0.2 µm polyethersulfone filter. In order to image cell membranes, the fluorescent dye $DiBAC_4(3)$ was added at a concentration of 1.5 µM to the medium in the Petri dish and allowed to incubate for 30 minutes prior to fluorescence imaging.

Labeling of DNA

Lambda-DNA was labeled with the fluorescent dye Yoyo-I. First, a 50 mM gly-gly buffer was made and adjusted to pH 8.2, filtered with a 0.45 micron filter and degassed. A quartz plate was placed over the wide-mouth bottle containing the gly-gly buffer and a UV lamp set at 254 nm was used to photobleach the buffer overnight. Gly-gly buffer was used to dilute the lambda-DNA to 50 pM. Yoyo-I was diluted 1:100 times in DMSO to make a stock solution. It was then added to the DNA solution at a ratio of approximately one dye molecule to every five DNA base pairs. This solution was placed in the dark at 4 ºC for 30 minutes to allow the dye to attach before use. Yoyo-I does not fluoresce when in solution, but yields bright fluorescence after being adsorbed in the minor groove of the DNA structure. It therefore served as an ideal fluorescent marker for DNA in single molecule spectroscopy, as it required no sample clean-up to remove the

excess dye. However, as the dye molecules may attach and detach, a sufficient concentration was required in the DNA solution, even if the DNA was diluted.

Labeling of Antibodies

Human IgG and Rabbit anti-bovine serum albumin IgG were covalently labeled with Alexa-Fluor 488 carboxylic acid, succinimidyl ester according to the product instructions. Briefly, they were as follows: each antibody was diluted to 10 mg protein / ml with 0.15 M $NaHCO_3$ buffer at pH 8.3. This solution was sonicated briefly to break up any protein agglomerates. Then, 1.0 M $NaHCO_3$ buffer and Alexa-Fluor 488 dye were added and the solution was stirred slowly for one hour.

Purification of Labeled Antibodies

Antibodies labeled with Alexa-Fluor 488 were purified using a gel size exclusion column. Phosphate-buffered saline (PBS) at pH 7.4, made using the ATCC formulation, was used as the mobile phase. It was also photobleached overnight with UV light, filtered with a 0.45 micron filter and degassed. Sephadex-50 dry gel powder was expanded in approximately 40 ml of PBS in a hot water bath for 2-3 hours and stirred gently with a glass stir rod occasionally, to release air bubbles. A one - cm diameter glass column was prepared with glass wool at its tip to retain the gel. Gel slurry was loaded in the column, taking care to prevent the trapping of air bubbles. The column was flushed with running buffer to equilibrate the compacting of the gel, which resulted in a gel column approximately 30 cm tall. The labeled antibody solution was loaded onto the column and washed through using running buffer. The single band was observed to separate into two

bands. The first eluding band was collected as fractions were collected every 0.6 ml. Each fraction was measured on a Beckman DU 640B UV-vis spectrophotometer, scanning the absorbance from 200 – 1100 nm to confirm the presence of covalently-bound dye and the absence of loose dye molecules. Fractions containing the labeled antibodies were combined and the absorbance was measured at 280 and 495 nm. Using an equation provided by Molecular Probes, the protein concentration and the degree of labeling were calculated based on the absorbance values.

Optical Measurements in a Square Capillary

Use of a square capillary for single molecule imaging required the simplest optical arrangement of the geometries presented in this work. A custom mount held the capillary so that the center of the capillary was in the focal plane of the microscope objective, running perpendicular to the laser. The laser beam was then cast directly upon the capillary window. Next, a cylindrical lens mounted on a three dimensional positioner was placed laterally directly in front of the capillary window distanced by its focal length, so that the laser beam was focused into a horizontal line that impinged upon approximately three mm of the center of the capillary. Finally, with fluorescently-labeled DNA in the capillary, the lens's xyz positioner was fine tuned to excite the molecules in the capillary but not reflect off the capillary walls in such a way that created excessive noise. Often, laser scatter on the inner walls of the capillary would be minimized to nearly non-observable levels. Square capillaries of two different sizes were tried. The width of the capillary's inside channel was either the larger size of 75 μm or the smaller size of 50 μm. The width of one side of a capillary's external dimension was

approximately 350 µm for both sizes. For three views of the capillary mount, see Figure 1. When applying the laser, a mechanical shutter was used to limit excitation time to 10 msec. with 100 msec. delays between pulses, which was effective in the minimalization of sample photobleaching.

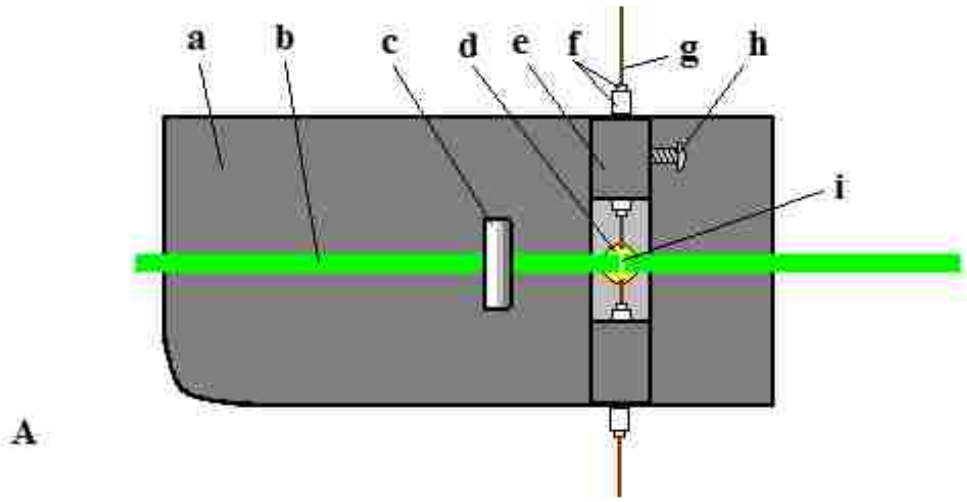

Figure 1. Components of the single molecule imaging capillary mount.
A) Top-down view
The capillary drawn was in reality approximately 25 cm in length, so that the ends could be secured inside vials of solution.
Capillary mount features were as follows:
a) Capillary mount platform, b) laser beam, c) cylindrical lens, d) hole drilled for light from microscope lamp, e) vertical capillary support, f) PTFE capillary support tubes, g) square capillary, h) mounting screw, i) capillary window.

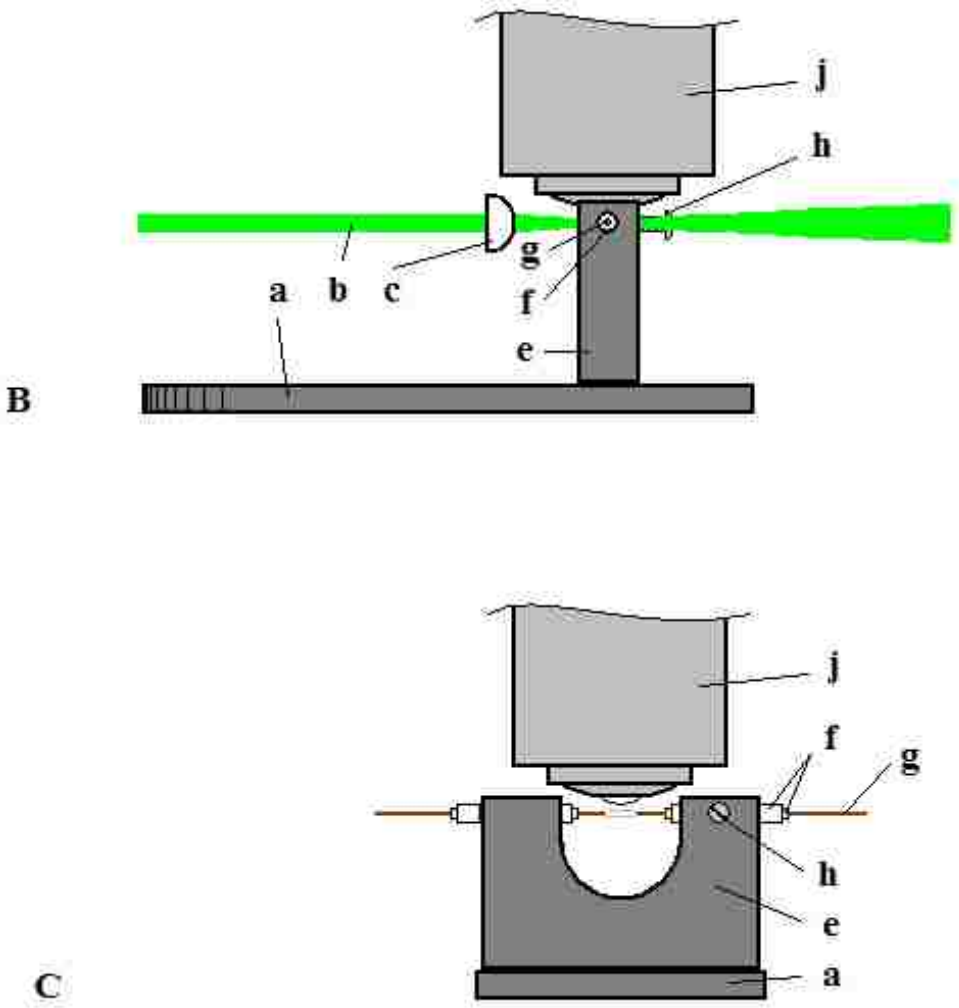

Figure 1 (cont.) Components of the single molecule imaging capillary mount.
B) Side view and C) End-on view.
Capillary mount features were as follows:
a) Capillary mount platform, b) laser beam, c) cylindrical lens, e) vertical capillary support, f) PTFE capillary support tubes, g) square capillary, h) mounting screw, i) capillary window, j) 40 X dry objective.

To create electrophoretic flow, the ends of the capillary were placed in vials of gly-gly buffer for DNA, or PBS for immunoglobulins. Nickel-platinum electrodes were

placed in the vials, with one attached to an adjustable high voltage power supply and the other thoroughly grounded. Care was taken to maintain the vials at equal heights above the optical table, to prevent gravity from causing flow in the capillary.

Single molecule imaging in a square capillary required the capillary be pre-coated so as to prevent the adsorption of analyte molecules onto the capillary surface. For this purpose a 0.2% PVP solution was prepared in ultrapure water. PVP is a nonionic water-soluble polymer that has been used in the literature in capillary electrophoresis (CE) systems for this purpose [13-15]. The capillary was rinsed with this solution for ten minutes prior to rinsing with running buffer and was renewed every hour for five minutes. For protein samples, 0.3% PEO dissolved in PBS was used as a sieving matrix to separate the proteins based on their size. In this way, single immunoglobulins were distinguished from their immunocomplexes in solution.

Optical Measurements on a Flat Surface

The sample holders which presented a flat surface were designed primarily for live cell imaging. Live A549 cells were cultured on sterilized 22 mm square cover glasses in Petri dishes. When the cells were to be imaged, the side of the cover glass lacking cells was washed with ultrapure water and dried with a Kimwipe®. Care was taken to ensure the water did not contact the side of the glass to which the cells were attached. The cells were rinsed with imaging buffer. Strips of 127 µm-thick polytetrafluoroethylene (PTFE) sized 25 by 3 mm were used to support opposite sides of the cover glass, and 50 µl of imaging buffer was inserted to fill the void between the cover glass and the flat optic. When live cell samples were to be imaged for up to one hour, further measures were

taken to stabilize the cells. A 3 ml reservoir exiting via a capillary tube delivered a slow and steady flow of imaging buffer to one end of the sample while a wick removed excess buffer at the opposite end. Rubber bands were used to strap the cover glass firmly over the PTFE spacers and the prism to prevent floating or shifting. These measures were necessary over periods of time longer than 20 minutes due to the buffer's evaporation along the cover glass edges. Between samples the flat optic was washed with 0.1 M HCl and ultrapure water. In addition to live cell imaging, single molecules and single nanoparticles could also be imaged using these presentations. A clean cover glass was used and the solution or suspension of choice was placed beneath. The laser beam pulse timing used in all flat surface optic presentations was identical to the timing used in the square capillary applications.

The first flat presentation sample holder used employed a 1-inch right angle prism. (See Figure 2.) The aluminum prism mount held the right angle prism so that a sample placed in the center of the prism's hypotenuse was perpendicular to the microscope objective. The laser beam was manipulated in the following manner: A 15 cm focal length convex lens was introduced approximately 13 cm prior to the sample located in the objective focal plane. This slightly defocused laser beam was desired because presented a smaller phototoxicity hazard in living cells and had a diameter at the objective focal plane wide enough to fill the ICCD camera's field of view. A round mirror on an adjustable mount then directed the laser to reflect off a small square mirror lying on the bottom of the prism holder. The laser passed through the prism, reflecting internally and exited through the far side. The adjustable round mirror was used to fine

tune the laser beam's position so that it illuminated the sample located in the objective's field of view.

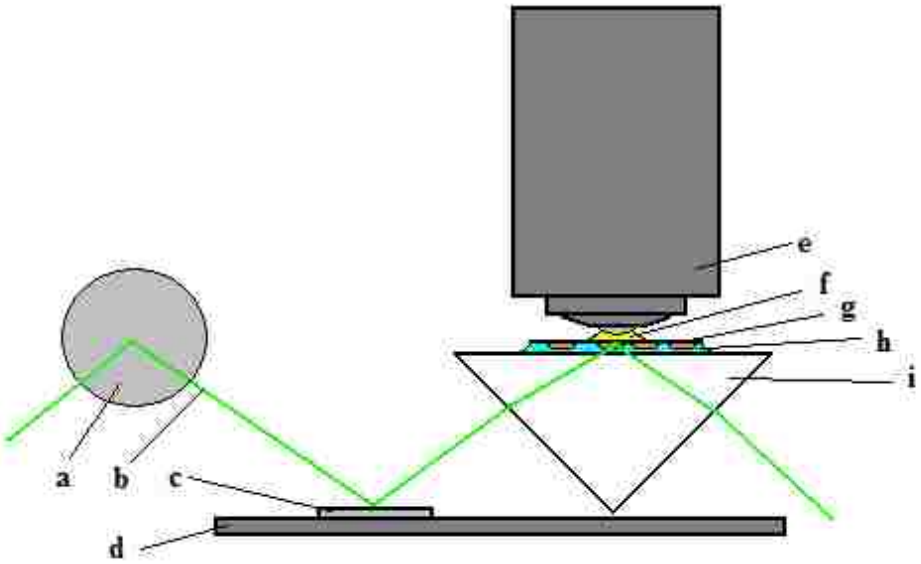

Figure 2. Right angle prism mount in use for cell imaging.
a) mirror, b) laser beam, c) moveable square mirror, d) aluminum prism mount structure, e) 100 X oil objective, f) immersion oil, g) cover glass with cells attached to the underside, h) imaging buffer, i) quartz right angle prism. Not shown: a 15 cm focal length convex lens positioned in the laser beam's path before the round mirror (a).

The second presentation of the sample on a flat optical surface incorporated a flat prism. Figure 3 shows the shape and dimensions of the optic used, which was originally manufactured to function as a quartz ATR plate. This was ideal, as attenuated total reflectance applies a totally internally reflected beam, which is how the optic was used here. (See Figure 4.) A custom flat aluminum slide holder was made to support and hold the flat prism, and allowed it to be manipulated on the microscope stage. It had no aluminum under the center of the optic, in order to avoid disturbance of the laser beam as

it reflected down the length of the prism. The same system was used here to place the cell sample on the optic as before, and the cover glass was positioned approximately ¾ of the distance along the prism surface. And, as before, a 15 cm focal length convex lens was positioned so as to deliver a slightly defocused laser beam to the sample.

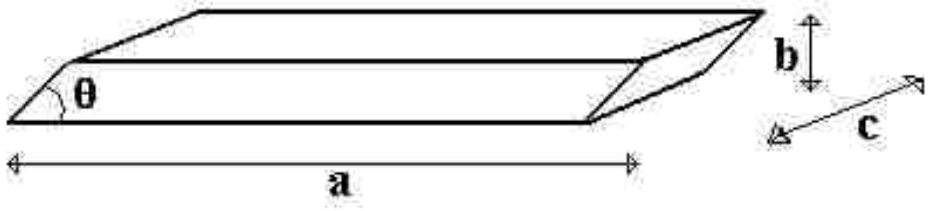

Figure 3. Dimensions of quartz ATR plate.
a) 51.5 mm, b) 1.5 mm, c) 16 mm, and θ = 45 degrees. The top, bottom and angled ends of the optic were polished to an optical flatness.

The third presentation of the sample on a flat optical surface required the in-house combination of two manufactured optics. A small (A=B=C= 1cm) right angle prism was attached to one end of a fused silica microscope slide (1 x 3 inches x 1 mm thick) using UV-curable optics adhesive. When fully cured, the optics glue had a refractive index essentially the same as quartz and the commonly-used optical glasses. As a result, the prism and slide behaved as a single continuous optic. The orientation is shown in Figure 5. As before, the convex lens was used to deliver a slightly defocused laser beam to the sample, which was also applied as before. Laser beam position fine tuning was done with a round mirror held in an adjustable mount. In this geometry, the laser entered the right angle prism and traveled the length of the microscope slide, reflecting internally. Samples

were positioned at the far end, as before. Phase contrast microscopy was possible with this geometry, so the microscope condenser was brought to focus on the sample from below.

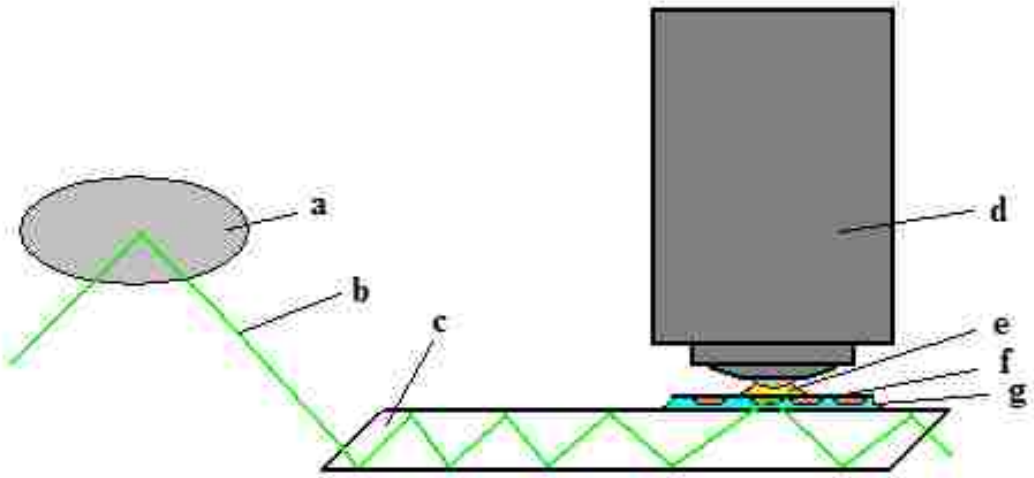

Figure 4. Cell imaging using an ATR plate geometry.
a) Mirror, b) laser beam, c) quartz ATR plate, d) 100 X oil objective, e) immersion oil, f) cover glass with cells attached to the underside, g) imaging buffer. Not shown is a 15 cm focal length convex lens positioned in the laser beam's path before the round mirror (a).

Since background noise is a perpetual consideration in fluorescence microscopy, different materials were tested for the background noise created when the excitation laser passed through them. The results of this test were used to choose the material from which the microscope slide for the configuration in Figure 5 would be made. It was accomplished by placing the different materials being tested on the large prism

arrangement (Fig. 2) with immersion oil between them. The laser was applied without a sample present and the ICCD camera was used to measure the background counts present. The materials tested were as follows: Foturan glass, borofloat glass, flat panel glass and fused silica.

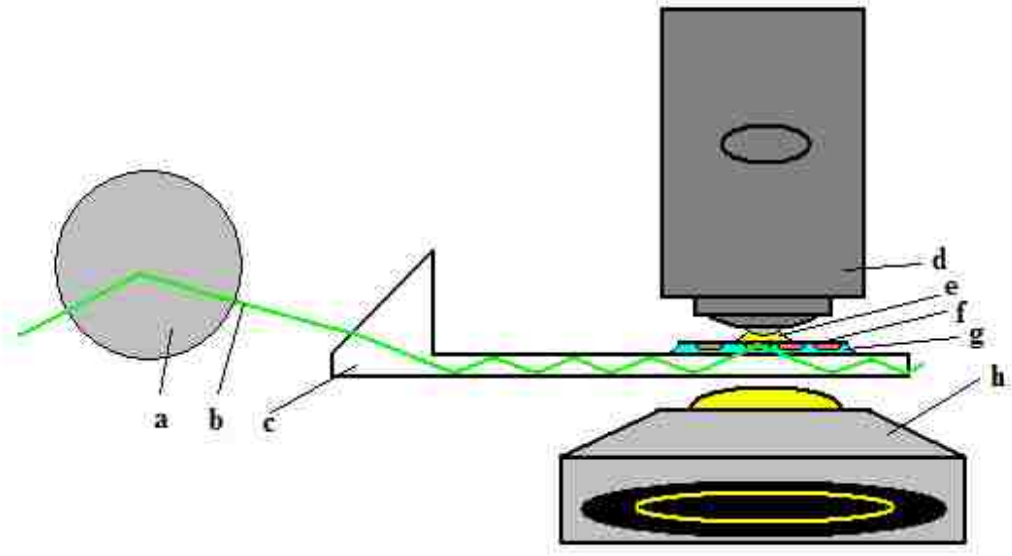

Figure 5. Modified microscope slide with small right angle prism used for cell imaging. a) mirror, b) laser beam, c) microscope slide with right angle prism attached with optics glue, d) 100 X oil phase contrast objective, e) immersion oil, f) cover glass with cells attached to the underside, g) imaging buffer, h) microscope condenser with phase contrast ring. Not shown is a 15 cm focal length convex lens positioned in the laser beam's path before the round mirror (a).

Results and Discussion

The use of a square capillary for single molecule and single nanoparticle detection was successful. Unique compared to the other sample presentation methods used, it provided a way for the external laser to be focused directly onto the sample without the use of prisms. Figure 6 shows lambda-DNA labeled with Yoyo-I in a square capillary. As this biomolecule-fluorophore combination yielded the strongest fluorescence of the samples studied, it served as the standard of choice for optics alignment and system performance analysis.

Figure 6. Yoyo-I labeled lambda-DNA molecules imaged one by one by fluorescence microscopy using a square capillary.

The degree of fluorescent dye labeling for anti-BSA IgG molecules was calculated to be 7.3 dye molecules per protein. Human IgG immunoglobulins were labeled with an average of 10.9 dye molecules per protein. These were imaged in the square capillary in the PEO sieving matrix, as shown in Figure 7.

A  B 

Figure 7. Single molecule spectroscopy of dye-labeled immunoglobulins.
A) Anti-BSA, B) Human IgG.

Each antibody was combined with its antigen and imaged again while under electrophoretic flow in the PEO sieving matrix. Figure 8 shows different video frames of the same data file. In these images, bound and unbound anti-BSA molecules are discernible. Two parameters are necessary to determine their state: their fluorescence intensity must be approximately the same, while their velocities must be distinctly different. Figure 8 also shows dye-labeled human IgG molecules and those which have been bound to their complementary antibody (combined with unlabeled anti-human IgG). As an example, the mobilities of single human IgG molecules were compared with their immuno-complexed counterparts in Figure 9.

A

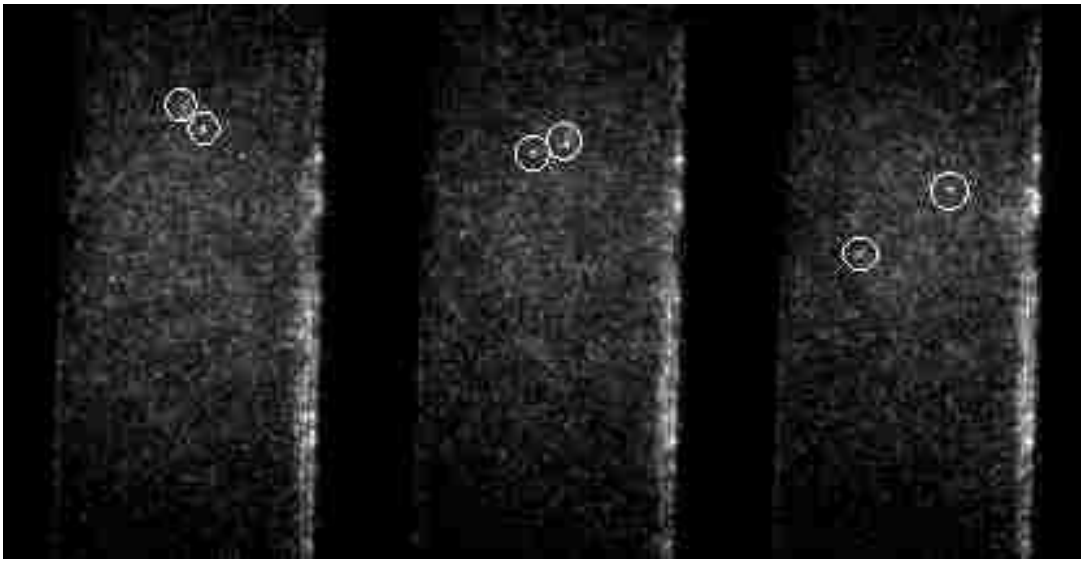

B

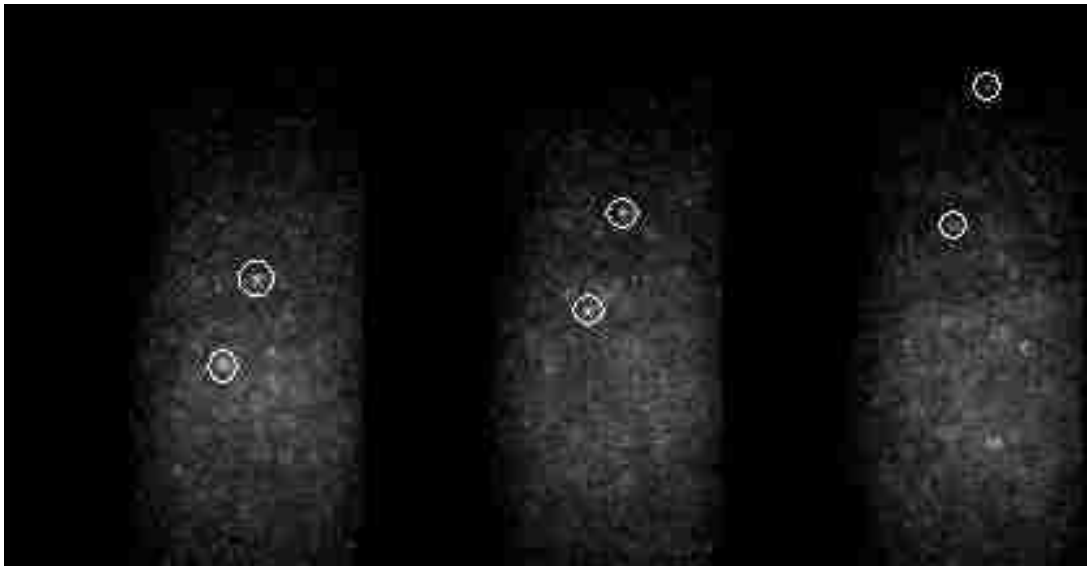

Figure 8. Difference in mobilities of dye-labeled antibodies versus their imunocomplexes. A) Anti-BSA molecules as single molecules and as immunocomplexes. Note the difference in mobility; the immunocomplex, with its greater mass, travels more slowly. B) Labeled human IgG (acting as antigen) and its immunocomplex with anti-human IgG.

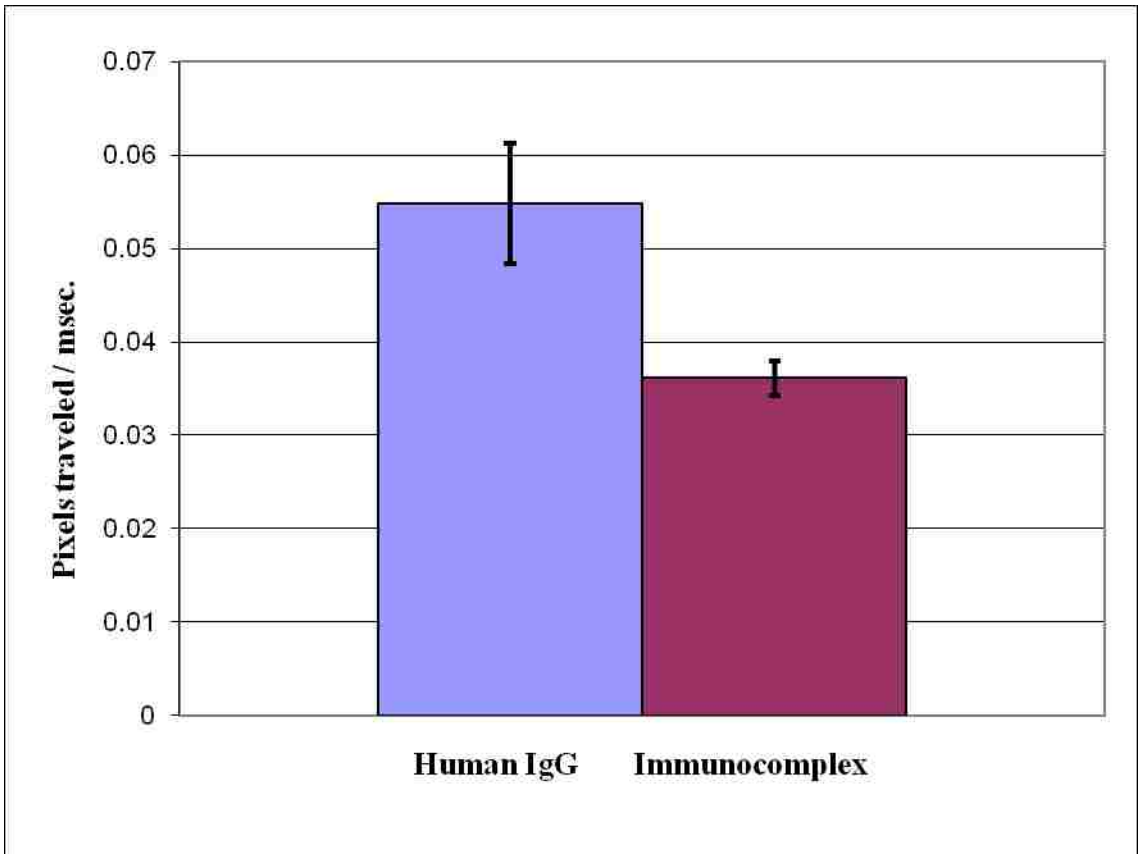

Figure 9. Mobility of unbound human IgG molecules compared to the mobility of those bound by a complementary anti-human IgG antibody.
Units of mobility are in camera pixels traveled per millisecond.

The final sample to be imaged using the square capillary was fluorescent semiconductor nanoparticles. The sample treatment was the same as with previous analytes, except that the solvent used was simply ultrapure water. To illustrate the importance of photobleaching the solvent prior to single molecule experiments, Figure 10 shows nanoparticles suspended in both normal and photobleached ultrapure water. In addition, since there were no electrolytes added to the solvent, no electrodes were used to produce electroosmotic flow. Instead, pressure was used to introduce the nanoparticle

suspension into the capillary, and the rate of flow was adjusted by lowering one of the vials into which were placed the ends of the capillary.

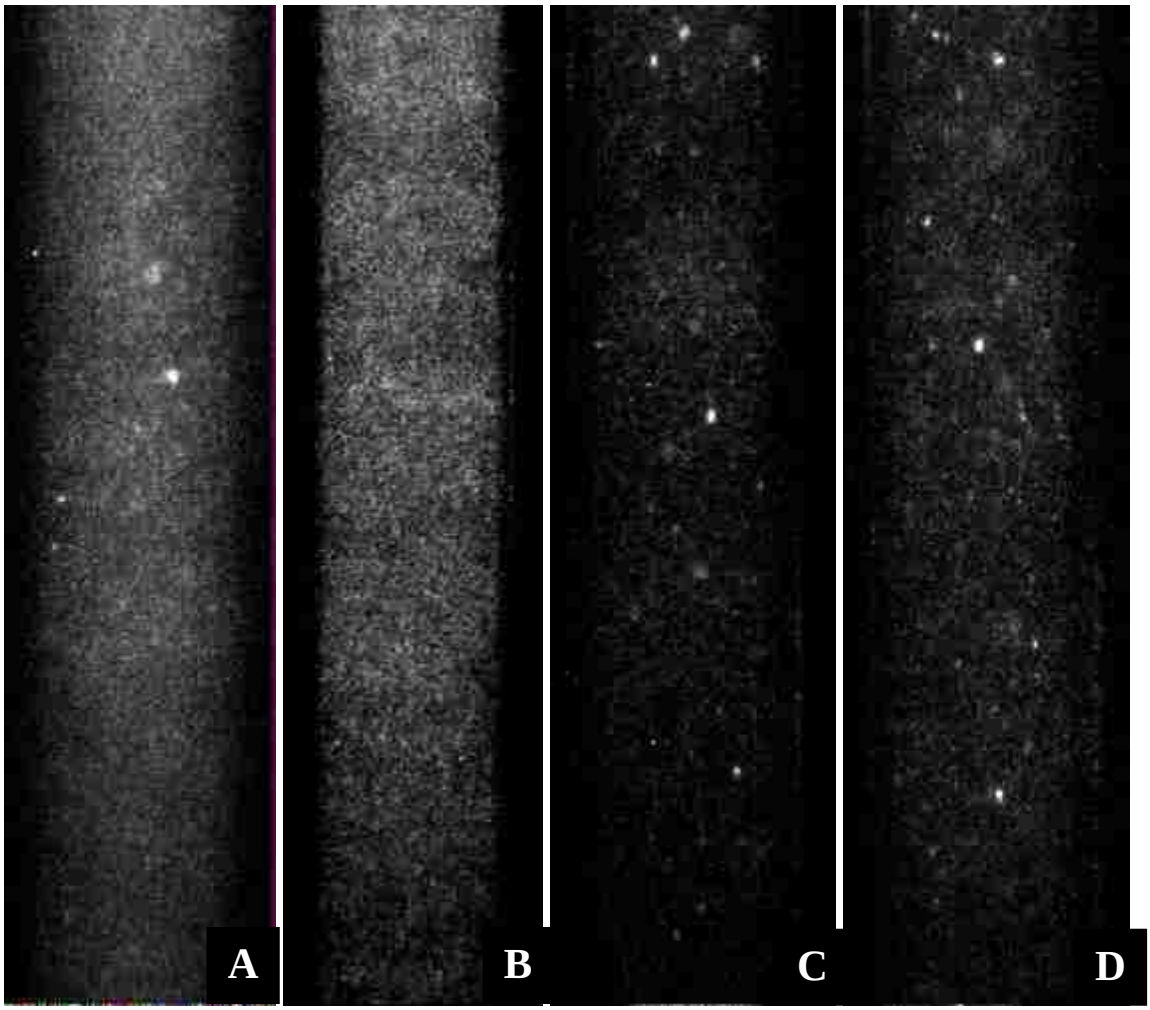

Figure 10. Importance of solvent photobleaching in single fluorescent nanoparticle imaging in a square capillary.
A and B) Fluorescent nanoparticles in ultrapure water.
C and D) Same particles sample, suspended in the same ultrapure water after overnight photobleaching of the solvent.

The first geometry used to present a flat sample surface proved to be the simplest in operation. The 1-inch right angle prism experienced just a single internal reflection of the laser beam. (See Figure 2.) Single molecules could be imaged in two ways: by excitation using an evanescent field laser created by total internal laser reflection or by directly impinging the laser upon the sample. (See Figure 11 A and B, respectively.) Total internal reflection produced a greater signal to noise ratio, but only excited molecules less than 200 nm from the prism surface. The reason there is so little background in Fig. 11 B is that the excitation field's intensity decreases exponentially as distance from the prism surface increases. Direct illumination of the sample molecules allowed the imaging of species in free solution, but generated higher background noise. Much of the new background noise was out-of-focus DNA molecules. Cells with the membrane dye $DiBAC_4(3)$ were clearly imaged via direct illumination. (See Figure 12.)

A 

Figure 11. Labeled lambda-DNA imaged using a large right angle prism.
A) Excitation using an evanescent field layer.

B 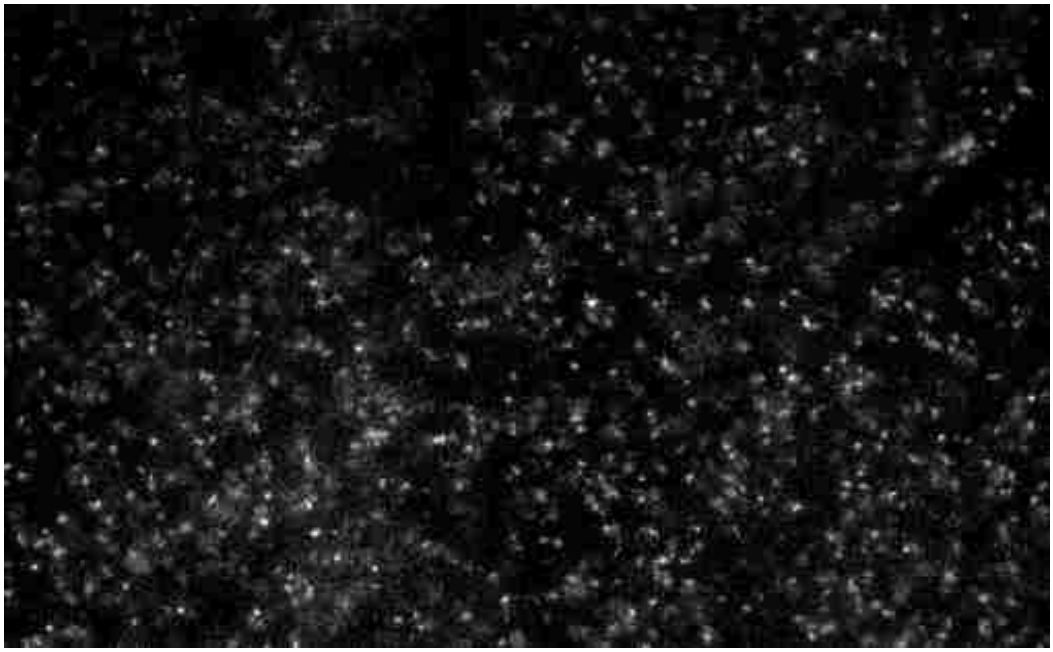

Figure 11 (cont.). Labeled lambda-DNA imaged using a large right angle prism. B) Excitation by direct illumination of laser beam.

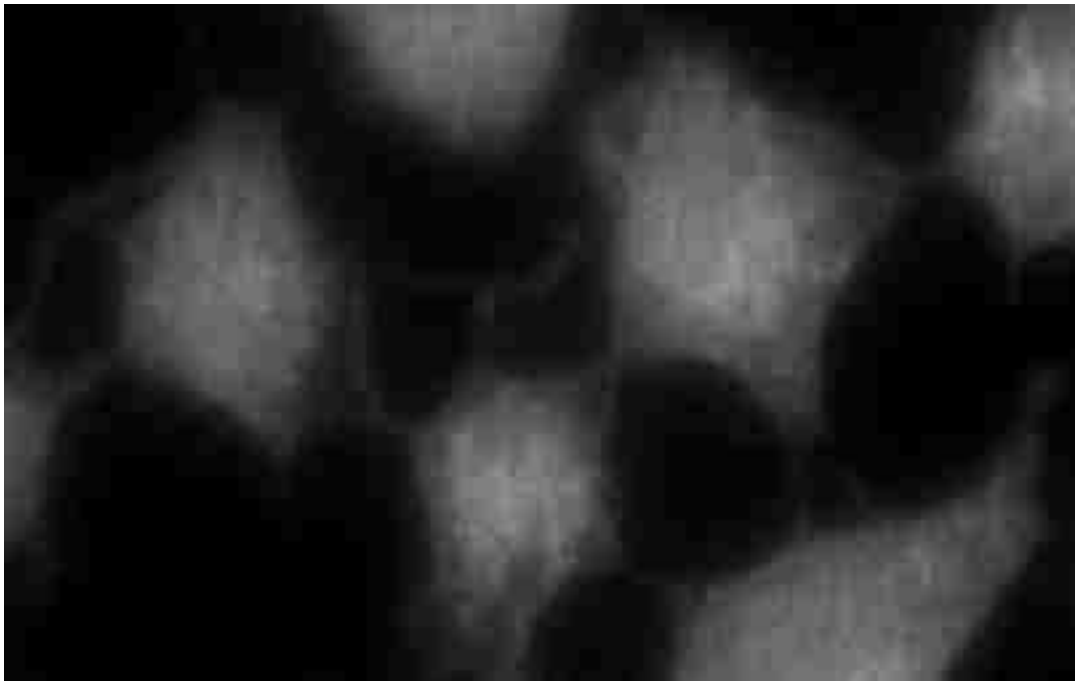

Figure 12. Cell fluorescence from living cells placed on a large right angle prism.

The flat prism configuration served equally well in imaging labeled DNA molecules at its surface. The angle of the laser employed caused the laser to totally internally reflect down the length of the prism, illuminating the sample at the end. (See Figure 13.) It was also used to image cells labeled with membrane dye, and they were clearly visible. (See Figure 14.)

The final flat sample presentation configuration was the modified small right angle prism – microscope slide, as shown in Figure 5. Figure 15 shows dye-labeled cells, and the image is of the same quality as with previous sample configurations. In addition, Figure 16 shows phase contrast images taken on the same sample presentation mount. This was a necessary feature since, with fluorescent nanoparticles, clearly visible cell membrane boundaries needed to confirm if a nanoparticle was inside or associated with a cell or not. Figure 16 shows fluorescent nanoparticles on the prism-slide sample mount. The image was duplicated in reverse color for ease of viewing.

Figure 13. Labeled lambda-DNA imaged on the flat prism.

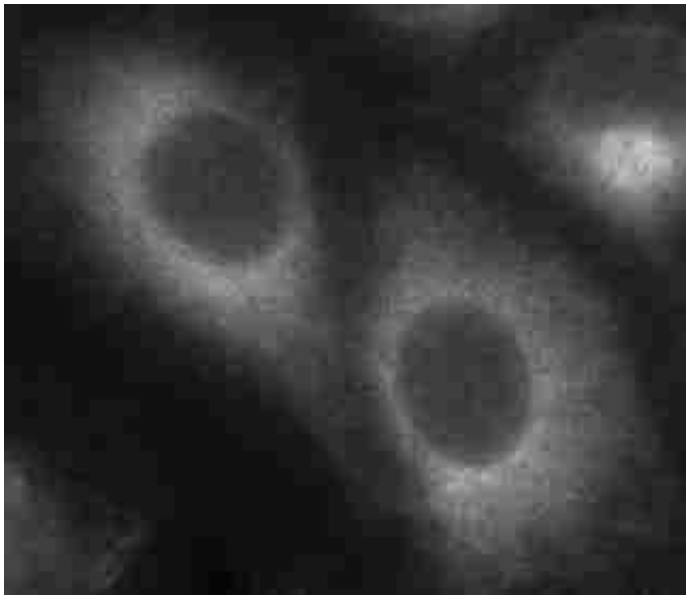

Figure 14. Cells labeled with membrane dye, imaged using the flat prism.

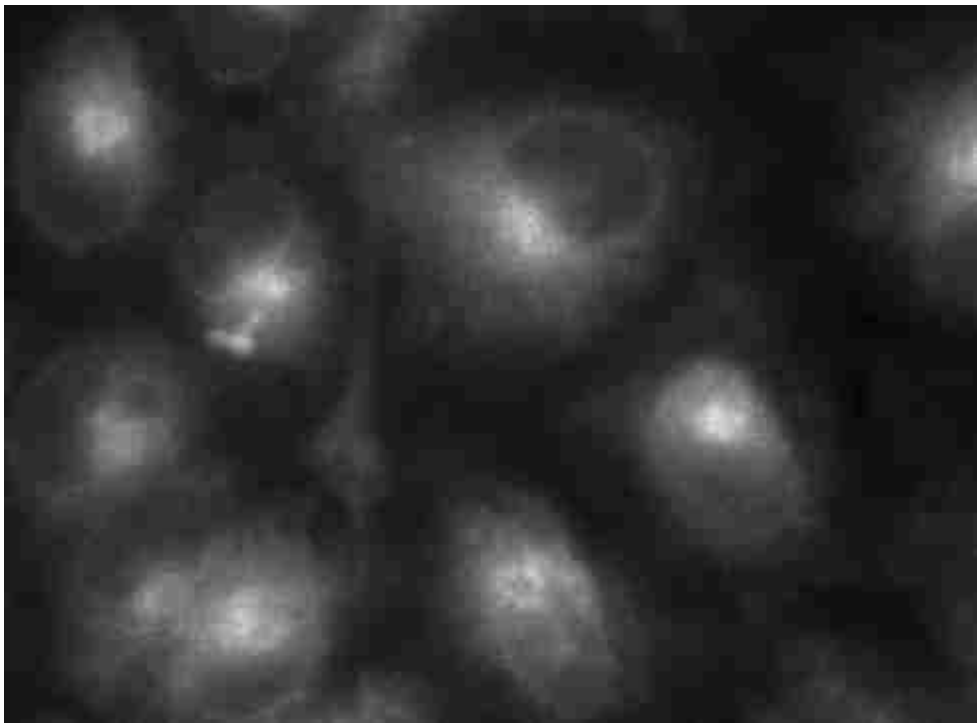

Figure 15. Fluorescent images of cells labeled with membrane dye, imaged using the modified prism-microscope slide.

Figure 16. Phase contrast images collected using the prism-slide sample mount. A 40 x objective was used to obtain this image.

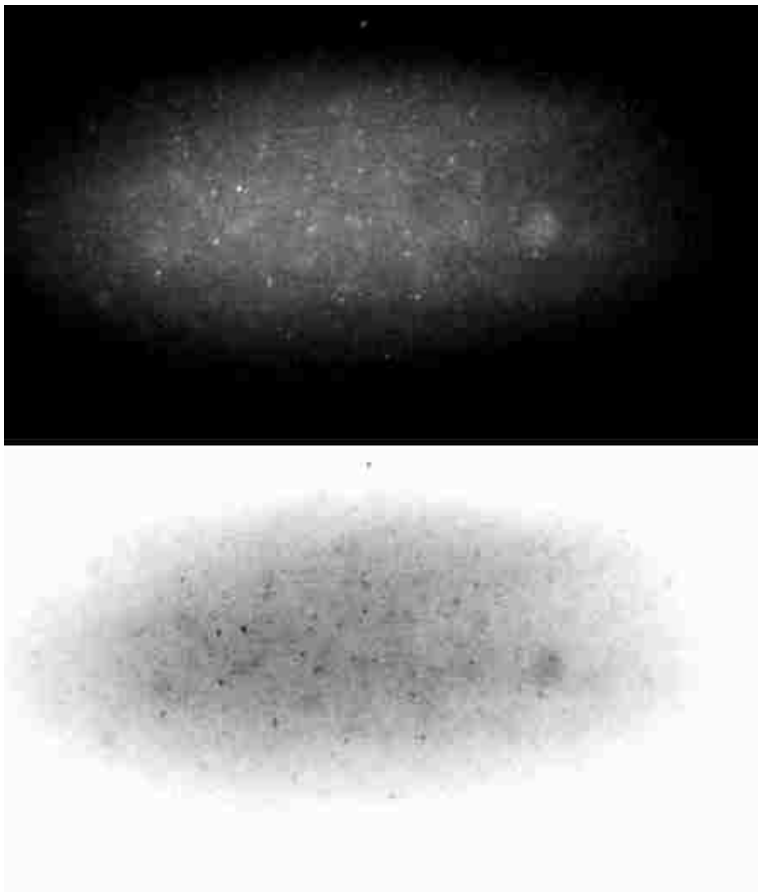

Figure 17. Fluorescent nanoparticles imaged on the combination prism-slide. A 40x objective was used. The image was recreated in reversed coloring for ease of viewing.

Different materials were tested for inherent background noise in the single cell imaging system, so that the best available material would be used to build the modified microscope slide configuration. Table 1 shows the different materials tested and the average signal collected by the ICCD camera during the test. All materials tested were optics grade materials. For this test, the laser was adjusted to maximum power and the camera was operated at 85% intensification, to simulate extreme experimental conditions. During the tests, all materials appeared to exhibit uniform noise, and no “bright or dark spots” were noted.

Table 1. Background noise associated with different sample optic materials.

Material Composition	**Average Camera Pixel Intensity**
Camera Dark Current	63.29
Quartz (fused silica)	66.69
Borofloat 33 glass	76.32
Flat Panel 1737 glass	85.98
Foturan glass	147.00

Cover glass materials were also tested for background noise contributions. Placed over ultrapure water on the large right angle prism, a standard glass cover glass was compared to a quartz cover glass. The resulting images are shown in Figure 18. As a control, the prism, without any water or cover glass, was imaged to identify any background that might be originating there.

A 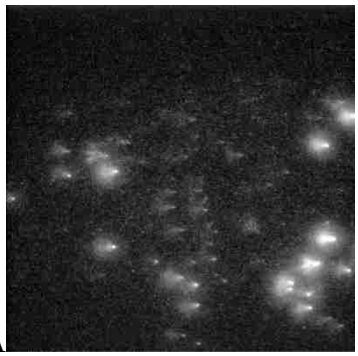 B 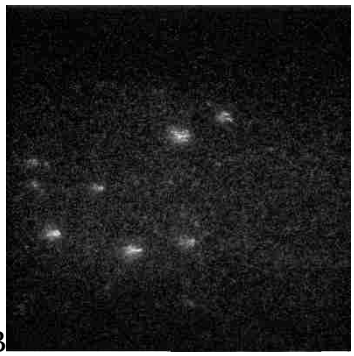 C 

Figure 18. Images of materials imperfections observed in different types of cover glasses. Each was positioned atop the large right angle prism using ultrapure water as a sample. A) Standard glass cover glass. B) Quartz cover glass. C) Dry prism: neither water nor cover glass material.

Interpretation of Data

Dye-labeled lambda-DNA was necessarily imaged as its strong fluorescent signal served to evaluate the performance of the different sample presentation geometries. When a sample presentation geometry was experiencing significant background noise, or if the optical arrangement or positioning were not optimized, a strongly fluorescing standard analyte was necessary. One goal of the single molecule work was to perfect the experimental method so that single fluorescent nanoparticles could successfully be

imaged. For this reason, it was necessary to increase the capabilities beyond DNA imaging, since electron excitation and relaxation in a fluorescent nanoparticle is a single quantum event and each DNA molecule has hundreds of adsorbed dye molecules undergoing quantum events. Despite the fact that fluorescent semiconductor nanocrystals – especially when coated with an appropriate stabilization layer such as CdS in this case – are extraordinarily photostable, their signal is still relatively weak on an individual basis. Dye-labeled immunoglobulins served the purpose of fine-tuning the experimental methods used in single nanoparticle imaging, as they exhibited a considerably weaker fluorescent signal than the DNA. And while they contained more than a single fluorophore each, those fluorophores had different quantum efficiencies and less resistance to photobleaching than the stabilized semiconductor nanocrystals.

The capillary proved successful in the imaging of both single molecules and single fluorescent nanoparticles and did not require the use of additional mirrors or the complicated process of the alignment for a total internally-reflected laser beam, but it nevertheless had limitations. One limitation was that all attempts to create an evanescent field of excitation using a capillary failed. A geometry not presented here, consisting of the combination of a large right angle prism, immersion oil and a square capillary, not only did not yield an evanescent excitation field layer, but did not produce an analyte signal easily discernable above background noise. It is important to note that since the capillary was square, its vertical sides *required* alignment in a directly vertical position. Otherwise, the focused laser deflected to a degree and created massive noise. In such a situation, the fluorescent signal was also deflected from its path to the detector and was not properly collected by the objective lens.

While square capillaries have been used in single molecule detection experiments in the past [16-20], the literature does not report the use of one with a 50 μm inner diameter. In addition, the capillary mount used in these experiments was built by the author and modified so as to best fit the system existing in our lab.

The use of a single, relatively large, right angle prism has been popular in the literature [21-24]. It was incorporated as part of this study so that its results might be compared with other approaches in efficacy. It has largely been used as a means of producing an evanescent field layer for minimal noise excitation of fluorophores. While it has been quite useful in this application, it has a few weaknesses. The shallow depth of an evanescent field layer is both its strength and its weakness. While very little background noise is generated by the field, the excitation zone is very narrow and is limited to those molecules which are or are nearly touching the fused silica surface. Live cells may only have their very outer perimeters imaged. And in order to get the cell surface close enough to the solid-liquid interface where the excitation field layer exists, there must be very little imaging buffer present. Water from this buffer evaporates along the edges of the cover glass rapidly, creating significant currents of buffer leading from the center of the cover glass to the edges and leaves dry and dead cells as it works inward from the sides. Some researchers use a wax compound to seal the edges of the cover glass to prevent evaporation, but this wax is difficult to remove from the delicate optical surface of the prism without causing damage. Any scratches in the prism surface – including those from low quality manufacturing – create significant visible noise and eventually the optic cannot be used. (See Figure 19.)

The flat prism geometry performed well in all aspects of imaging except one. It was too thick to allow phase contrast microscopy on an upright microscope such as the Olympus BX-51. The condenser beneath the microscope stage collided with the bottom of the flat prism, and was still not close enough to be properly focused on the sample. If the flat prism were to be manufactured to the specifications of a microscope slide's thickness, a new problem would arise: the 45 degree edge which admits the laser beam would be too small a target through which to reasonably align the laser beam. For purely fluorescent work, the flat prism work quite well, combining the prism with the microscope in a convenient, efficient form.

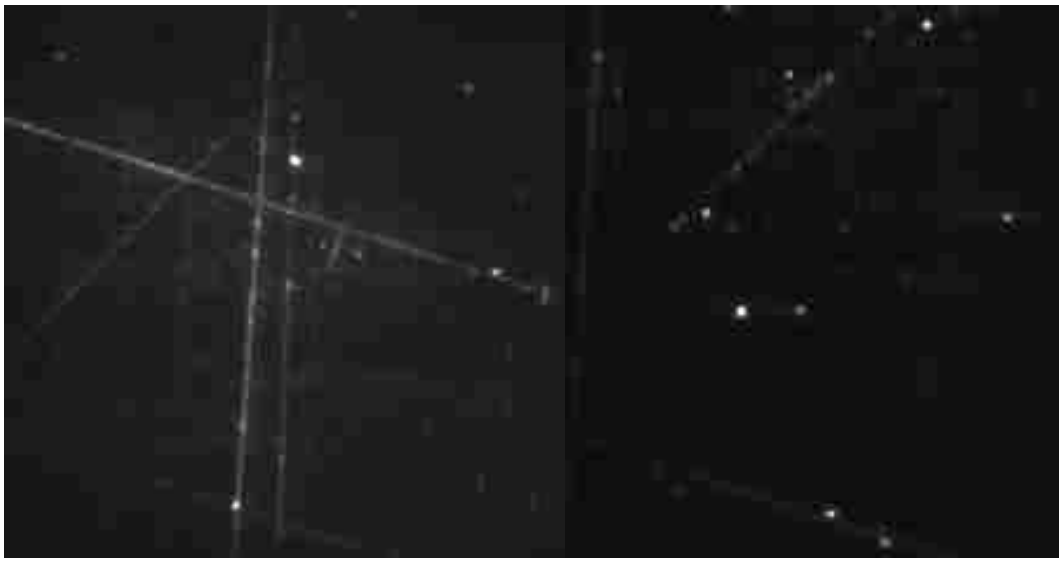

Figure 19. Micro-scratches on the surface of a right angle prism.
Sample is plain PBS.

When building the combination small right angle prism – microscope slide, different slide materials were tested for background noise. This was done because, although fused silica had functioned well for the prisms, it was also quite expensive. Several different types of optical glass were measured. The only nonuniformity that would prohibit direct comparison between the microscope slide materials would be that the available Foturan glass sample was thicker than the other materials. Nevertheless, for our testing purposes, it yielded considerably more noise than any other material and was therefore not chosen for use in the cell imaging optic. As was shown in Table 1, fused silica generated very little noise compared to any of the optical glasses. The optical glass with the least noise, Borofloat 33 glass, still generated background noise levels 3.8 times that of fused silica. The extremely low level of noise observed in the fused silica material is logical. Fused silica is synthetic quartz, and its crystalline structure, as opposed to an amorphous glass, lends itself to high purity. The SiO_2 crystal lattice is more easily created pure than amorphous glass, which can have not only elemental impurities but may also experience inhomogeneity.

When a glass or glasslike material contributes to background noise, the degree of its contribution is directly related to its thickness. Though cover glasses are very thin (approximately 0.17 mm here) they were also tested for noise. Figure 18 shows that imperfections as microscopic bubbles caused serious noise as laser scatter. As very little noise was expected, the emission bandpass filter was removed for these tests. Because the emission filter was not in place, the bubbles were visible for the first time. While standard glass cover glasses continued to be used simply for cost efficiency, this noise test emphasized the importance of material quality and emission optics selection.

Background noise was especially important in the configuration built, as the laser beam internally reflected down the length of the optic. Higher noise may indicate greater material impurities, which may lead to laser scattering and irregularities in sample excitation. Besides impurities, there are also imperfections in optics materials. The quality of a single type of material may vary from lot to lot, and there exist different classes of quality under the same material name as well. This is especially true in the case of crystalline fused silica, which was a problem encountered when purchasing supplies for this experiment. It is sold in different qualities for different applications. All fused silica used in this study was of optics grade.

The modified right angle prism – microscope slide sample presentation platform yielded the most universally acceptable data. The fluorescence images were equal to those acquired using previous sample optic configurations, and it allowed phase contrast images to be collected. Since the microscope slide was only one millimeter thick and the slide was longer than the flat prism, the laser had to internally reflect more times than any other sample configuration as it traveled down the length of the optic to the sample. The resulting slight loss in laser power, however, was easily compensated for by increasing the power setting of the laser. The sample might have been placed nearer to the center of the slide and would have thus reduced the required number of laser reflections, except that the right angle prism would encounter the danger of physically contacting the objective during alignment. The right angle prism was required at the end of the microscope slide because if the laser's angle of incidence was too small, then it would reflect off the surface and not travel inside the microscope slide. If the laser's angle of incidence were great enough to penetrate the slide, then it would also pass through the

bottom and escape the microscope slide without internally reflecting. Only with the right angle prism attached, using optical glue with a similar refractive index, did the microscope slide act as a viable optic for live cell imaging on an upright microscope using an externally-applied total internally reflected laser for excitation.

The behavior of the laser with respect to total internal reflection in the optic, yet direct illumination of the sample was facilitated by differences in refractive index. The refractive index of fused silica is approximately 1.46, of water, approximately 1.33 and of air, approximately 1.0003 [25]. Since the refractive index of fused silica is so different from that of air, the laser undergoes a complete reflection at the interface between the two, as long as the angle is less than 45 degrees. But when the refractive index is much more similar, as is the case with an aqueous solution, the laser passes into the solution to illuminate the sample.

Conclusions

While all sample presentation geometries shown here were successful in their goal of single molecule, single nanoparticle, or single cell imaging, some geometries held clear advantages over others. The 50 μm inner diameter square capillary proved superior to the 75 μm diameter capillary as a result of the depth of the microscope focal plane even though it was a smaller target upon which to focus the laser. The modified microscope slide provided the best live cell imaging results since the right angle prism allowed easy application of the excitation laser, yet the slide thickness facilitated phase contrast microscopy. And, in all cases, fused silica produced the lowest background

signal compared to any of the different glass materials tested. The sample presentation geometries were used in future studies accordingly.

Acknowledgements

Sincere thanks are extended towards Michael Myers and Dean Lenz for their advice, help and the use of their tools and materials in the construction of the various sample presentation devices.

References

1 Ma Y, Shortreed MR, Yeung ES (2000) High-Throughput Single-Molecule Spectroscopy in Free Solution. Analytical Chemistry 72:4640-4645

2 Xu X-H, Yeung ES (1997) Direct measurement of single-molecule diffusion and photodecomposition in free solution. Science (Washington, D. C.) 275:1106-1109

3 Ma Y, Shortreed MR, Li H, Huang W, Yeung ES (2001) Single-molecule immunoassay and DNA diagnosis. Electrophoresis 22:421-426

4 Kang SH, Yeung ES (2002) Dynamics of single-protein molecules at a liquid/solid interface: Implications in capillary electrophoresis and chromatography. Analytical Chemistry 74:6334-6339

5 Yildiz A, Forkey JN, McKinney SA, Ha T, Goldman YE, Selvin PR (2003) Myosin V Walks Hand-Over-Hand: Single Fluorophore Imaging with 1.5-nm Localization. Science (Washington, DC, United States) 300:2061-2065

6 Skoog D, Holler FJ, Nieman T *Principles of Instrumental Analysis*, 5th ed.; Harcourt Brace & Company: Philadelphia, 1998.

7 Hutchins BM, Morgan TT, Ucak-Astarlioglu MG, Williams ME (2007) Optical properties of fluorescent mixtures: Comparing quantum dots to organic dyes. Journal of Chemical Education 84:1301-1303

8 Pelton M, Smith G, Scherer NF, Marcus RA (2007) Evidence for a diffusion-controlled mechanism for fluorescence blinking of colloidal quantum dots. Proceedings of the National Academy of Sciences of the United States of America 104:14249-14254

9 Tang J, Marcus RA (2005) Mechanisms of fluorescence blinking in semiconductor nanocrystal quantum dots. Journal of Chemical Physics 123:054704/054701-054704/054712

10 Wang CH, Chen TT, Tan KW, Chen YF, Cheng CT, Chou PT (2006) Photoluminescence properties of CdTe/CdSe core-shell type-II quantum dots. Journal of Applied Physics 99:123521/123521-123521/123524

11 Gong S, Yao D, Feng X, Jiang H (2006) Quantum size dependent optical nutation in a core-shell CdSe/ZnS quantum dot. Microelectronics Journal 37:904-909

12 Wang Y, Tang Z, Correa-Duarte MA, Pastoriza-Santos I, Giersig M, Kotov NA, Liz-Marzan LM (2004) Mechanism of Strong Luminescence Photoactivation of Citrate-Stabilized Water-Soluble Nanoparticles with CdSe Cores. Journal of Physical Chemistry B 108:15461-15469

13 Barry JP, Muth J, Law S-J, Karger BL, Vouros P (1996) Analysis of modified oligonucleotides by capillary electrophoresis in a polyvinylpyrrolidone matrix coupled with electrospray mass spectrometry. Journal of Chromatography, A 732:159-166

14 Kaniansky D, Masar M, Bielcikova J (1997) Electroosmotic flow suppressing additives for capillary zone electrophoresis in a hydrodynamically closed separation system. Journal of Chromatography, A 792:483-494

15 Srinivasan K, Pohl C, Avdalovic N (1997) Cross-Linked Polymer Coatings for Capillary Electrophoresis and Application to Analysis of Basic Proteins, Acidic Proteins, and Inorganic Ions. Analytical Chemistry 69:2798-2805

16 Zheng J, Yeung ES (2002) Anomalous radial migration of single DNA molecules in capillary electrophoresis. Analytical Chemistry 74:4536-4547

17 Anazawa T, Matsunaga H, Yeung ES (2002) Electrophoretic quantitation of nucleic acids without amplification by single-molecule imaging. Analytical Chemistry 74:5033-5038

18 Zheng J, Yeung ES (2003) Counting single DNA molecules in a capillary with radial focusing. Australian Journal of Chemistry 56:149-153

19 Lee J-y, Li H-W, Yeung ES (2004) Single-molecule spectroscopy for molecular identification in capillary electrophoresis. Journal of Chromatography, A 1053:173-179

20 Li J, Lee J-Y, Yeung ES (2006) Quantitative screening of single copies of human papilloma viral DNA without amplification. Analytical Chemistry 78:6490-6496

21 Funatsu T, Harada Y, Tokunaga M, Saito K, Yanagida T (1995) Imaging of single fluorescent molecules and individual ATP turnovers by single myosin molecules in aqueous solution. Nature (London) 374:555-559

22 Gai H, Li Y, Silber-Li Z, Ma Y, Lin B (2005) Simultaneous measurements of the flow velocities in a microchannel by wide/evanescent field illuminations with particle/single molecules. Lab on a Chip 5:443-449

23 Kang SH, Kim Y-J, Yeung ES (2007) Detection of single-molecule DNA hybridization by using dual-color total internal reflection fluorescence microscopy. Analytical and Bioanalytical Chemistry 387:2663-2671

24 Suzuki Y, Tani T, Sutoh K, Kamimura S (2002) Imaging of the fluorescence spectrum of a single fluorescent molecule by prism-based spectroscopy. FEBS Letters 512:235-239

25 Lide D, Ed. *CRC Handbook of Chemistry and Physics*, 75th ed.: Boca Raton, FL, 1995.

2. Effect of nanoparticles on membrane potential of living A549 cells

Abstract

The safety of nanomaterials has received attention recently in the scientific community. This study chose to investigate the *in vitro* safety of the two commonly produced metal oxide nanopatciles Al_2O_3 and CeO_2. To gain insight into possible cell disruption mechanisms caused by Al_2O_3 and CeO_2 nanoparticles, a real-time single cell imaging system was employed to study the cell membrane potential change by using the membrane potential – sensitive fluorescent probe $DiBAC_4(3)$. Exposure to 13 nm Al_2O_3 nanoparticles resulted in more significant depolarization than 22 nm Al_2O_3 particles. On the other hand, 20 nm CeO_2 particles, though known to be the most toxic, caused less significant depolarization than both the 13 nm and 22 nm Al_2O_3 during the timeframe of this study. Factors such as exposure duration, surface chemistry, and other mechanisms may explain the difference between cytotoxicity data and the live cell imaging results. In addition, 13 nm Al_2O_3 nanoparticles clearly showed more significant depolarization than the 22 nm Al_2O_3 particles. This is the first report that utilizes a real-time single cell imaging system to elucidate depolarization caused by Al_2O_3 nanoparticles.

Keywords

Aluminum oxide (Al_2O_3); nanoparticles; lung cancer cells (A549); depolarization; cell imaging

Introduction

Mammalian cells, in a normal healthy state, maintain a negative potential across the lipid bilayer that forms their outer membrane. Since on both sides of the lipid bilayer there are buffered aqueous solutions, the negative potential inside a cell is established and maintained by the concentration of ions in solution. The individual ionic concentrations are selectively held in place (or changed) largely through the use of ion channels and pumps. These membrane structures are proteins that either actively transport ions from the cytoplasm to the extracellular environment, or alter their tertiary and/or quaternary structures to allow or disallow the passage of cations from the extracellular environment to the cytoplasm (Voet, Voet and Pratt 2002).

The potential across the cell membrane fluctuates in healthy cells, but serious and prolonged disruptions indicate the cell has experienced trauma. Depolarization is a decrease in the absolute value of a cell's membrane potential. Thus, a change in membrane voltage in which the membrane potential becomes less negative is depolarization. In cell function, the potential across the membrane plays an important role by controlling ion fluxes across the cell membrane, signal transduction as well as osmotic balance of the cell. Some previous studies have shown that depolarization appears to be

an early sign of cell damage because of the cytotoxic activity of toxins (Ordonez, Rubinstein and Burnett 1990, Radosevic, et al. 1993).

In this study, bis-(1,3-dibutylbarbituric acid)trimethine oxonol ($DiBAC_4(3)$) was used as the indicator of membrane potential. $DiBAC_4(3)$ is an anionic fluorescent probe whose distribution across the cell membrane depends on membrane potential (Haugland 2005). When depolarization occurs, more dye enters the cells because the inside of cell becomes more positive, and the cellular fluorescence increases. The reason intracellular fluorescence increased with an increase of dye molecules, yet there was relatively little background fluorescence in the imaging buffer, is due to molecular structure. While in solution and unassociated with other molecules, $DiBAC_4(3)$ exhibits almost no fluorescence activity. However, upon association with membrane lipids, it emits an intense fluorescence in the green region (Haugland 2005).

The objective of this study was to gain insight into a possible membrane depolarization toxicity mechanism caused by nanoparticles. To accomplish this, a single molecule and single cell imaging system (SMIS) was used with freshly-suspended nanoparticles in a free solution to monitor the initial interactions between nanoparticles and cells (Gai, et al. 2005, Ma, et al. 2001). The work presented in this section was largely included by the author in a paper published in Toxicological and Environmental Chemistry (Lin, et al. 2008).

Experimental

Nanoparticles

Cerium oxide (CeO_2, 20 nm) and aluminum oxide (Al_2O_3, 13 nm, 22 nm) were synthesized with the room temperature homogeneous nucleation method (Zhou, Anderson and Huebner 2002). Particle size and distribution were analyzed by a Philips EM430 transmission electron microscopy (TEM) (Philips Electron Optics, Eindhoven, Holland). The nanoparticle suspensions in cell imaging buffer (see Chemicals section) for the cell imaging experiments were freshly prepared and diluted to 25 μg/ml, which was equal to the highest dosage in the cytotoxicity study. The concentration was suitable because the cell imaging experiments lasted only one hour and the particles at this concentration did not precipitate over a period of at least 1.5 hours.

Chemicals

Fetal bovine serum (FBS) was purchased from American Type Culture Collection (ATCC) (Manassas, VA, USA). Ham's F-12 medium with L-glutamine, KCl, Na_2HPO_4 and $NaHCO_3$ were purchased from Fisher Scientific (Pittsburg, PA, USA). Penicillin-streptomycin, $FeSO_4$, $MgSO_4$, and $ZnSO_4$ were purchased from Sigma (Saint Louis, MO, USA). The $CaCl_2$, NaCl, and D-glucose were bought from Aldrich (Milwaukee, WI, USA). The fluorescent marker ($DiBAC_4(3)$) was purchased from Molecular Probes (Eugene, OR, USA). Ultrapure DI-water was prepared using a Simplicity 185 system (Millipore, Bedford, MA, USA).

The buffer used for cell imaging experiments contained $CaCl_2$, NaCl, D-glucose, $FeSO_4$, $MgSO_4$, $ZnSO_4$, KCl, Na_2HPO_4, and $NaHCO_3$ at the same concentrations found

in Ham's F-12 culture medium. The buffer was adjusted to pH 7.2 and filtered using a sterile 0.2 μm polyethersulfone filter. The dye $DiBAC_4(3)$ was added to the imaging buffer to a concentration of 1.5 μM immediately before each experiment.

Cell Culture

The human bronchoalveolar carcinoma-derived cell line, A549, was purchased from ATCC (Manassas, VA, USA). This cell line has been widely used in in vitro cytotoxicity studies (Huang, Khor and Lim 2004, Upadhyay, et al. 2003). Cells were maintained in Ham's F-12 medium supplemented with 10% fetal bovine serum and 100 units/ml penicillin, 100 μg/ml streptomycin, and grown at 37 ºC in a 5% CO_2 environment with 100% humidity. Cells to be imaged were cultured on a sterile No. 1.5, 22 mm square glass cover plate.

Single Cell Imaging Assembly

A high purity glass cover plate with cells cultured on one side was used in the study of cell-nanoparticle interactions. The plate was placed on the hypotenuse face of a right-angle fused-silica prism (Melles Griot, Irvine, CA; Prism UVGSFS, A=B=C=2.54 cm) with the cultured cells facing down towards the prism surface. Before each set of experiments, the prism surface was washed with 1.0 M HCl and ultra pure water. The distance between the cell glass plate and prism surface was fixed at 127 μm using two polytetrafluoroethylene (PTFE) film strips under opposite edges of the plate. The plate was strapped firmly in place to prevent it from shifting or floating. Sample suspensions were first introduced into the channel using hydrostatic pressure at one open edge of the

resulting 15 mm channel, while excess sample suspension was removed with a wick at the opposite edge. A 3-ml reservoir coupled to PTFE tubing and a 75 μm inner diameter fused silica capillary delivered a continual flow of sample suspension at a rate of 3.5 μl / min. A continual flow design was used because of the very small volume of sample suspension contained in the 15-mm channel. While cells in the cytotoxicity assessment experiment were exposed to a nanoparticle suspension in the milliliter volume range, the solution volume in the imaging channel was approximately 50 μl. The difference in volumes meant that the cells exposed in the cytotoxicity experiment experienced contact with a "bulk suspension," and therefore a nanoparticle number limited only by the rate of diffusion of the particles within that suspension. However, it was possible that cells exposed in the 15-mm channel would bind nanoparticles, thereby decreasing the number and concentration of nanoparticles in the extracellular environment. The slow yet continual stream of sample suspension assured that the concentration of nanoparticles in the small experiment chamber was constantly refreshed, without introducing a very large flow that might influence experimental results. The experimental setup is shown in Figure 1.

Cell Labeling for Single Cell Imaging

The fluorescent marker $DiBAC_4(3)$ was used to monitor the cells, as its intracellular fluorescence intensity is membrane potential-dependent (Cornfield, et al. 1994, Laskey, et al. 1992). Each glass plate with adhering cultured cells was individually incubated at 37^{o}C in fresh dye-spiked imaging buffer for 30 minutes. The glass plate was then removed, the side with cells was rinsed with 0.5 ml cell imaging buffer, and the

plain glass side was carefully washed with ultra-pure water, dried, and prepared for the oil immersion objective with a drop of immersion oil. The glass was held at such an angle so that the ultra-pure water did not contact the cells.

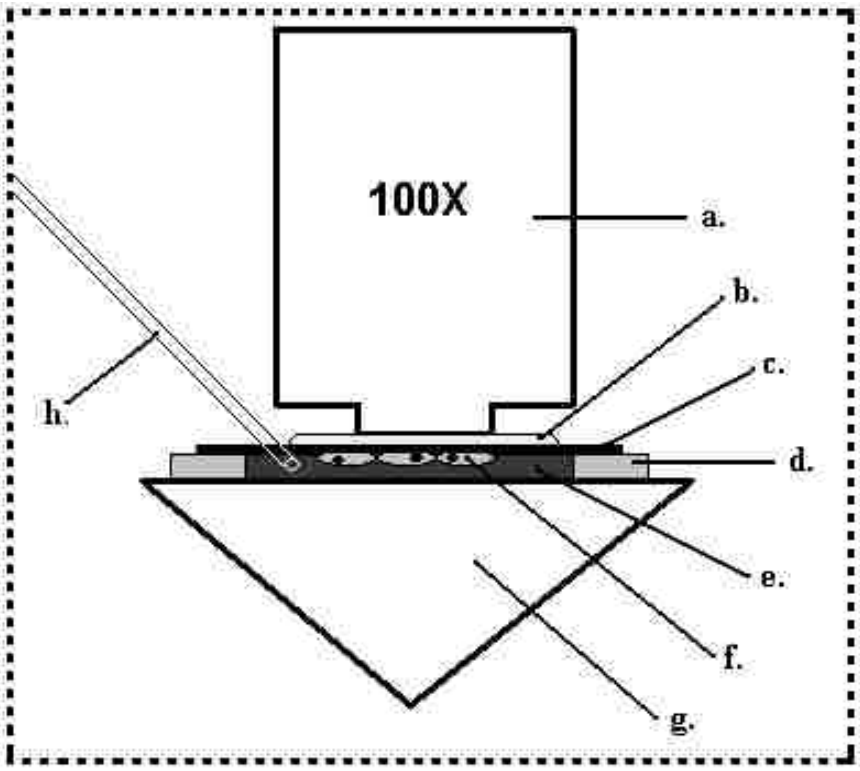

Figure 1. Sample introduction system for single cell imaging.
a.) Objective. b.) Immersion oil. c.) Glass cover plate. d.) PTFE support. e.) Buffer. f.) Cells. g.) Prism. h.) Capillary.

Equipment Setup

The experimental setup for this study represents a minor modification of the data acquisition system used in previous experiments (Gai, et al. 2005, Ma, et al. 2001) and is shown in Figure 2. An Intensified Charge-Coupled Device (ICCD) camera (Princeton

Instruments, Trenton, NJ, USA) was mounted on top of an Olympus upright microscope. The digitization rate of the camera was 5 MHz (12 bits), the controller gain was set at 70 and the camera was kept at -20^{o}C. The camera was operated in the internal synchronization mode and in the frame-transfer mode. The excitation source was an argon ion laser at 488 nm (Spectral Physics, Mountain View, CA , USA). Extraneous light and plasma lines from the laser were eliminated prior to its entry into the observation region with the aid of an equilateral dispersing prism, optical pinholes, and a 488 nm bandpass filter. The laser beam was passed through the right angle prism at an angle of 50 degrees relative to the normal of the glass plate surface. At this angle, the laser light was totally reflected from the top surface of the glass plate to prevent scattered light from reaching the camera. A 488 nm holographic notch filter (Kaiser Optical, Ann Arbor, MI; HNFP) with optical density of >6 and a 514-533 nm bandpass filter (Omega Optical, Brattleboro, VT; No. XF3003) were placed between the objective and the ICCD. An Olympus 100×, 1.3 NA UPlanFl oil microscope objective was used to collect the fluorescence from the labeled cells. Imaging data were collected using Winview/32 software (Princeton Instruments, Trenton, NJ, USA).

The imaging data were analyzed as follows: for each sample, an image data file consisting of 25 video frames was collected every five minutes. Within each imaging file, a single cell was selected. Coordinates for the fluorescence signal at the brightest part of the cell were used to select that region of interest for numerical data analysis. The minimum size of this region of interest was typically 10 x 15 pixels in size. The software calculated the average fluorescence signal in the region of interest. This average was calculated for all 25 frames of each data file, and these 25 averages were averaged in

order to arrive at a single value for the fluorescence intensity of the cell's response in that imaging data file. The same regions of interest were used for all imaging data files of a given sample, to ensure that the same specific region of the same specific cell was measured every five minutes. The process was repeated to collect cell responses from multiple cells within each sample. Imaging data file examination showed that the cell response in the dimmer regions of the cell mirrored the trend in the bright regions, so the bright fluorescence regions were chosen arbitrarily for analysis. In addition, it was determined that within the 25 frames of an imaging data file, no great trend was typically visible in cell response from frame 1 to frame 25. For this reason, the 25 data frames were averaged together. Multiple cells were investigated for all samples, though cell response within each sample was very similar from cell to cell. Since cells in the same sample under the same conditions may yield slightly different levels of fluorescence intensity(Brauner, Hulser and Strasser 1984), the percent change in fluorescence was compared over the course of the experiment. Finally, in order to account for environmental changes such as laser power fluctuations, a sample region containing no cells was analyzed and averaged, and then subtracted from the cellular fluorescence signal prior to the calculation of percent intensity change.

Statistical Analysis

For this experiment, a one-tailed unpaired Student's t-test was used for significance testing, using a p value of 0.05. This determined if the relative fluorescence signal of the cell imaging data were significantly different from control samples.

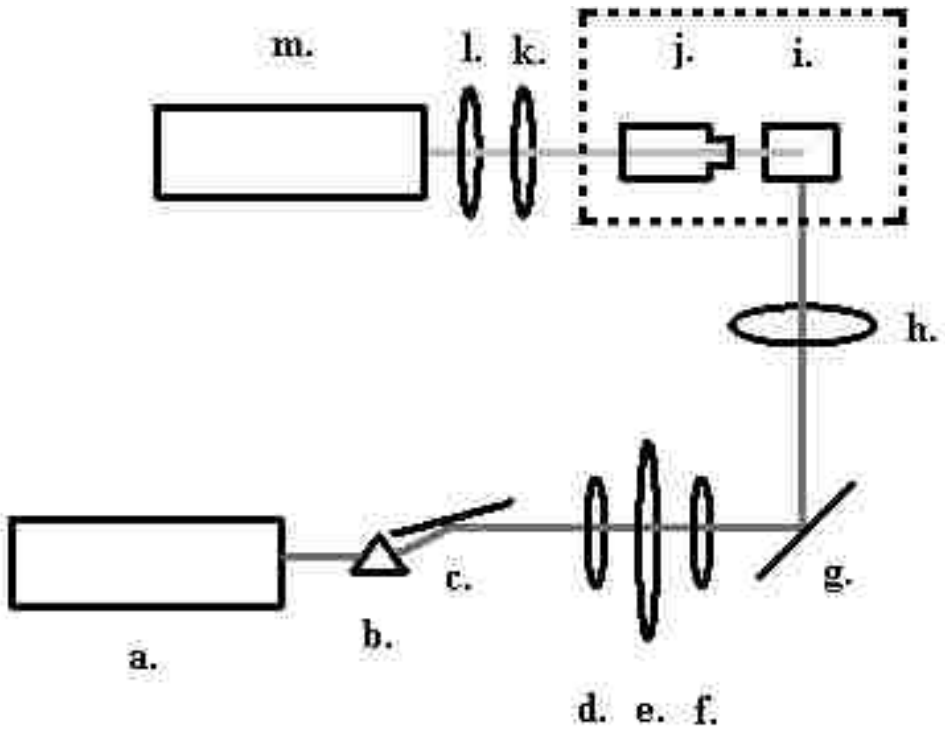

Figure 2. Optical setup for single cell imaging.
a.) Laser. b.) Prism. c.) Mirror. d.) Pinhole. e.) Shutter. f.) Pinhole. g.) Mirror. h.) 488 Bandpass filter. i.) Sample and prism. j.) Microscope objective. k.) 488 notch filter. l.) Emission bandpass filter. m.) Camera.

Results

Single Cell Imaging to Study the Interaction of Nanoparticles with Cells

To investigate the initial interactions of nanoparticles with the cells, a single cell imaging experiment using a SMIS was conducted. The nanoparticles chosen for investigation were 20 nm CeO_2, 13 nm Al_2O_3, and 22 nm Al_2O_3, because they showed greater cytotoxicity in the dose response experiment. Cells were exposed to the same concentration (25 μg/ml) of nanoparticles, while the environment for control cells was

simply imaging buffer. The concentration of nanoparticles chosen was stable for at least 1.5 hours in this particular SMIS system. The cells were first labeled with the fluorescent membrane potential marker $DiBAC_4(3)$. An increase in fluorescence signal is an indication that the potential across the cell membrane is less negative than is the membrane potential in healthy control cells. The fluorescence intensity of the control cells changed little over the course of one hour. In contrast, cells exposed to the various nanoparticles showed a distinct increase in fluorescence intensity over the same period of time (Figure 3). Specifically, at the end of one hour, 13 nm Al_2O_3–treated cells showed an average signal increase of 86%, which was the greatest signal change seen during the experiment. Cells dosed with 22 nm Al_2O_3 showed an average signal increase of 45%, while the 20 nm CeO_2 –treated cells showed the least degree of signal increase, 37%. The control exhibited a relatively stable fluorescence signal, with the maximum average signal change being observed at 14%. Nanoparticle-exposed samples were statistically different from the average control signal at different times. The 22 nm Al_2O_3–treated cells showed a significant difference from the control by 10 minutes ($p < 0.05$, N = 19), yet the percent change in signal leveled out by approximately 30 minutes. The 13 nm Al_2O_3–treated cells showed a significant increase in signal by 15 minutes ($p < 0.05$, N = 12), and 20 nm CeO_2 –treated cells by 55 minutes ($p < 0.05$, N = 7). The signal change in the Al_2O_3–treated cells was visibly evident, and is illustrated in Figure 4. Cell morphology remained generally unchanged throughout the experiment.

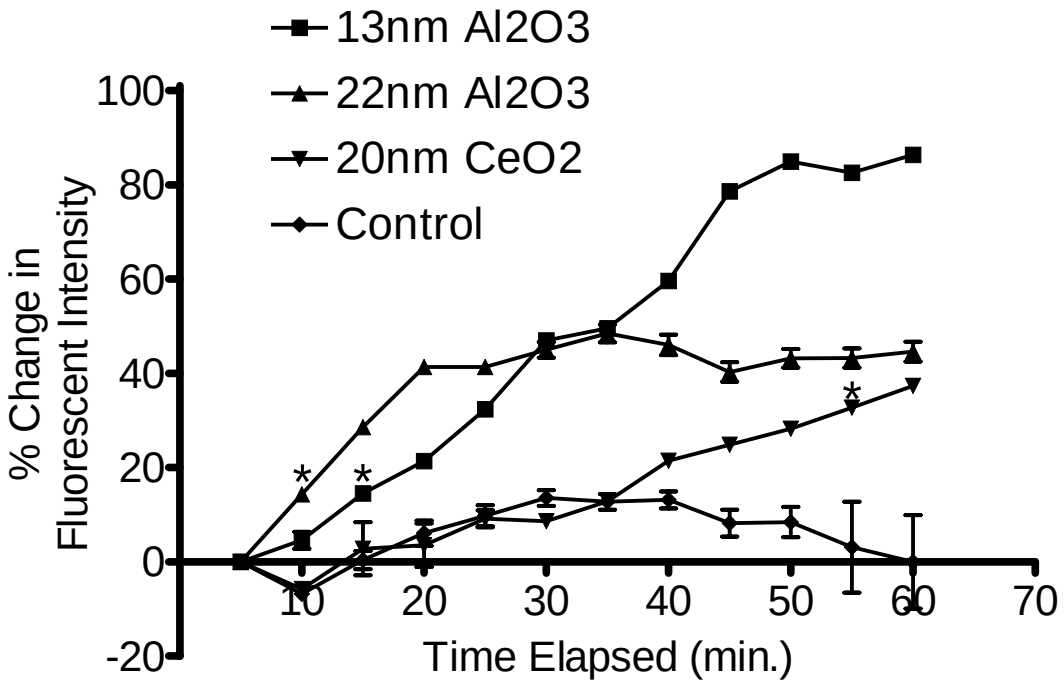

Figure 3. Averaged percent change in cellular fluorescence intensity for control, and after treatment with Al_2O_3 and CeO_2 nanoparticles.
Data were expressed as mean ± coefficient of variation. The coefficient of variation is calculated by multiplying the standard deviation by 100 and dividing by the average. Nanoparticle data with an asterisk [*] above them designate the first point in each respective nanoparticle data series to be significantly different from the controls. This significance for 13 nm Al_2O_3 (N = 12), 22 nm Al_2O_3 (N = 19) and 20 nm CeO_2 (N = 7) was calculated using the student's t test ($p < 0.05$).

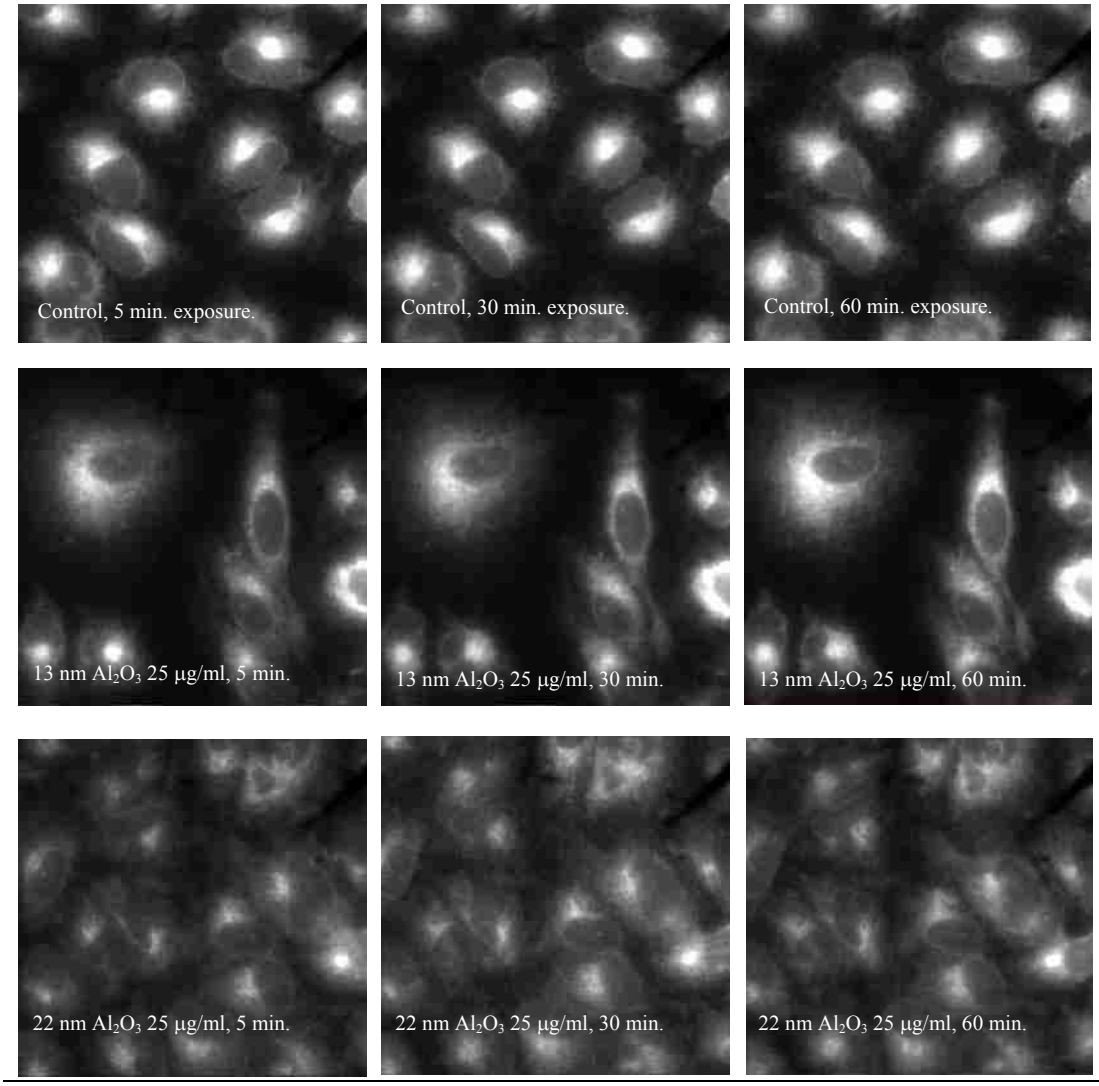

Figure 4. Examples of fluorescence intensity changes after cells were exposed to 13 nm and 22 nm Al_2O_3 nanoparticles.
Images shown here were collected at 5, 30 and 60 minutes. Control images are shown in the first row.

Discussion

To investigate possible initial mechanisms of toxicity, the changes in cell membrane potential were studied by monitoring the fluorescence intensity of the anionic

cell membrane marker $DiBAC_4(3)$. This marker has been widely used for investigating cell membrane behavior while cells are under environmental stress or other conditions (Allen and Kirk 2004, Wolff, Fuks and Chatelain 2003, Xie and Zhuang 2001). When depolarization of the cell membrane occurs, the transmembrane dye equilibrium shifts, causing the dye to migrate inside the cell from the extracellular environment. The reverse is also true; hyperpolarization causes the observed fluorescence signal to decrease.

In this study, the increase in fluorescence signal indicated depolarization of the cell membrane after the cells were exposed to Al_2O_3 and CeO_2 nanoparticles. Such a condition could be caused by a number of pathways including a protein-mediated influx of a specific cation or cations, expulsion of a specific anion or anions, or by physical breaches of the membrane. Under normal conditions, the potential across the cell membrane is maintained by the active transport of cations through the lipid bilayer (Widmaier, Raff and Strang 2004). Since the concentrations of ions such as Cl^-, K^+, Ca^{2+}, and Na^+ within the cell help regulate physiological pathways, a change in the concentration of each can activate a variety of mechanisms within the cell (Becker, Kleinsmith and Hardin 2000). This includes even the triggering of apoptosis, as is the case with Ca^{2+} (Orrenius, Zhivotovsky and Nicotera 2003). Further research is necessary to clarify the exact pathway(s) by which the membrane potential is changed.

Exposure to the nanoparticles tested in the cell imaging experiment caused a distinct increase in the fluorescence intensity of the $DBAC_4(3)$ dye in the cells (Figure 3). Of the three kinds of particles studied, the 13 nm Al_2O_3 nanoparticles appeared to have the greatest influence upon the cells. Moreover, the effect was time-dependent. Oscillation of signal was observed in control cells, but the signal did not increase sharply.

An ANOVA of the control data revealed that the control groups were not significantly different from one another ($p > 0.05$). The 13 nm Al_2O_3 caused the most membrane depolarization during the measured exposure time, followed by 22 nm Al_2O_3. The data from imaging the cell membrane potential change did not agree with the Al_2O_3 nanoparticle cytotoxicity data (Lin, et al. 2008).

Proteins are known to adsorb onto the surfaces of numerous types of nanoparticles, and CeO_2 and Al_2O_3follow this trend (Horie, et al. 2009, Tang, et al. 2006). Since there were no proteins added to the imaging buffer, it is likely that the particle surfaces were mostly free of adsorbed proteins when they first contacted the A549 cells. As a result, proteins on the cell surfaces were in a position to experience direct nanoparticle adsorption. Among the proteins on a cell surface are ion channels, so it is possible that nanoparticle adsorption onto ion channel proteins disrupted the natural ion balance maintained across the membrane through active ion transport. This phenomenon may have had an influence upon the mechanism of toxicity to the cells within the first hour of exposure.

In the cytotoxicity study, the 20 nm CeO_2 showed the greatest cytotoxicity. Why, then, did it cause a lesser degree of disruption of membrane potential in the imaging experiment compared to Al_2O_3? Different factors may contribute to this apparent discrepancy. First, the exposure time during the imaging experiment (60 minutes) was very short compared to the 24-hour exposure in the cytotoxicity experiment. Thus, any changes observed during the imaging experiment represent only the initial effects of nanoparticles upon the cells. Cell environmental conditions limited the length of the imaging study, as neither temperature nor atmospheric gas concentrations could be

regulated. Second, it is reasonable to suspect that the Al_2O_3 particles may exhibit faster kinetics than CeO_2 nanoparticles when moving through the solution and interacting with the cells, due to their lower density. Third, CeO_2 nanoparticles may produce toxicity via mechanisms that do not involve disrupting the membrane potential. For example, previous work done in this research group has shown the cytotoxicity of CeO_2 nanoparticles was related to an oxidative stress mechanism and lipid peroxidation (Lin, et al. 2006). Fourth, since the chemical surfaces of the CeO_2 and Al_2O_3 nanoparticles are different, they may interact with the membrane differently. The metal atoms on the surface of the two kinds of metal oxide nanoparticles are different in their size, charge (and charge density), valence electrons and valence electron orbital arrangements. These several factors may cause the difference in reaction time with the cell membrane, as well as affect the number of nanoparticles interacting with the membrane. The presence of such differentiating factors would eventually cause a difference in the levels of cytotoxicity. These are areas meriting further research.

Conclusion

The real-time imaging study clearly proved that cell membrane depolarization induced by two sizes of Al_2O_3 and CeO_2 nanoparticles may be one of the initial mechanisms of action for nanoparticle cytotoxicity. It is plausible that aluminum oxide and cerium oxide nanoparticles adsorb onto membrane surface proteins and thereby partially inhibit the normal ion movement across the membrane that maintains a correct membrane potential.

Acknowledgements

We thank the Department of Chemistry, the Department of Biological Sciences, and the Environmental Research Center for Emerging Contaminants at the University of Missouri-Rolla for financial support. Thanks also go to Robert S. Aronstam for technical editing.

References

Allen, R.J., K. Kirk. 2004. The membrane potential of the intraerythrocytic malaria parasite Plasmodium falciparum. *Journal of Biological Chemistry* 279, no. 12:11264-11272.

Becker, W.M., L.J. Kleinsmith, J. Hardin In *The World of the Cell,* 4th ed.; Benjamin/Cummings: San Francisco, CA, USA, 2000, pp 212.

Brauner, T., D.F. Hulser, R.J. Strasser. 1984. Comparative measurements of membrane potentials with microelectrodes and voltage-sensitive dyes. *Biochimica et Biophysica acta* 771, no. 2:208-216.

Cornfield, D.N., T. Stevens, I.F. McMurtry, S.H. Abman, D.M. Rodman. 1994. Acute hypoxia causes membrane depolarization and calcium influx in fetal pulmonary artery smooth muscle cells. *American Journal of Physiology* 266, no. 4 Pt 1:L469-475.

Gai, H., Y. Li, Z. Silber-Li, Y. Ma, B. Lin. 2005. Simultaneous measurements of the flow velocities in a microchannel by wide/evanescent field illuminations with particle/single molecules. *Lab Chip* 5, no. 4:443-449.

Haugland, R.P. *The Handbook: A Guide to Fluorescent Probes and Labeling Technologies*, 10th ed. ed.; Invitrogen Corp.: USA, 2005.

Horie, M., K. Nishio, K. Fujita, S. Endoh, A. Miyauchi, Y. Saito, H. Iwahashi, K. Yamamoto, H. Murayama, H. Nakano, N. Nanashima, E. Niki, Y. Yoshida. 2009. Protein Adsorption of Ultrafine Metal Oxide and Its Influence on Cytotoxicity toward Cultured Cells. *Chemical Research in Toxicology* 22, no. 3:543-553.

Huang, M., E. Khor, L.Y. Lim. 2004. Uptake and cytotoxicity of chitosan molecules and nanoparticles: effects of molecular weight and degree of deacetylation. *Pharm Res* 21, no. 2:344-353.

Laskey, R.E., D.J. Adams, M. Cannell, C. van Breemen. 1992. Calcium entry-dependent oscillations of cytoplasmic calcium concentration in cultured endothelial cell monolayers. *Proceedings of the National Academy of Sciences of the United States of America* 89, no. 5:1690-1694.

Lin, W., Y.-w. Huang, X.-D. Zhou, Y. Ma. 2006. Toxicity of Cerium Oxide Nanoparticles in Human Lung Cancer Cells. *International Journal of Toxicology* 25, no. 1-7.

Lin, W., I. Stayton, Y.-w. Huang, X.-D. Zhou, Y. Ma. 2008. Cytotoxicity and cell membrane depolarization induced by aluminum oxide nanoparticles in human lung epithelial cells A549. *Toxicological and Environmental Chemistry* 90, no. 5:983-996.

Ma, Y., M.R. Shortreed, H. Li, W. Huang, E.S. Yeung. 2001. Single-molecule immunoassay and DNA diagnosis. *Electrophoresis* 22, no. 3:421-426.

Ordonez, J.V., H.M. Rubinstein, J.W. Burnett. 1990. Flow cytometric detection of jellyfish venom induced cytotoxicity. *Toxicon* 28, no. 7:863-867.

Orrenius, S., B. Zhivotovsky, P. Nicotera. 2003. Regulation of cell death: the calcium-apoptosis link. *Nature Review. Molecular Cell Biology* 4, no. 7:552-565.

Radosevic, K., T.C. Bakker Schut, M. van Graft, B.G. de Grooth, J. Greve. 1993. A flow cytometric study of the membrane potential of natural killer and K562 cells during the cytotoxic process. *Journal of Immunological Methods* 161, no. 1:119-128.

Tang, D.Q., D.J. Zhang, D.Y. Tang, H. Ai. 2006. Fabrication of magnetic core-shell CoFe2O4/Al2O3 nanoparticles as immobilized metal chelate affinity support for protein adsorption. *Chemistry Letters* 35, no. 11:1238-1239.

Upadhyay, D., V. Panduri, A. Ghio, D.W. Kamp. 2003. Particulate matter induces alveolar epithelial cell DNA damage and apoptosis: role of free radicals and the mitochondria. *Am J Respir Cell Mol Biol.* 29, no. 2:180-187.

Voet, D., J. Voet, C. Pratt *Fundamentals of Biochemistry*, Upgrade Edition ed.; John Wiley & Sons: United States of America, 2002.

Widmaier, E.P., H. Raff, K.T. Strang In *Human Physiology,* 10th ed.; McGraw-Hill: New York, 2004, pp 160.

Wolff, C., B. Fuks, P. Chatelain. 2003. Comparative study of membrane potential-sensitive fluorescent probes and their use in ion channel screening assays. *Journal of Biomolecular Screening* 8, no. 5:533-543.

Xie, Y., Z.X. Zhuang. 2001. Chromium (VI)-induced production of reactive oxygen species, change of plasma membrane potential and dissipation of mitochondria membrane potential in Chinese hamster lung cell cultures. *Biomedical and Environmental Sciences* 14, no. 3:199-206.

Zhou, X.D., H.U. Anderson, W. Huebner. 2002. Room temperature homogenous nucleation synthesis and thermal stability of nanometer CeO_2 single crystals. *Appl. Phys. Lett.* 80, no. 3814-3816.

3. Study of Uptake and Loss of Silica Nanoparticles in Living Human Lung Epithelial Cells at the Single Cell Level

Abstract

The toxicology of nanomaterials is a blooming field of study, yet it is difficult to keep pace with the innovations in new materials and material applications. Those applications are quickly being introduced in research, industrial and consumer settings. Even though the cytotoxicity of many types of nanoparticles has been demonstrated, the behavior of those particles in a biological environment is not yet fully known. This work has investigated cell uptake and loss of silica nanoparticles using human lung carcinoma (A549) cells. We characterized over time protein adsorption on particle surfaces, the internalization of those particles in A549 cells under different specific protein environments, and the loss of particles following the removal of the environmental presence of the particles. Proteins were shown to quickly saturate the particle surface, followed by a competitive process of particle agglomeration protein adsorption. Uptake of particles peaked at 8-10 hours, and it was determined that, in this system, the charge of the protein-coated particles changed the rate of uptake if the charge difference was great enough. Cells internalized particles lacking any adsorbed proteins approximately three times the rate of protein-coated particles with the same charge. Although particles returned to the extracellular environment over time, the process was relatively slow and did not near completion within 24 hours. Finally, analysis at the single cell level afforded observations of particle agglomerates loosely associated with cell membranes when

serum was present in the culture medium, but in the absence of serum, particles adhered to the dish floor and formed smaller agglomerates on cell surfaces. Although data trends were easily distinguished, all samples showed considerable variation from cell to cell.

Keywords

Human lung epithelial cells; Silica nanoparticles; Cell uptake; Single cell imaging

Introduction

The use of nanomaterials and the study their toxicity is not by any means a new idea [1, 2]. However, as a host of new nanomaterials is created each year, it has proven difficult for researchers to conduct sufficient studies of their biological activities and persistence. Not only has the severity of toxicity alone not been fully evaluated for many of these materials, but also the mechanisms by which the materials interact with living organisms.

Silica is generally deemed nontoxic in chemical terms and relatively inert in biological systems. Its nanoparticles (NPs) have been shown to induce oxidative stress, while their micron-sized counterparts did not [3]. This toxicity towards living cells is cell line dependent, and those cells with longer doubling times may be more susceptible to damage [4]. In addition, amorphous silica NPs were found to not be genotoxic in 3T3-L1 fibroblasts [5]. It is well established that proteins adsorb onto silica NPs, and even the stability and orientation of protein structures in that state have been studied [6-9]. One

study in particular found that in the case of RAW 264.7 cells, a macrophage model, membrane receptors for damaged or altered albumin would increase uptake of carbon nanotubes when albumin was adsorbed onto them [10]. Clearly, the proteins and the state of the proteins adsorbed onto NP surfaces have potential in directing NP internalization in living cells. These past studies show the need for a more detailed characterization of the interactions between SiO_2 NPs and living cells, and the role played by adsorbed proteins.

Applications using mesoporous silica NPs would also benefit from further understanding in this area. An example of work with these NPs, Angelos et al. used mesoporous silica NPs for drug delivery, and incorporated activatable molecular nanoimpellers and nanovalves into the structure. This was demonstrated to be useful for delivering hydrophobic anticancer drugs to cancer cells [11]. Other motifs studied for mesoporous silica NPs include spherical and tube-like morphologies and their relative uptake efficiencies based on cell type and particle aggregation [12]. Further work with mesoporous silica NPs showed that a strongly positive surface charge held the potential to inhibit uptake, but that this effect was observed to be cell type-specific [13]. Surface charge studies of solid silica NPs by Xing et al., however, showed a positive charge to aid the uptake of the particles [14]. Sun et al. imaged the real time, live uptake of a single mesoporous silica NP using differential interference contrast microscopy [15]. All these systems would be improved by further knowledge of silica NP and protein behavior.

In this study, we have investigated the uptake of silica NPs in different protein coating environments. Analysis was performed at the single cell level, in order to more fully investigate the diversity of cell response at a resolution that bulk studies cannot

deliver. The significance of this work is due to its characterization of silica NP surfaces when surrounded by proteins such as would be found in an *in vivo* environment, the effect of this surface modification upon cellular uptake, and investigation of cellular recovery following acute exposure to silica NPs. The work is therefore important in gaining insight into the environmental toxicological properties of silica NPs. We chose A549 (human lung carcinoma) cells, to model inhalation exposure, and studied NPs in a largely protein-free environment to better characterize the interactions of "bare" silica NPs with living cells. This cell line is also valid for studying blood-borne NPs, due to the high blood circulation through the respiratory system. Also studied were pre-coated proteins of biological significance, such as hemoglobin, to model NPs absorbed through the gastrointestinal tract, as they would already have adsorbed proteins by the time they were brought to lung cells via the circulatory system in an occurrence of biological exposure.

The fluorescent silica-capped NPs used in this study contained a CdSe@CdS core [16]. There have been a number of other luminescent silica NPs employed for labeling, and as long as there is not leakage from the NP core, they have been shown to be highly compatible for in vitro testing. Examples of these are those encapsulating fluorescent dyes such as fluorescein isothiocyanate (FITC) in silica [17]. FITC-silica coatings for iron oxide NPs [18], and encapsulation of other organic fluorophores for two-photon fluorescence imaging [19], The toxicity of luminescent silica NPs has been studied, both for organic dye-doped silica particles and for semiconductor-core particles. For dye-doped particles (plain, and amino- and phosphorylate-terminated), He et al. found similar

results at concentrations below 0.2 ug/ml [20]. For those analyzed by Jin et al., the particles showed no significant toxicity at concentrations below 0.1 mg/ml [21].

Experimental

Chemicals

Bovine serum albumin (BSA), unfractionated bovine histone, bovine hemoglobin, Folin-Ciocalteu's phenol reagent and copper sulfate were purchased from Sigma (St. Louis, MO). Penicillin-streptomycin, sodium-potassium tartrate, sodium phosphate, sodium chloride and optima-grade nitric acid were purchased from Fisher Scientific (Waltham, MA). Coomassie Plus Protein Assay Reagent was purchased from Pierce (Rockford, IL). Sodium citrate, cadmium perchlorate, dimethylselenourea, thioacetamide, mercaptopropyltrimethoxysilane, sodium silicate, isopropanol and NaOH were purchased from Aldrich (Milwaukee, WI). Fetal bovine serum (FBS) and Ham's F-12 nutrient mixture with L-glutamine but without phenol red were purchased from Midsci (St. Louis, MO).

Aqueous solutions were made using water purified with a Millipore Simplicity 185 water purification system. All pH measurements were performed using an Accumet XL15 meter (Fisher Scientific).

Nanoparticle Synthesis and Characterization

Fluorescent nanoparticles were synthesized using the procedure by Wang et al. [16], except for the following modification(s): after synthesis, the nanoparticle suspension was purified by the addition of 50 ml of isopropanol followed by

centrifugation. This purification procedure was repeated three times. The synthesis procedure produced fluorescent NPs in a stock suspension, which were counted by diluting them in a 1:33 ratio in purified water, sonicating them for 20 minutes and imaging their fluorescence in a single molecule detection system designed as previously described [22]. The system used for this work was modified in the following ways: the uncoated square capillary from Polymicro Technologies (Phoenix, AZ) used had an internal diameter of 50 μm, an Olympus UPlanFl 40X (NA = 0.75) objective was used, on an Olympus BX51 microscope (Tokyo, Japan), and a Uniblitz (Rochester, NY) shutter driver / timer model VMM-T1 was used to control the rate of data acquisition. Unequal elevation of sample vials at either end of the capillary produced a slow flow rate, which was interrupted periodically with pressure-rinsing to introduce fresh NP suspension from the sample vial into the capillary.

The sizes of NPs were characterized by a JEOL 1400 transmission electron microscopy (TEM) instrument. The samples were prepared on 200 mesh carbon-coated Cu grids. The TEM images showed silica-coated particles with a diameter of 13 nm. The fluorescent CdSe@CdS core inside the SiO_2 shell makes the whole nanoparticle visible in single cell imaging.

Plain silica nanoparticles (15 nm) were supplied by Degussa Co. (Parsippany, NJ). Plain silica nanoparticles were only used in the time-dependent protein-particle adsorption experiments.

Spectral Analysis of Fluorescent Nanoparticles

Absorbance measurements were performed using a Beckman DU 640B UV-vis spectrophotometer. Fluorescent nanoparticle fluorescence measurements were performed using a Perkin-Elmer LS-5 fluorescence spectrophotometer. Fluorescent nanoparticles were suspended in ultra pure water for spectral analysis.

Cell Culture and Treatment with NPs

A549 (human lung carcinoma) cells were purchased from ATCC (Manassas, VA). Subculturing was performed using Ham's F-12 medium, with L-glutamine and without phenol red with 1% Penicillin-streptomycin and 10% fetal bovine serum at 37°C with a 5% CO_2 atmosphere and 100% humidity. For imaging experiments, cells were grown on sterile cover glasses, held in a Petri dish. Cells were plated at a density of 1.2×10^5 cells per 9.62 cm^2.

Each cover glass was prepared to image on the microscope by rinsing the bottom with distilled water, and 500 μl of culture medium from the Petri dish was used to rinse the side with adherent cells to ensure no distilled water made contact with the cells. A lint-free cloth was used to dry the cover glass bottom. A quartz microscope slide was prepared with 30 μl of culture media, and the cover glass was placed on the slide and a drop of immersion oil was added prior to imaging.

Alternatively, glass-bottomed Petri dishes (In Vitro Scientific, Sunnyvale, CA) were used for the following experiments: protein-free NP uptake, pre-aggregated NP uptake, and specific protein-adsorption uptake. In this arrangement, cells were plated in a Petri dish and the dish was placed directly on the microscope, with immersion oil. Three-

dimensional images were recorded, followed by micropipette-rinsing the cells with media from the dish, and finally three-dimensional images of the rinsed cells were recorded. For all samples, cells were grown in Petri dishes for 24 hours before being dosed with NPs. In all experiments, NPs were dispersed in the appropriate solution by using a sonication bath for 15 minutes. In addition, all samples were dosed at a concentration of 5.0×10^8 particles/ml cell culture medium, at 2 ml medium per Petri dish, with the exception of the samples comprising the dose-dependent curve. Experiment-specific dosing schemes were as follows: Dose-dependent and simple time-dependent uptake experiments were designed to suspend nanoparticles in complete cell medium and apply to the samples.

Nanoparticle loss over time: Samples were dosed according to the simple time-dependent uptake procedure. At 24 hours of exposure, the medium in the Petri dishes was removed, followed by two rinses of 1 ml fresh, NP-free medium, which was followed by 2 ml of NP-free medium. Samples continued to be incubated, and were measured over time for NP content.

Pre-aggregated NP uptake: After NPs were dispersed at the proper concentration in culture medium, the suspension was allowed to rest at 4 ºC for 12 hours before being warmed, vortexed and applied to the Petri dishes.

Protein-free uptake: Cells were plated in the Petri dishes using complete medium. After 24 hours, the dishes were rinsed twice with 1 ml of FBS-free medium. Nanoparticles were suspended in FBS-free culture medium and applied. Dosing and detection was otherwise unchanged.

Specific protein-adsorption uptake: Cells were dosed with NPs that had a specific protein adsorbed to their surfaces prior to dosing. Based on this paper's study of protein adsorption onto silica NP surfaces, it was determined that a 10% solution of a given protein would be used to pre-coat NPs. Histone, hemoglobin and albumin were accordingly prepared in 10% solutions, into which NPs were dispersed. For the duration of one hour, the suspension was alternatively gently vortexed, sonicated and rested at room temperature. Finally, the pre-coated NPs were dispersed at the correct concentration in complete medium and dosed to the samples.

Cell imaging

Cell images were obtained using an Olympus IX51 inverted microscope equipped with a 1.25 NA UPlanFL 60x oil objective. Fluorophore excitation was achieved using a mercury lamp and bandpass filters selecting excitation wavelengths centered at either 482 nm or 562 nm. Fluorescence emission passed through bandpass filters centered at either 536 nm or 692 nm before they were recorded using a Hamamatsu ORCA 285 digital CCD camera. From each sample dish were recorded two to three fields of view, randomly chosen, and positioned to maximize the number of whole cells visible at a time. Only cells that were entirely within the field of view were analyzed. An average of 20.4 ± 12.5 cells per sample was analyzed. All experiments were performed between two and four times, depending on the reproducibility. Fluorescent images were captured in multiple planes along the z-axis, allowing the cell to be imaged in its entirety while providing greater particle location information. Phase contrast images were also collected at each z-section. Data collection and image analysis were performed using Slidebook 4.2 software

(Intelligent Imaging Innovations, Inc., San Diego, CA). Image analysis was performed by first overlaying the fluorescence and phase contrast images, and all NPs found outside cells were not counted. Fluorescent NP signals were distinguished from cell autofluorescence signals, as autofluorescence appeared in the red region of emission in addition to the green. In contrast, less than 1% of nanoparticles excited by 562 nm light exhibited fluorescence, while they gave strong fluorescent signals in the green region of emission following excitation by 482 nm light. Therefore, co-localized red and green fluorescence indicated the signal was autofluorescence.

Cadmium Determination by ICP-MS

Preparation of samples prior to Cd quantification followed a procedure previously used by our group for the quantification of Zn [23]. Summarized, that method was as follows: digestion vessels were weighed. Cell homogenate (800 µl) and culture media (5 ml) samples were digested in 3 ml of optima-grade nitric acid, refluxing at 90 °C for 4 hours. Then the samples were allowed to evaporate, leaving a volume of approximately 1 ml. Volumes were brought to 10 ml by adding ultra pure water, and masses were recorded again for calculation purposes. Trace-level Cd measurements were performed using a Perkin-Elmer ELAN DRC-e inductively-coupled plasma mass spectrometry (ICP-MS) system (Perkin-Elmer, Wellesley, MA). The most abundant isotope of Cd, ^{114}Cd, was measured in the analysis.

Protein Content Assays

The Bradford Assay [24] was used to determine total protein content of cell samples. This was done to normalize Cd content in the ICP-MS experiment to the number of cells analyzed. Forty µl of BSA standard or sample cell homogenate was added to 1500 µl Coomassie Plus reagent. This was mixed and incubated for 10 minutes at room temperature. Absorbance was measured at 595 nm, also using the Beckman DU 640B spectrophotometer.

The Hartree-Lowry Assay was used to quantify protein adsorption on silica nanoparticles, as it is more sensitive at lower concentrations than the Bradford Assay, and gives a more linear response [25]. Briefly: 500 µl of standard BSA or nanoparticle suspension was mixed with 450 µl of Reagent A (7 mM sodium potassium tartrate, 0.81 M sodium carbonate, dissolved in 0.5 M NaOH) and incubated at 50 °C for 10 minutes. After cooling to room temperature, 50 µl of Reagent B (70 mM sodium potassium tartrate, 40 mM copper sulfate, dissolved in 0.1 M NaOH) was added, mixed, and incubated at room temperature for 10 minutes. Then 1500 µl of Reagent C (Folin-Ciocalteau's phenol reagent diluted with 15 volumes of water) was added and mixed, followed by incubation at 50 °C for 10 minutes. After each was cooled to room temperature, absorbance was measured at 650 nm using the Beckman DU 640B spectrophotometer.

Determination of Protein Adsorption onto SiO_2 NPs over Time

Silica nanoparticles were dispersed in complete cell culture media at a concentration of 15 µg/ml (approximately 5×10^{11} nanoparticles/ml). This concentration

was high enough to allow the samples to fall safely within the range of the protein assay's absorbance calibration curve, yet reasonably low so as to mimic particle behavior at concentrations used in the cell culture studies. Suspensions were mixed, placed in an ultrasonic bath for 20 minutes, and mixed gently again. Nanoparticle dispersions in open vessels were placed in a cell incubator at 37 °C with 100% humidity and 5% CO_2 atmosphere to imitate cell exposure conditions. Samples were incubated at the following lengths of time: 0, 0.5, 1, 2, 4, 8, 16 and 32 hours. At the appropriate times, nanoparticle dispersions were removed from the incubator and centrifuged at 6000 rpm at room temperature for 30 minutes in an Eppendorf Centrifuge 5403. The supernatant liquid was removed. Particles were resuspended in 1500 µl of phosphate buffered saline (PBS). These suspensions were placed in an ultrasonic bath for 30 minutes prior to analysis using the Hartree-Lowry protein content assay.

Determination of Zeta Potential

The zeta potentials of bare silica NPs and of specific protein-coated NPs were determined. For the protein-coated samples, plain silica NPs were alternately swirled, incubated at room temperature, or sonicated in a 10% solution of either BSA, Hb or histone overnight. The plain silica sample was soaked in purified water. All samples were centrifuged at room temperature at 4000 rpm for 30 minutes, after which all but 250 µl of the supernatant was removed. Centrifugation at the same temperature and speed followed for 10 minutes, after which the remainder of the supernatant was removed. Samples were washed with one ml of purified water, centrifuged for 20 minutes, and all supernatant was removed. Immediately before analysis, each sample was individually treated in the

following manner: Three ml of purified water was used to suspend the NPs via vortexing. The suspension was transferred to a glass bottle, and three more ml of purified water was used to briskly rinse the centrifuge tube. This process was repeated four times, after which the suspension in the glass bottle was diluted to 20 ml. The final suspension was mixed and sonicated for 15 minutes, and then analyzed. Analysis was performed using a Malvern Zetasizer Nano-ZS90 (Worcestershire, United Kingdom).

Results and Discussion

Surface Characteristics of Fluorescent Nanoparticles

The application of the SiO_2 shell over the CdS@CdSe nanoparticles was accomplished using a well-established procedure [16, 26-29]. In this case (3-aminopropyl) trimethoxysilane (APS) was adsorbed onto the CdS surface, subsequently displacing the previously adsorbed citrate molecules. Hydrolysis of the surface-boded APS occurs quickly yielding the respective triols. At this stage activated silica in the form of sodium silicate is added to the solution. By maintaining an appropriate pH, the formation of silica nuclei is avoided, yet the silicate groups slowly polymerize at the hydrolyzed APS at the particle's surface. This amaorphous silica layer formed using this approach is a dense and homogenous layer that encapsulates the particle [28, 29]. Nucleation of the silica has been observed to occur after 5 days and so the reaction is quenched prior to this time. The presence of the SiO_2 layer was confirmed via TEM microscopy. At the relevant pH (7.0 – 7.4), the surface of the SiO_2 layer is composed primarily of OH groups bonded to terminal silicon atoms rendering the particle extremely hydrophilic and easily dispersible in aqueous media.

Spectral Analysis of Fluorescent Nanoparticles

Spectral analysis of the fluorescent nanoparticles showed the wavelength range in which they absorbed, which in turn revealed useful fluorescence excitation wavelengths. Figure 1 shows the absorbance curve. Note the shoulder at approximately 488 nm, indicating monodispersity of fluorescent nanoparticle size. The fluorescence emission was measured following excitation at a number of selected wavelengths, and the resulting emission signals are also shown in Figure 1. Emission after all excitation wavelengths was centered at approximately 555 nm, and the signal intensity decreased as the excitation wavelength increased. No fluorescence was detected by the fluorometer using excitation with wavelengths greater than 550 nm. The fluorophore excitation wavelength centered at 482 nm was chosen based on these data, taking into consideration the biological autofluorescence in the UV region, in order to maximize the signal to noise ratio for live *in vitro* fluorescence imaging.

Protein Adsorption onto SiO_2 NPs over Time

It is well known that proteins have a strong tendency to adsorb onto silica surfaces, and silica nanoparticles are no exception [7, 10, 30, 31]. Therefore, in order to correctly interpret NP-cell interactions, it was first necessary to characterize the NP surfaces as they changed in the cell growth media environment over time. Protein adsorption occurred very quickly, reaching a level of approximately 2.5 mg protein / μg SiO_2 NPs by 2 hours (See Figure 2). A downward trend in the mass of adsorbed protein was then observed, until an equilibrium level was reached at 1.7 mg protein / μg SiO_2 NPs after approximately 15 hours.

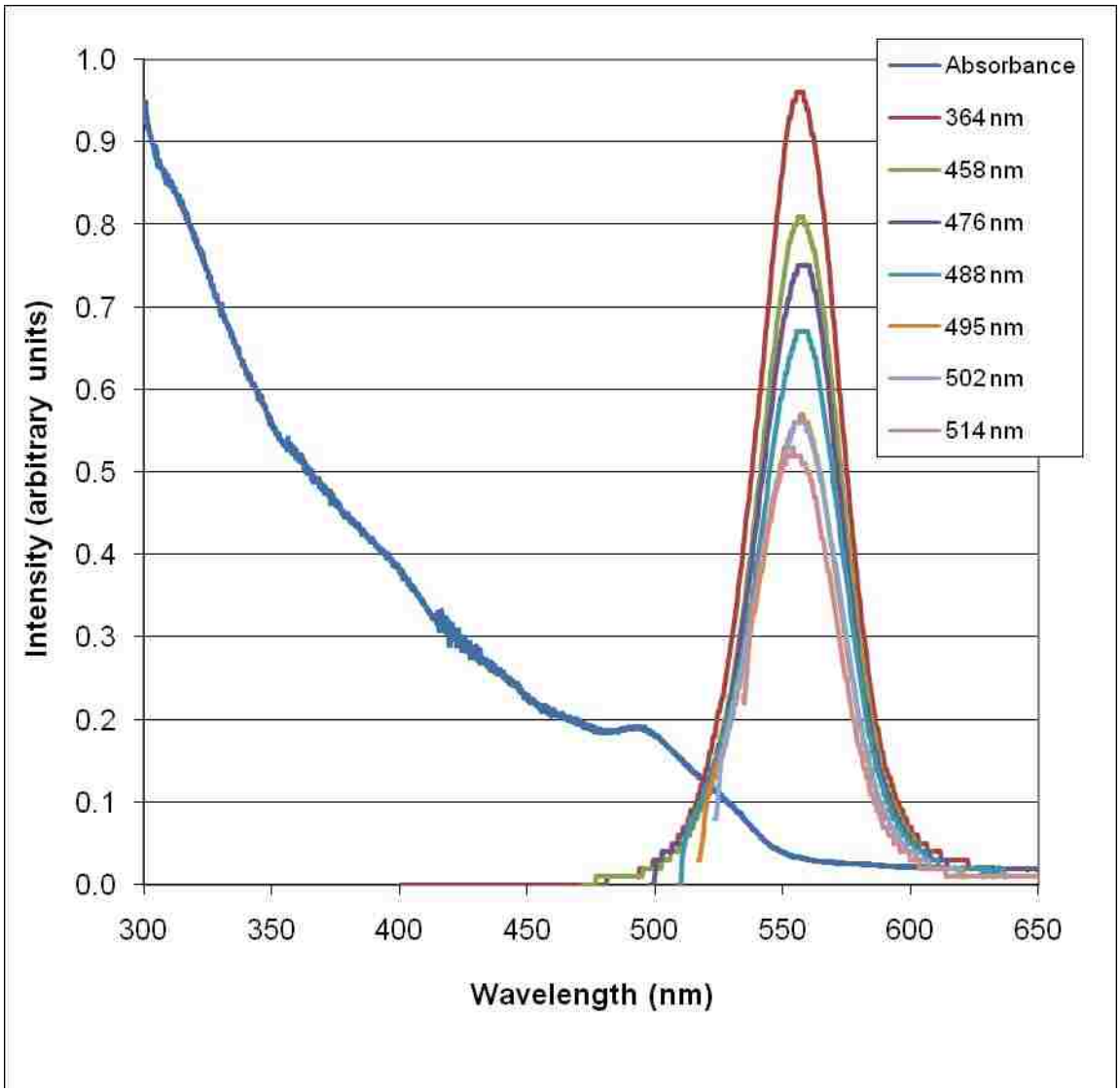

Figure 1. Absorbance curve and fluorescence emission peaks following excitation at noted wavelengths for fluorescent nanoparticles.

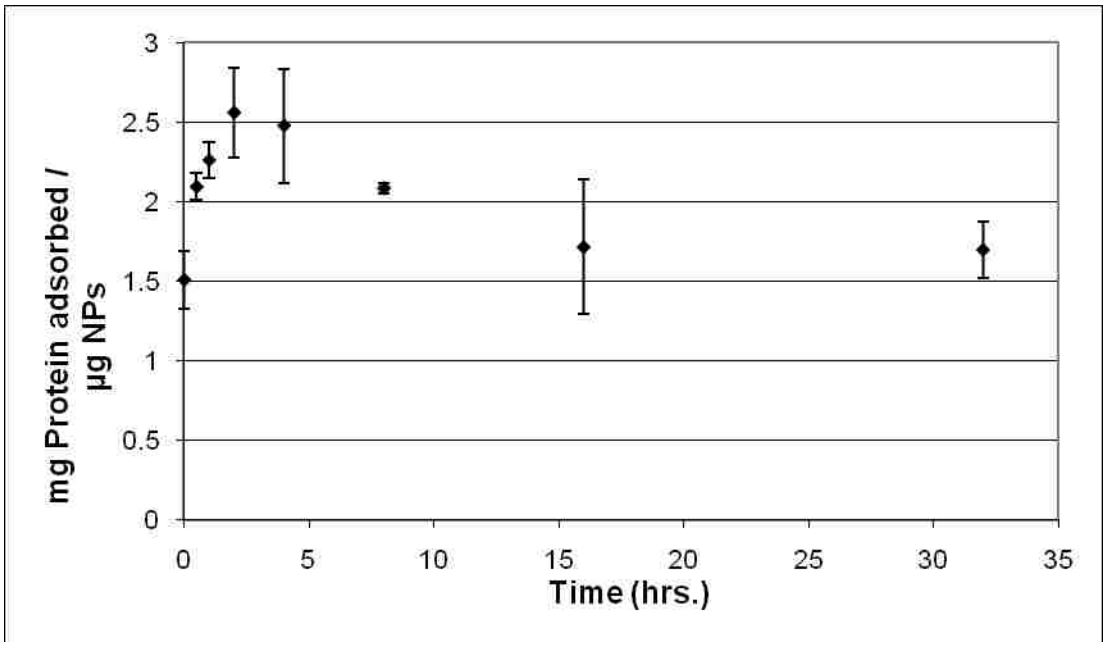

Figure 2. Protein adsorption onto silica nanoparticles over time in complete cell growth medium.

Since protein content was measured using a UV-Vis absorbance method, NPs suspended in water were measured as a control for the light scattered by the suspended solid particles. In addition, since the Hartree-Lowry protein assay quantifies proteins through the binding of tyrosine, tryptophan and cysteine amino acids, (and these amino acids were listed on the nutrient mixture formulation sheet at concentrations of 7.8, 2, and 35 mg/l, respectively) it was necessary to determine the response generated following the adsorption of these molecules. Our study showed that the absorbance signal from these two sources of interference was 9.8 ± 0.4% for water and 13.5 ± 1.5% for the cell nutrient mixture (lacking FBS), relative to the signal generated by NPs incubated in complete cell growth media. So while light scattering by bare NPs and absorbance by lone amino acids

detected by the assay was not negligible, it was an order of magnitude smaller than the light absorbed in the protein assay.

Since the pH of cell growth media changes as it reaches equilibrium with the incubator's 5% CO_2 environment, this was investigated as a possible influence on the surface condition of particles. It was determined that the pH of the complete culture media was initially 7.64, but when equilibrium with the 5% CO_2 atmosphere was achieved, it was 7.30. As this change in pH does not induce a great change in the surface of silica or in the solubility of FBS proteins, this factor likely had little or no effect upon the behavior of protein – nanoparticle interactions.

Dose- dependent Uptake of NPs in Cells

In order to choose the concentration of nanoparticles to use in time-dependent exposure studies, a dose response study was first conducted. The duration of the dose-dependent uptake experiment was 24 hours. Primarily, it was necessary to determine that the concentration chosen would not saturate the mechanism(s) by which the cells internalized NPs. A further consideration was to make sure the NP concentration was low enough to distinguish particles individually after internalization. Based on the curve, a concentration of 5.0×10^8 particles per ml culture media was chosen, as the cell uptake at this concentration was in the linear range of the curve, and uptake was clearly not saturated. (See Figure 3.) For these reasons, this concentration was used for the remainder of the experiments.

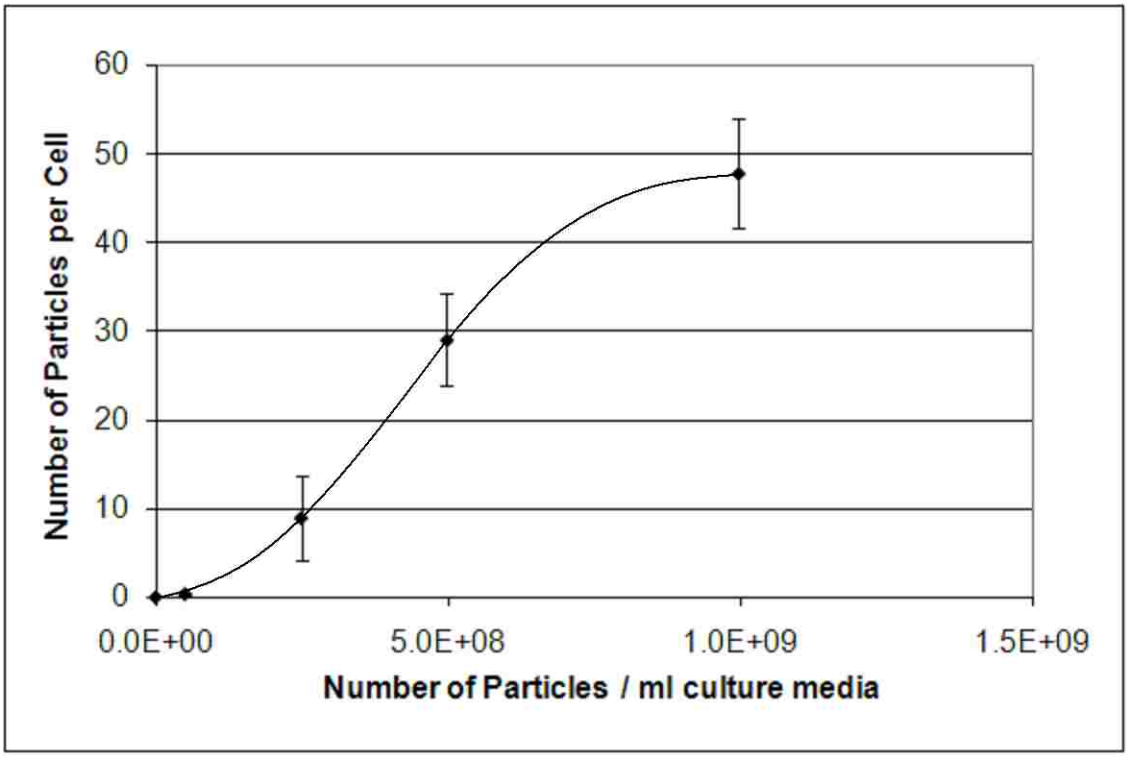

Figure 3. Uptake of fluorescent silica-coated nanoparticles following different doses.

Time-dependent Uptake of NPs in Cells

The rate at which freshly dispersed NPs entered cells in complete culture medium was measured over 24 hours, and served as the standard conditions to which results under different conditions were compared. After approximately 8 to 10 hours, the number of nanoparticles observed in the cells increased very little. The initial linear portion of the curve had a best-fit line of ($y = 4.005\ x + 0.065$) and an R^2 value of 0.89 (See Figure 4).

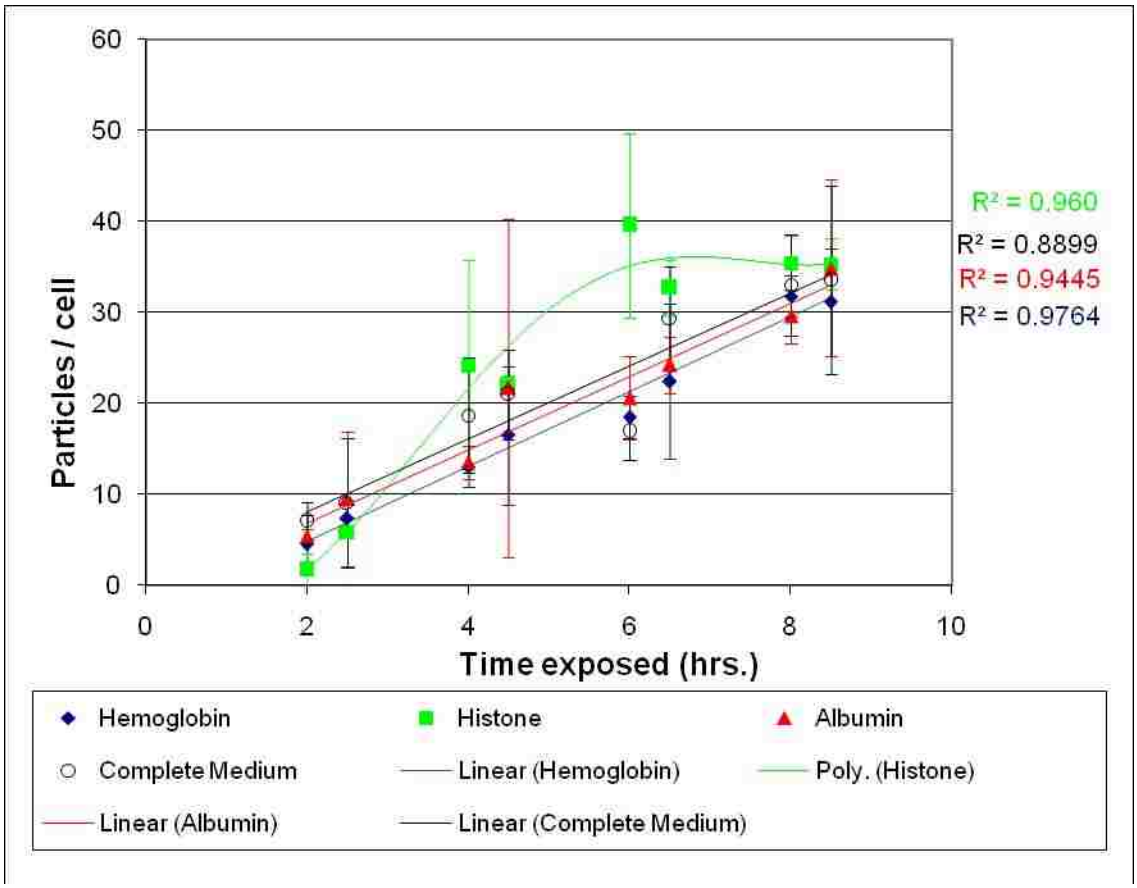

Figure 4. Uptake of fluorescent NPs under different protein environments. Conditions were as follows: specific protein adsorption (albumin, hemoglobin and histone) and adsorption of proteins in complete medium.

The timeframe of zero to 8.5 hours was subsequently chosen for testing NP uptake under differing protein-coating conditions. Examples of fluorescent and phase contrast images are shown in Figure 5. Nanoparticle location within cells appeared to be random, with the two following exceptions: Fluorescence from nanoparticles was not observed inside the nuclei, and quite often there was an accumulation of NPs directly around the nuclear membrane, a trait seen in other more complex silica NP systems [32] (See Fig. 5c). In some cases where it initially appeared that NPs had entered a nucleus, a

closer examination of the data z-series showed that the NPs were located over, not inside, the nucleus. However, other researchers have observed silica NPs enter the nucleus and affect enzyme activity there [33]. The behavior of nanoparticles in live cells has been shown to be cell-line dependent, at least in some cases, though Chen and von Mikecz found that fluorescently-labeled NPs in the 40-70 nm size range entered the nuclei while particles larger or smaller did not.

Internalization of NPs under Different Protein-coating Environments

Proteins with different pIs were adsorbed onto NPs and thoroughly dispersed prior to dosing the cells. Bovine albumin, hemoglobin and histone, with pIs of approximately 4.8, 7.1 and 10.7, respectively, were used [34, 35] (See Figure 4). Bovine albumin was chosen for its acidic pI, and for its ability to act as a secondary control since FBS is largely comprised of BSA. Hemoglobin and histone were chosen for their respective pIs, and the logic behind using proteins found in different biological locations was that in an NP toxic exposure situation, proteins will be scavenged and adsorbed from any place the NPs are present. As will be shown later, NPs may exit a cell where they

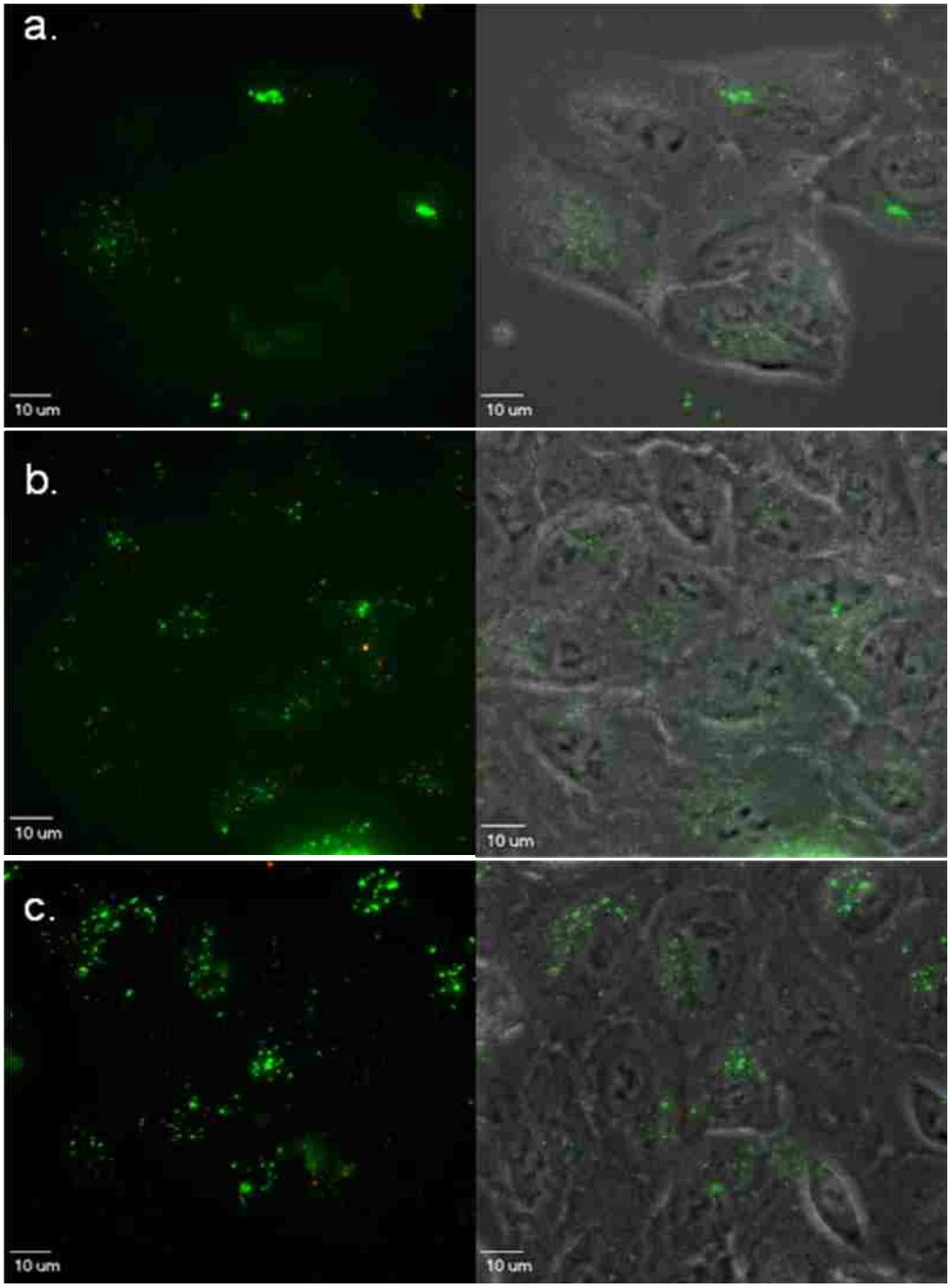

Figure 5. A549 cells in complete medium with internalized fluorescent nanoparticles after specified durations of exposure.
a.) 4 hours of exposure, b.) 8 hours of exposure and c.) 24 hours of exposure. Images on the left show projection images of combined fluorescence signals in the red and green, and images on the right have the phase contrast image superimposed.

have adsorbed proteins, and will then be subsequently eligible to be internalized by other cells. The zeta potentials of bare silica particles and of the particles with their specific proteins adsorbed are listed in Table 1. The uptake curves for NPs pre-coated with albumin and hemoglobin were very similar to the curve for complete medium, with error bars overlapping. It may be noted here that while an uptake trend is clearly evident in the data, the variation from cell to cell was considerable. In the same field of view, cells with relatively few NPs internalized were commonly seen alongside those with many nanoparticles inside (See Fig. 5a). The histone curve displayed the greatest variation of the three specifically – adsorbed proteins, but did not diverge from the general trend until 6 hours of exposure had elapsed, at which time the uptake curve showed a marked decrease in internalization rate. Because of this trend, the histone-coated particle curve appears to reach the "uptake saturation" state earlier than the 10 hours exposure observed in the control curve. In addition, note that FBS is primarily comprised of BSA, and their best fit lines are nearly identical.

Silica NPs have a tendency to form aggregates in aqueous suspension over time. This was observed in all our experiments. In order to examine whether this was the reason for diminished NP internalization after 10 hours of exposure, the standard uptake curve in complete medium was performed, except that the NP suspensions were allowed to form aggregates for 12 hours before being gently vortexed and dosed to the cells. Surprisingly, from 2 to 8.5 hours, the internalization of these pre-aggregated NPs appeared reasonably similar to the uptake of NPs freshly dispersed in complete medium and revealed neither a complete particle uptake blocking mechanism nor showed a great difference in trend (See Figure 6).

Table 1. Zeta potentials of bare and specific protein-coated silica NPs suspended in purified water. The pIs of the proteins, as stated in the literature, are also shown.

	Zeta Potential (mV)	**Standard Deviation (mV)**	**Protein pI**
Plain SiO_2 NPs	**-31.7**	**0.579**	
BSA-coated SiO_2 NPs	**-34.8**	**0.526**	**4.8**
Hb-coated SiO_2 NPs	**-29.6**	**0.399**	**7.1**
Histone-coated SiO_2 NPs	**-18.0**	**0.571**	**10.7**

Xing et al. showed in the past that the lack of FBS in the growth medium enhanced the uptake of NPs. This was also tested, to compare our core-shell NP system with the literature, and to verify that our analysis of relatively few cells at the single cell level would yield trends similar to those produced via bulk analysis methods [17]. Figure 7 displays the complete medium curve again, for reference, and shows the serum-free uptake curve. The serum-free curve is different in three primary ways: there is greater variation between the cells' response at each datum, the trend created by the data is not as linear as for the protein-coated samples, and there are generally more than three times the

number of NPs internalized than any of the protein-coated samples. The data trend from the literature was confirmed using our method, although the difference between protein-coated and serum-free samples was much greater in our study.

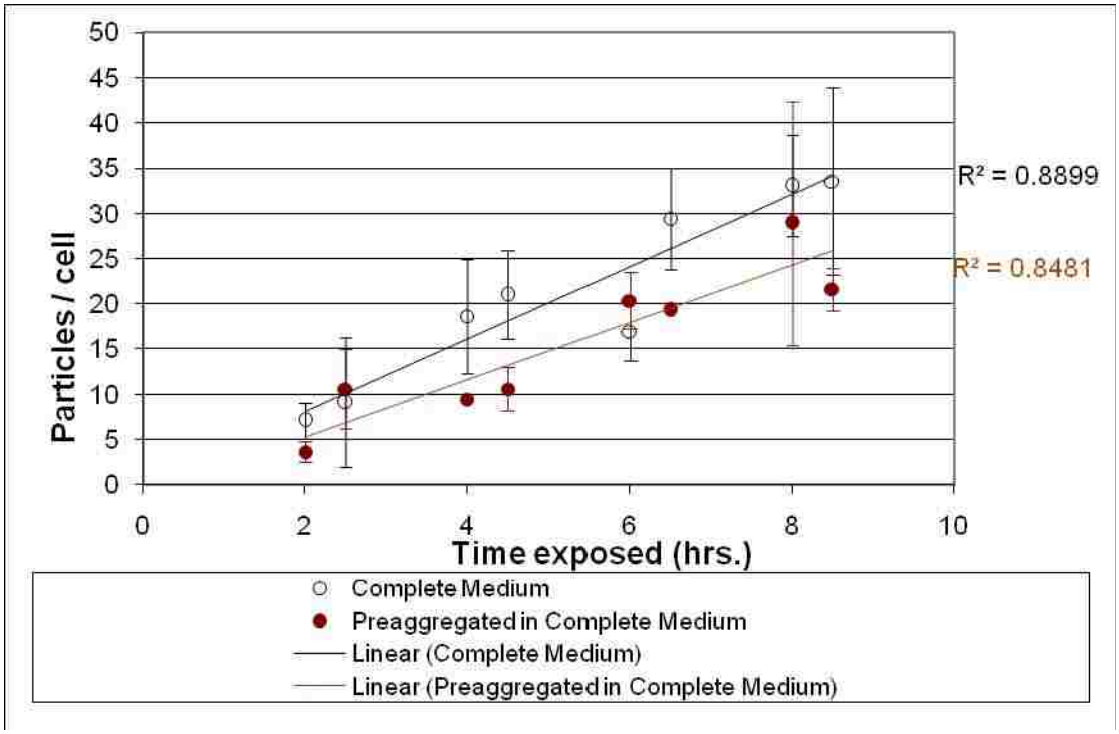

Figure 6. Nanoparticle uptake of pre-agglomerated particles compared to regularly-dispersed particles.

The single-cell analysis method also provided the following observations: Nanoparticle aggregates, identifiable by their intense fluorescence and larger size, were seen in all samples. The serum-free samples exhibited smaller aggregates, which could be found adsorbed onto the dish's cover glass bottom. All samples containing FBS were virtually free of aggregates attached to the glass bottom. Instead, they could be seen loosely associated with cell membranes. Samples were carried in an insulated box approximately 70 meters from the cell incubator to the microscope. Despite the

disturbance of being transported, NP aggregates were still loosely associated with cell membranes. In fact, if aggregates were observed on the glass floor, they typically exhibited motion with any movement of the medium. After an initial image was collected, a micropipette was used to wash away the NP aggregates from cell surfaces to remove detail-concealing fluorescence.

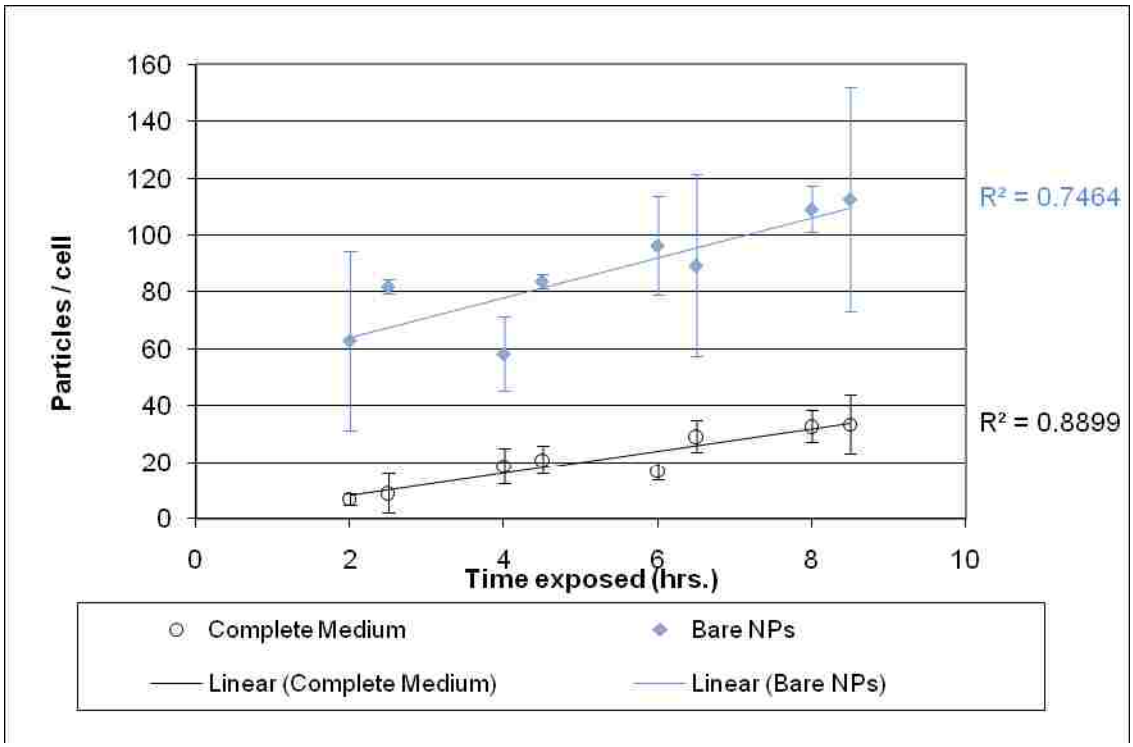

Figure 7. Uptake of nanoparticles in medium lacking serum (protein-free), and in complete medium.

Loss of Internalized NPs over Time

The degree to which nanoparticles exited the cells was also measured, relative to the time elapsed since the environmental presence of NPs was removed. (See Figure 8.)

A rapid decrease was observed until about eight hours had elapsed, and then a very slow and gradual loss of NPs ensued. The trend showed no immediate indication of reaching zero particles per cell.

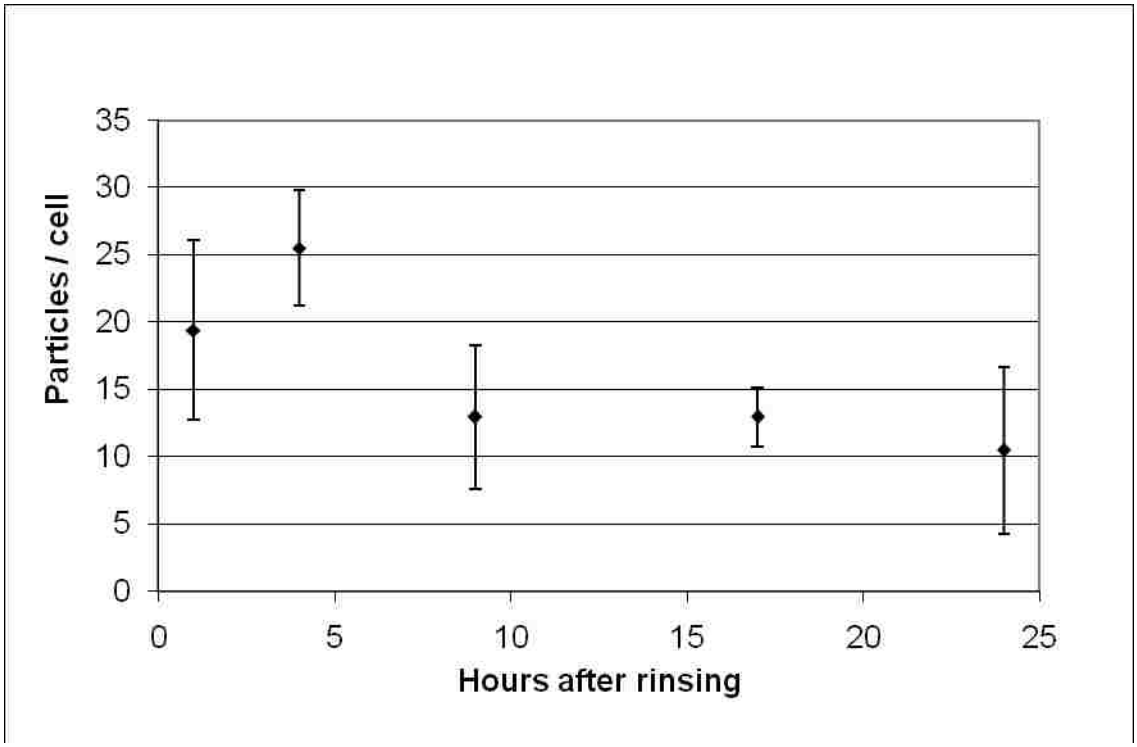

Figure 8. Loss of nanoparticles from cells over time, following the removal of the environmental presence of particles.

Cadmium Determination by Mass Spectrometry

The fluorescent nanoparticles used in these experiments suffer quenched fluorescence if the SiO_2 shell is breached and the semiconductor core is oxidized [16]. Therefore, it was necessary to confirm that the particle loss experiment was not simply a case of the NPs being decomposed or "digested" once they were within a cell. Analysis of both cells and growth media using ICP-MS was performed to measure Cd content. Since Cd is typically present in cell cultures at trace concentrations, the Cd content

measured could be considered as proportional to the number of nanoparticles present. Controls confirmed this. In addition, the Cd content values from cell samples were compared to the nanoparticle content of cells from fluorescence images, to confirm that the Cd measured via ICP-MS was not from NPs whose shells had been compromised. Fluorescent image analysis showed that 46.5% of the NPs present at 24 hours of exposure had exited the cells after 24 hours in a NP-free environment. The ICP-MS data showed that, under the same conditions, 44.2% of the Cd no longer remained in the cells, showing good agreement between the experiments. In addition, the growth media used to incubate cells during the NP loss experiment contained Cd at a concentration three orders of magnitude greater than control, yet two orders of magnitude less than the media intentionally spiked with nanoparticles at the dose concentration (See Table 2). The analysis of growth media during the particle loss experiment was also important, as it confirmed that particles were indeed transferring from the cytoplasm to the exterior environment, and that the decrease of NPs observed per cell over time was not simply due to dispersion of internalized NPs through natural cell division.

Interpretation of Data

Complete cell medium was chosen as the standard condition under which to run this experiment because our goal was to investigate factors influencing mechanisms of silica NP uptake. While quality work has been done in the past on similar systems, cell growth media used to suspend NPs for nearly all tests lacked FBS [17]. Since proteins are abundant in living organisms and would be present in a NP exposure scenario, it was decided to include the serum supplement in all but one experiment. The dose response

and simple uptake experiments mirrored dose and simple time-dependent uptake results as found throughout the literature [17].

Table 2. Analysis of Cd in cells and growth medium using ICP-MS.
Cell sample results reported as mass of Cd normalized to mass of cell protein (μg Cd / mg protein), and growth media results reported as μg Cd measured per ml of medium.

	Average	**±**
NP uptake sample cells	**1.856**	**0.266**
NP loss sample cells	**1.036**	**0.048**
Control cells	**1.796×10^{-4}**	**5.463×10^{-5}**
NP uptake media	**2.739**	**0.056**
NP loss media	**4.903×10^{-2}**	**4.381×10^{-3}**
Control media	**5.470×10^{-5}**	**3.046×10^{-6}**

The curve in Figure 2 showing protein adsorption over time illustrates the importance of this phenomenon in the process of NP internalization. Adsorption begins immediately upon NP exposure to proteins. It is logical that proteins should coat the surfaces of NPs before NP agglomeration occurs, as there are orders of magnitude more

proteins in solution than there are NPs in suspension and therefore a much greater chance of protein-NP collisions through Brownian motion. Also, since silica NPs remain attracted to one another even in a protein-containing medium (see Figure 9b), there appears to be a competition between the adsorption of proteins on the silica NP surfaces and the attraction between those silica surfaces to each other. The result is what appears to be the aggregation of NPs over time, leading to the exclusion of some adsorbed proteins as NPs associate with one another. The NP agglomeration process took between 10 and 15 hours to fully reach equilibrium in Figure 2, yet the uptake curves of the various adsorbed proteins appear not to be greatly affected by the agglomeration taking place in the NP suspension. (See Figures 4 and 6.)

The literature reports that a difference in surface charge on silica NPs will change the rate of internalization in cells [14]. It was therefore investigated whether adsorbed proteins of acidic, neutral, and basic pI would have any effect upon particle internalization, or if simply the cells' recognition of a protein coating would direct NP uptake behavior. The zeta potentials of all specific protein-coated NPs were negative, with histone-coated NPs being the least negative of all (See Table 1). The time-dependent uptake experiment which lasted for 24 hours exhibited a curve which was linear for approximately 9 hours, at which time the slope decreased sharply and leveled off (data not shown). The two to 8.5 hours timeframe was chosen for studying the various factors affecting uptake, since the uptake curve under standard in vitro conditions was linear and unsaturated when the 5.0×10^8 particles/ml concentration was used. The mechanism(s) of uptake for all curves did not appear to be saturated (shown in Figures 4 and 6), as they had overlapping error bars and linear curves, excluding histone after 6 hours. Histone-

coated NPs, with the least negative zeta potential, exhibited the fastest uptake *of the protein-coated* NPs. This trend correlates with that from the literature [14]. The y-intercepts of the linear curves in Figures 4 and 6 have positive nonzero values, which show that NP uptake in under two hours takes place at a faster rate than it does during the 2 - 8.5 hour timeframe of the data. The implication of these data is that as there is rapid realization of a full protein coating on NPs, and when a protein-coated silica NP is internalized by A549 cells, it is recognized as a mass of proteins, where protein type is largely unimportant as long as the overall charge is similar. The silica particle itself is not recognized as such by the living cell since it is concealed behind a cluster of proteins, and the identities of the adsorbed proteins do not necessarily drive uptake. The silica particle itself may not make contact with the cell's membrane molecules, etc., until such time as the adsorbed proteins are removed or released under favorable conditions, possibly once the particle is within a cell. An exception to this condition would be receptor recognition of specific adsorbed proteins, mediating uptake such as occurs with a BSA scavenger receptor [10].

If recognition of the presence of proteins (as opposed to the absence of proteins) governed NP uptake in human lung cancer cells, of interest would be the influence of agglomerate size. It is understood that non-functionalized SiO_2 nanoparticles have a tendency to form aggregates over time when in an aqueous suspension [3]. The pre-aggregated particle experiment showed that, within the experimental timeframe, particles having been pre-coated with proteins and pre-aggregated to an equilibrium size produced an uptake curve with standard deviation bars still overlapping those of the other protein-adsorbed uptake curves except histone. The pre-aggregation uptake curve was decidedly

the lower than all other protein-coated particle uptake curves (See Figures 4 and 6), but failed to reveal a complete blocking of uptake mechanisms. This phenomenon is of particular interest in the field of environmental toxicity studies, as NPs released into the environment will be completely in an 'equilibrium' state with their surroundings. Therefore, we have shown that interactions between silica NPs with one another and with proteins in their environment does not eliminate their ability to be internalized. It should also be remembered that analysis in this study was performed at the single cell level, the result being greater detail in cell-to-cell observations, but a much smaller cell population measured. Greater standard deviation bars resulted, which in turn could possibly blur the edges between the trends of the various curves. Yet even allowing for the limitations of single cell analysis, the following observation remains unexplained: If agglomeration caused NPs to cease entering cells and created a relatively flat uptake curve after many hours (such as is seen in the histone uptake curve after six hours in Fig. 4), why did the pre-agglomeration experiment yield an uptake curve not unlike the sonicated and dispersed NP uptake curves?

The answer to this question can be found in the results of the particle loss experiment. Most toxicological studies of nanomaterials have focused on the uptake of nanomaterials. In this study, we have shown that NPs are indeed released to the extracellular environment. When fluorescence imaging data showed a loss of NPs over time following the removal of environmental NPs, it was necessary to eliminate the possibility that NPs were being "digested" by the cells and the fluorescence thereby optically quenched from inside the cells. Table 2 illustrates the loss of Cd in cells over time. Cadmium presented a convenient species that could be measured at trace levels,

indicating the presence of the fluorescent NPs. It simultaneously shows how, though nearly two orders of magnitude smaller than the dosing concentration, the particle loss sample media contained a three orders of magnitude greater Cd concentration than the control. These results confirmed the phenomenon of NP release to the extra cellular environment. The process appears to be slower and incomplete compared to NP internalization, but nevertheless still takes place (See Fig. 8). This is no surprise, since the equivalent of the entire plasma membrane may fully cycle through the endocytosis and exocytosis processes over the course of two hours or less [36]. The rate at which NPs were released from cells was greatest when the number of NPs within the cells was greatest. Therefore, in addition to agglomerates slowing slightly the entry of NPs to cells, the release of NPs from cells may also contribute to the apparent reduced rate of NP internalization over time, as was seen in the histone-coated NP uptake curve. In other words, after approximately ten hours, NP aggregation slows uptake at a similar time the cell is releasing NPs at the greatest rate. These two factors could easily contribute to the "saturation" stage of a prolonged uptake curve.

Analysis at the single cell level yielded some useful observations. For example, it was noted earlier that large NP aggregates could be seen loosely associated with the plasma membrane, but not generally scattered about the floor of the dish (See Figure 9). Too large for endocytosis in their entirety, the NP aggregates appeared to be attracted to membrane molecules by weak intermolecular forces. As parts of the aggregates separated from the bulk portion, they might then be small enough for internalization. On a small number of occasions, even a strong rinsing with medium would not wash away an associated aggregate. In order to test the strength of the NP agglomerate – cell

interactions in these situations, the rinse treatment was increased enough to detach a cell from the glass substrate on occasion (following the standard image collection sequence). It is therefore possible that some aggregates are either bound to membrane molecules, or have even become slightly inserted into the membrane itself by way of an adsorbed protein tether. It is also possible that some proteins had desorbed from the NP surfaces, allowing the NPs to directly adsorb onto membrane surface proteins. Implications of this phenomenon are that in NP exposure, be it in the gastrointestinal tract, blood or through the skin, pre-agglomeration and protein adsorption may slow but not eliminate uptake of silica NPs.

Single cell imaging also provided useful information on cell uptake of nanoparticles in the absence of FBS. We have determined that the factors driving NP uptake in a protein-rich environment clearly do not dominate uptake of the same particles in a protein-free environment. Note that in Table 1, protein-free NPs have a zeta potential value between the Hb- and BSA-coated particles. Figure 7 then shows that, after a noticeably rapid uptake of protein-free NPs during the first two hours of exposure, the linear curve of these NPs is generally three times the magnitude of the complete medium sample. Key here is the fact that the silica NPs can make uninhibited direct contact with the cells' membrane molecules. As noted before, the significantly higher number of internalized particles in a protein-free environment, despite the loss of numerous NP and NP aggregates to adsorption on the floor of the Petri dish, suggests a very different mechanism of internalization than for the protein-coated moieties (See Fig. 10). Particle diffusion would be faster in protein-free medium since dissolved proteins increase the viscosity, so the medium directly surrounding cells would be replenished with NPs from

the bulk suspension faster as they were internalized. Also, it should be noted that since all cells were cultured in complete medium, the floor of each dish was coated in adsorbed FBS proteins even though the dish was rinsed with FBS-free medium. Therefore, NPs

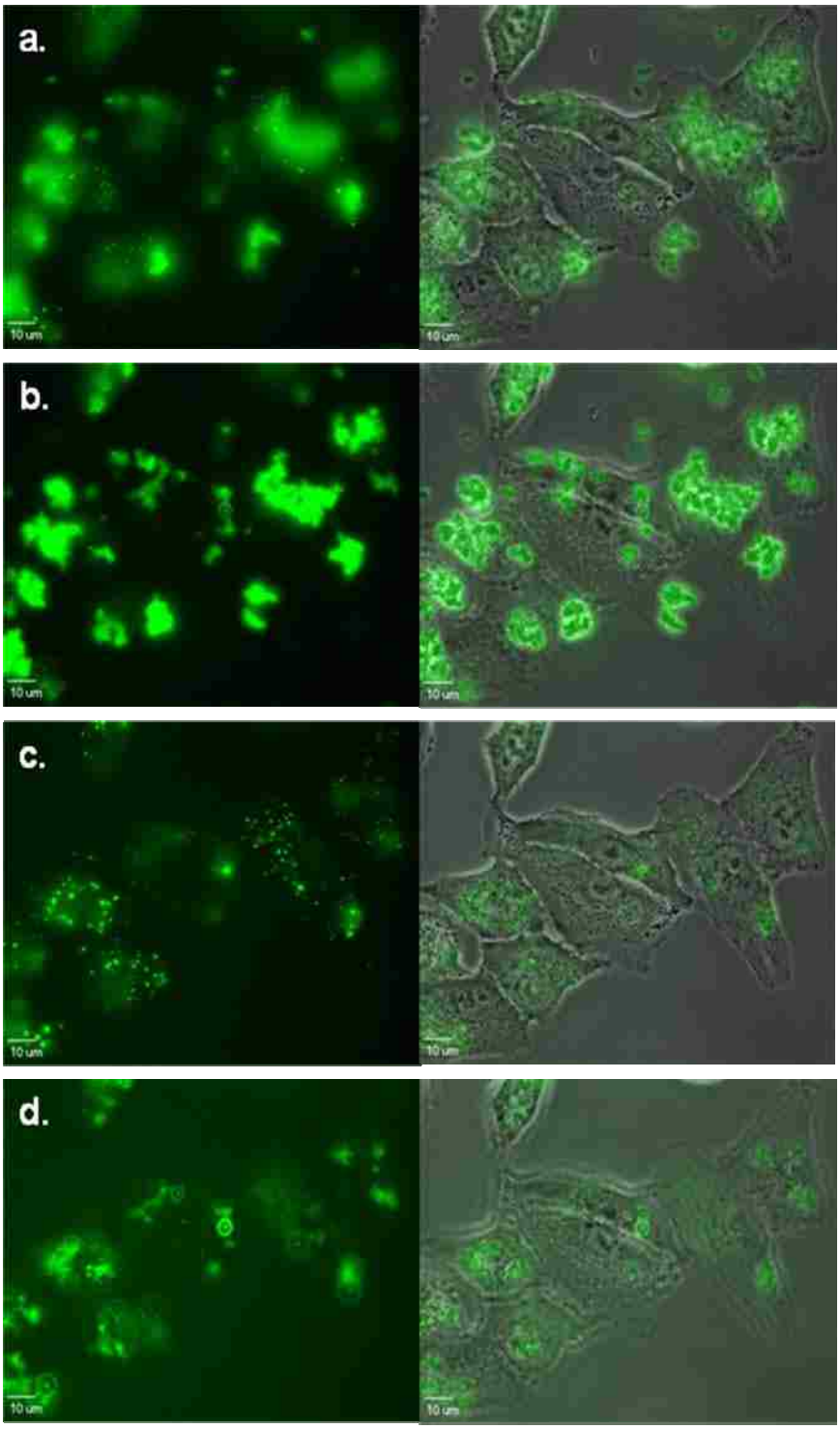

Figure 9. Cell uptake of NPs in complete medium, showing NP agglomerates loosely associated with cell membrane surfaces prior to rinsing, and the disappearance of NPs after rinsing.
Images recorded in a.) the z = 0 plane and b.) the z = 6 plane. Post-rinse images show most large NP agglomerates washed away in c.) the z = 0 plane and d.) the z = 6 plane.
suspended in the serum-free medium adsorbed either onto the glass floor's attached proteins, or onto the glass floor itself. In the experiments where the NPs were coated with adsorbed proteins, there was little to no NP adsorption onto the glass floor because both were already coated in proteins. This offers at least one explanation for the greatly increased NP uptake by cells not surrounded by FBS-containing medium: Silica nanoparticles, not being pre-coated with proteins, quickly adsorb onto proteins incorporated in the cell membrane. Their subsequent internalization may simply be mediated by the rapid continual process of the lipid bilayer use in endocytosis and exocytosis, or the recycling of damaged or altered membrane protein structures, or other processes. It is useful to recall the high rate at which the membrane's lipid bilayer is cycled through the endocytosis and exocytosis processes: commonly less than two hours [36]. In a past study, it has been found that silica NPs coated with a nonionic surfactant had dramatically fewer proteins adsorbed to their surfaces, and the resulting toxicity was greatly diminished [10]. While the surfactant blocked much of the protein adsorption, it also may have blocked a primary mechanism by which the NPs were internalized since the particles would not have adsorbed onto membrane proteins either. The protein-free experiment provides a model for a NP exposure situation where conditions would lead to inhaled silica NPs.

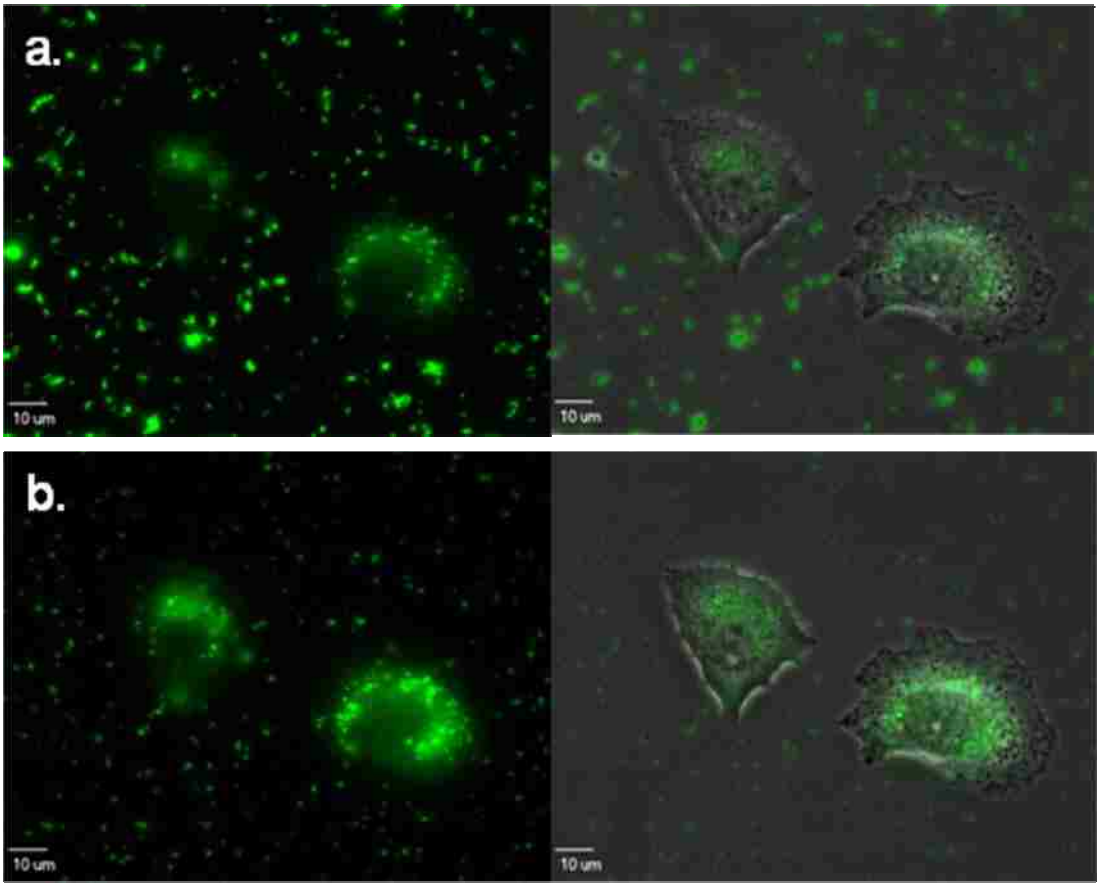

Figure 10. Serum-free uptake showing nanoparticle aggregates adsorbed onto glass plate surface.
a.) pre-rinse and b.) post-rinse. All images are the z = 0 plane of the image series. The images to the left show fluorescence only; the images to the right are fluorescence combined with phase contrast.

Conclusions

In summary, situations of consumer exposure to silica NPs will often give opportunity for both protein adsorption and NP aggregation, whether the route of exposure is the gastrointestinal tract, lungs, or skin. Since pre-aggregation of NPs did not eliminate cellular uptake or alter the location of internalized particles, the risk of

environmental exposure to silica NPs should be carefully explored in addition to freshly-dispersed suspensions. Also, as the pI of the adsorbed proteins did not result in a noticeable change in the rate of uptake except for histone after six hours, these results may apply to all localized environments in the body regardless of the type of protein, unless there is special receptor recognition. Particle charge was confirmed to play a role in uptake, though its effect in our study was minimal compared to the presence versus the absence of adsorbed proteins. Finally, our study indicates that, after acute silica NP exposure, there may be a mechanism or mechanisms by which the NPs can be eliminated at the cellular level. However, for the duration of our experiment, particle elimination did not near completion. As a result, toxicity studies and exposure regulations [37] should consider this parameter for a proper understanding of silica NP safety. The results of these experiments warrant further investigation, for example, the mechanism(s) by which NPs exit the cells. Also of interests are the causes behind the variability between cells and the number of particles internalized within a given period of time.

Acknowledgements

The authors want to acknowledge financial support from Environmental Research Center and the Chemistry Department at Missouri University of Science and Technology. We would like to express our thanks to Honglan Shi for her help with the ICP-MS analysis, Dr. Demin Wang for his help with the zeta potential determination and Xiaoliang Cheng for the translation of a literature article.

References

1 Giddings JC, Piovella F, Ricetti M, Jarvis A, Peake IR, Bloom AL (1980) Characterization of procoagulant activity produced by cultures of human monocytes and lymphocytes separated in colloidal silica-polyvinylpyrrolidone gradients. Clin. Lab. Haematol. 2:121-128

2 Matsuno K, Schaffner T, Gerber HA, Ruchti C, Hess MW, Cottier H (1983) Uptake by enterocytes and subsequent translocation to internal organs, eg, the thymus, of Percoll microspheres administered per os to suckling mice. J. Reticuloendothel. Soc. 33:263-273

3 Lin W, Huang Y-w, Zhou X-D, Ma Y (2006) In vitro toxicity of silica nanoparticles in human lung cancer cells. Toxicol. Appl. Pharmacol. 217:252-259

4 Chang J-S, Chang KLB, Hwang D-F, Kong Z-L (2007) In vitro cytotoxicity of silica nanoparticles at high concentrations strongly depends on the metabolic activity type of the cell line. Environ. Sci. Technol. 41:2064-2068

5 Barnes CA, Elsaesser A, Arkusz J, Smok A, Palus J, Lesniak A, Salvati A, Hanrahan JP, de Jong WH, Dziubaltowska E, Stepnik M, Rydzynski K, McKerr G, Lynch I, Dawson KA, Howard CV (2008) Reproducible Comet Assay of Amorphous Silica Nanoparticles Detects No Genotoxicity. Nano Lett. 8:3069-3074

6 Lundqvist M, Sethson I, Jonsson B-H (2004) Protein Adsorption onto Silica Nanoparticles: Conformational Changes Depend on the Particles' Curvature and the Protein Stability. Langmuir 20:10639-10647

7 Shang W, Nuffer JH, Dordick JS, Siegel RW (2007) Unfolding of Ribonuclease A on Silica Nanoparticle Surfaces. Nano Lett. 7:1991-1995

8 Karlsson M, Carlsson U (2005) Protein adsorption orientation in the light of fluorescent probes: Mapping of the interaction between site-directly labeled human carbonic anhydrase II and silica nanoparticles. Biophys. J. 88:3536-3544

9 Lynch I, Dawson KA (2008) Protein-nanoparticle interactions. Nano Today 3:40-47

10 Dutta D, Sundaram SK, Teeguarden JG, Riley BJ, Fifield LS, Jacobs JM, Addleman SR, Kaysen GA, Moudgil BM, Weber TJ (2007) Adsorbed Proteins Influence the Biological Activity and Molecular Targeting of Nanomaterials. Toxicol. Sci. 100:303-315

11 Angelos S, Liong M, Choi E, Zink JI (2008) Mesoporous silicate materials as substrates for molecular machines and drug delivery. Chem. Eng. J. (Amsterdam, Neth.) 137:4-13

12 Trewyn BG, Nieweg JA, Zhao Y, Lin VSY (2008) Biocompatible mesoporous silica nanoparticles with different morphologies for animal cell membrane penetration. Chem. Eng. J. (Amsterdam, Neth.) 137:23-29

13 Chung T-H, Wu S-H, Yao M, Lu C-W, Lin Y-S, Hung Y, Mou C-Y, Chen Y-C, Huang D-M (2007) The effect of surface charge on the uptake and biological function of mesoporous silica nanoparticles in 3T3-L1 cells and human mesenchymal stem cells. Biomaterials 28:2959-2966

14 Xing X-L, He X-X, Wang K-M, Peng J-F, Tan W-H (2006) Studies on the cellular uptake of SiNPs with different surface charges. Gaodeng Xuexiao Huaxue Xuebao 27:2076-2078

15 Sun W, Fang N, Trewyn BG, Tsunoda M, Slowing II, Lin VSY, Yeung ES (2008) Endocytosis of a single mesoporous silica nanoparticle into a human lung cancer cell observed by differential interference contrast microscopy. Anal. Bioanal. Chem. 391:2119-2125

16 Wang Y, Tang Z, Correa-Duarte MA, Pastoriza-Santos I, Giersig M, Kotov NA, Liz-Marzan LM (2004) Mechanism of Strong Luminescence Photoactivation of Citrate-Stabilized Water-Soluble Nanoparticles with CdSe Cores. J. Phys. Chem. B 108:15461-15469

17 Xing X, He X, Peng J, Wang K, Tan W (2005) Uptake of silica-coated nanoparticles by HeLa cells. J. Nanosci. Nanotechnol. 5:1688-1693

18 Lu C-W, Hung Y, Hsiao J-K, Yao M, Chung T-H, Lin Y-S, Wu S-H, Hsu S-C, Liu H-M, Mou C-Y, Yang C-S, Huang D-M, Chen Y-C (2007) Bifunctional Magnetic Silica Nanoparticles for Highly Efficient Human Stem Cell Labeling. Nano Lett. 7:149-154

19 Kim S, Pudavar HE, Bonoiu A, Prasad PN (2007) Aggregation-enhanced fluorescence in organically modified silica nanoparticles: a novel approach toward high-signal-output nanoprobes for two-photon fluorescence bioimaging. Adv. Mater. (Weinheim, Ger.) 19:3791-3795

20 He X, Liu F, Wang K, Ge J, Qin D, Gong P, Tan W (2006) Bioeffects of different functionalized silica nanoparticles on HaCaT cell line. Chin. Sci. Bull. 51:1939-1946

21 Jin Y, Kannan S, Wu M, Zhao JX (2007) Toxicity of Luminescent Silica Nanoparticles to Living Cells. Chem. Res. Toxicol. 20:1126-1133

22 Ma Y, Shortreed MR, Li H, Huang W, Yeung ES (2001) Single-molecule immunoassay and DNA diagnosis. Electrophoresis 22:421-426

23 Adams M, Lin W, Ma Y (2007) Quantitative determination of ZnO nanoparticles in human bronchoalveolar carcinoma-derived lung cancer cells. J. Undergrad. Chem. Res. 6:1.19-11.22

24 Bradford MM (1976) A rapid and sensitive method for the quantitation of microgram quantities of protein utilizing the principle of protein-dye binding. Anal. Biochem. 72:248-254

25 Hartree EF (1972) Determination of protein. Modification of the Lowry method that gives a linear photometric response. Anal. Biochem. 48:422-427

26 Correa-Duarte MA, Giersig M, Liz-Marzan LM (1998) Stabilization of CdS semiconductor nanoparticles against photodegradation by a silica coating procedure. Chemical Physics Letters 286:497-501

27 Ung T, Liz-Marzan LM, Mulvaney P (1999) Redox Catalysis Using Ag@SiO2 Colloids. Journal of Physical Chemistry B 103:6770-6773

28 Liz-Marzan LM, Giersig M, Mulvaney P (1996) Synthesis of Nanosized Gold-Silica Core-Shell Particles. Langmuir 12:4329-4335

29 Iler RK; (E. I. du Pont de Nemours & Co.): US, 1959

30 Graf M, Garcia RG, Waetzig H (2005) Protein adsorption in fused-silica and polyacrylamide-coated capillaries. Electrophoresis 26:2409-2417

31 Ekuma CE, Ugwu EI, Idenyi NE (2006) Adsorption density and spectra distribution of adsorbed lysozyme as a function of pH and temperature. J. Appl. Sci. 6:1982-1985

32 Gemeinhart RA, Luo D, Saltzman WM (2005) Cellular Fate of a Modular DNA Delivery System Mediated by Silica Nanoparticles. Biotechnol. Prog. 21:532-537

33 Chen M, von Mikecz A (2005) Formation of nucleoplasmic protein aggregates impairs nuclear function in response to SiO2 nanoparticles. Exp. Cell Res. 305:51-62

34 Malamud D, Drysdale JW (1978) Isoelectric points of proteins: a table. Anal. Biochem. 86:620-647

35 Lin S-H, Hung C-L, Juang R-S (2008) Applicability of the exponential time dependence of flux decline during dead-end ultrafiltration of binary protein solutions. Chem. Eng. J. (Amsterdam, Neth.) 145:211-217

36 Park CS, Lee PH (1994) Vesicular transport with emphasis on exocytosis. Yonsei Med. J. 35:355-377

37 Erickson B (2008) Evaluating Nanomaterials. C&EN 86:5

CONCLUSIONS

The sample presentation geometries presented were each successful in single cell or single particle imaging. The square microcapillary, with known internal dimensions, was useful for the quantification of fluorescent nanoparticles (NPs). The combination small right angle prism-microscope slide optic proved to be the most useful for live single cell imaging, with externally-delivered laser excitation.

Exposure to nanoparticles of 13 and 22 nm Al_2O_3 and 20 nm CeO_2 induced membrane depolarization in living human lung cancer-derived (A549) cells. After one hour, the greatest depolarization was observed in 13 nm Al_2O_3-dosed cells, followed by those dosed with 22 nm Al_2O_3 and 20 nm CeO_2. This illustrated a size-dependent effect in Al_2O_3 nanoparticles. It suggested that, although CeO_2 is more toxic than Al_2O_3, there may be different mechanisms through which they induce cytotoxicity. As no protein supplement was present in the cell imaging buffer, it suggested there may be nanoparticle adsorption onto cell surface membrane proteins, which could contribute to membrane depolarization.

Amorphous silica nanoparticles with fluorescent semiconductor cores were employed in the characterization of silica NP internalization in living A549 cells under different conditions. In general, after cells had been exposed to NPs for approximately ten hours, the rate of particle internalization decreased rapidly and the number of particles inside cells nearly ceased to increase. It was found that, when the nanoparticles were coated with adsorbed proteins, the charge of the adsorbed proteins affected the rate of cellular uptake. The adsorbed proteins with a less negative charge allowed NPs to enter

cells at a slightly faster rate. The most significant increase in silica NP internalization was observed in the absence of adsorbed proteins on the particle surface. Observations of these samples compared to all protein-coated samples suggested that cells exposed to bare silica NPs experienced indiscriminate adsorption of particles onto surface membrane proteins. Through the ongoing process of endocytosis, the adsorbed NPs were internalized at a rate of approximately three times that of protein-coated NPs.

Nanoparticles allowed to pre-agglomerate in complete culture medium were internalized only slightly slower than freshly dispersed NPs. Since particle agglomeration was not responsible for the decreased rate of uptake at ten hours, particle loss from live cells was investigated. It was shown that, after environmental NPs were removed, the particles that were previously internalized were, in part, expelled to the extracellular environment. Particle loss was most rapid immediately following the environmental cleanup, but slowed rapidly. Within 24 hours, cells were observed to have lost a little less than half of their internalized NPs.

The results shed some light on the role of surface-adsorbed proteins in NP-biological systems interactions. They show that the safety of NP exposure should be evaluated not only for uptake in biological organisms, but also for the organism’s ability to eliminate the particles. In addition, nanoparticle release into the environment should be carefully evaluated since NPs equilibrated by protein adsorption and agglomeration were actively internalized by the cells.

VITA

Isaac Alexander Stayton was born on November 15, 1978, in the state of Missouri. He graduated with a Bachelor of Science in Chemistry from Truman State University in Kirksville, Missouri in 2002. He then attended Missouri University of Science and Technology (formerly the University of Missouri – Rolla). There he received his PhD in Analytical Chemistry in May 2009.